Small-Molecule Organic Photovoltaic Devices: Applications and Reliability

by

Xiaoran Tong

A dissertation submitted in partial fulfillment
of the requirements for the degree of
Doctor of Philosophy
(Materials Science and Engineering)
in The University of Michigan
2014

Doctoral Committee:

Professor Stephen R. Forrest, Chair
Professor L. Jay Guo
Professor Jamie D. Phillips
Associate Professor Max Shtein

ACKNOWLEDGEMENTS

This thesis would not have been possible without the support and contribution of others. My deepest gratitude is due to my advisor Stephen Forrest for giving me support, patience and constructive feedback, and shaping my view of research through high standards for curiosity, thinking, writing and communication.

Michael Slootsky has contributed the most to the OPV reliability work - designing the setup and discussing the degradation theory. Mike has given me the most support through the course of the PhD program, constantly pushing my thinking and encouraging me to never give up.

Nana Wang and Quinn Burlingame are valuable collaborators in the reliablity work contributing helpful discussions and experimental work. I thank Nana for her skills to fabricate large-area OPV devices with amazing yield, and Quinn for FTIR measurements in Chapter VII.

I am thankful for my my committee members, Max Shtein, Jamie Phillips and Jay Guo, for taking the time to read this thesis and provide helpful feedback.

I am indebted to my first mentors in the basics of organic semiconductors and devices - Chris Giebink, Stephane Kéna-Cohen, Richard Lunt, Mike Arnold, Rhonda Bailey-Salzman, Xin Xu, Yiru Sun and Jeramy Zimmerman. I am indebted to Kyle Renshaw, Yifan Zhang, Robert Krasny, Mark Thompson, Peter Djurovich for the helpful discussions on degradation theory. I thank OCM members for giving me support and creating an enjoyable environment in the group: Ning Li, Kuen-Ting Shiu, Guodan Wei, Xiangfei Qi, Greg McGraw, Brian Lassiter, Xuhuai Zhang, Kyusang Lee, Kevin Bergemann, Xin Xiao, ByeongSeop Song, Jaesang Lee, Xiao Liu, Anurag

Panda, Xiaozhou Che, Dejiu Fan, and Olga Griffith. Special thanks to Eva Ruff for administrative and emotional support. I am grateful to friends in Michigan and elsewhere for making graduate school a fun journey. Lide Zhang, Seow Yuen Yee, Nanjun Liu, John Schaibley and Val Schaibley, Jeffery Gregory and Jishu Xu are great friends and great dinner party companions. Finally, I am thankful to my mom for being the role model in my life, and for the constant support and love.

Xiaoran Tong

Ann Arbor, MI

July, 2014

TABLE OF CONTENTS

LIST OF FIGURES

Figure

LIST OF TABLES

Table

LIST OF APPENDICES

Appendix

ABSTRACT

Small-Molecule Organic Photovoltaic Devices: Applications and Reliability

by

Xiaoran Tong

Chair: Stephen R. Forrest

The development of organic optoelectronic devices has moved forward at an incredible pace over the past three decades. Prototype organic solar cell panels have emerged in the personal electronic market, and displays using organic light-emitting diodes have become an essential part of consumer electronics. This thesis focuses on the application and reliability of organic photovoltaic cells (OPVs), as they are promising candidates as low-cost, flexible solar energy conversion sources.

Top-illuminated organic photovoltaic cells present opportunity to widen OPV applications, with potential use as power generating coatings on flexible and low-cost substrates. In the first part of the thesis, we explore inverted small-molecule organic photovoltaic cells on reflective metal substrates. We investigate the design of inverted OPVs. We demonstrate methods to overcome challenges in device performance and achieve inverted OPV on metal substrates with comparable efficiency to conventional devices.

In the second part of the thesis, we study the reliability of small-molecule OPVs. We start with an extensive overview of characterization and reporting of OPV oper-

ational lifetime, device packaging and current research progress. We present a fully-automated, compact experimental setup for long-term reliability testing. We identify exciton-induced product as a dominant degradation mechanism in organic solar cells, and describe the physical theory that accurately predicts the burn-in period of device degradation. Device reliability can be greatly improved by reducing exciton lifetime, such as employing a mixed donor-acceptor active layer. The degradation mechanism also applies to photodegradation of neat OPV materials, and the stability is substantially improved in the mixed donor-acceptor film. In long-term lifetime study, we show that oxygen diffusion into the active layer is the primary cause of degradation, leading to increased recombination current.

CHAPTER I

Introduction to organic semiconductors and devices

We begin with a review of organic semiconductors and optoelectronic devices. We discuss the unique capabilities, fundamental physics, processing techniques and applications of organic semiconductors and devices. This chapter is not intended to be exhaustive but rather introductory to major advances in the field of organic optoelectronic devices.

1.1 Organic semiconductors

Organic semiconductors are a group of conjugated carbon-based materials with key differences from their inorganic counterparts such as Si, Ge, or III-V compounds. Organic materials are weakly bonded by van der Waals force, resulting in low evaporation temperatures (<500 ℃) and mechanical versatility, while inorganic semiconductors are covalent bonded crystals that are often brittle.[1] The optical and electronic properties of organics can be tailored via synthesis, thus providing unlimited possibilities in terms of material properties and combination. Moreover, organics have the potential as low-cost and flexible electronic devices that are compatible with cost-effective fabrication techniques such as roll-to-roll processing.[2, 3]

The optoelectronic properties of organic materials arise from the π-conjugated system. In carbon atoms, the 2s and 2p orbitals form sp^2 hybridization, where the three sp^2 orbitals exhibit a planar trigonal structure and the p_z orbital is perpendicular to the sp^2 plane. A σ-bond is formed by the orbital overlap of two sp^2 orbitals from two carbon atoms. The resulting occupied bonding orbitals (σ) and unoccupied

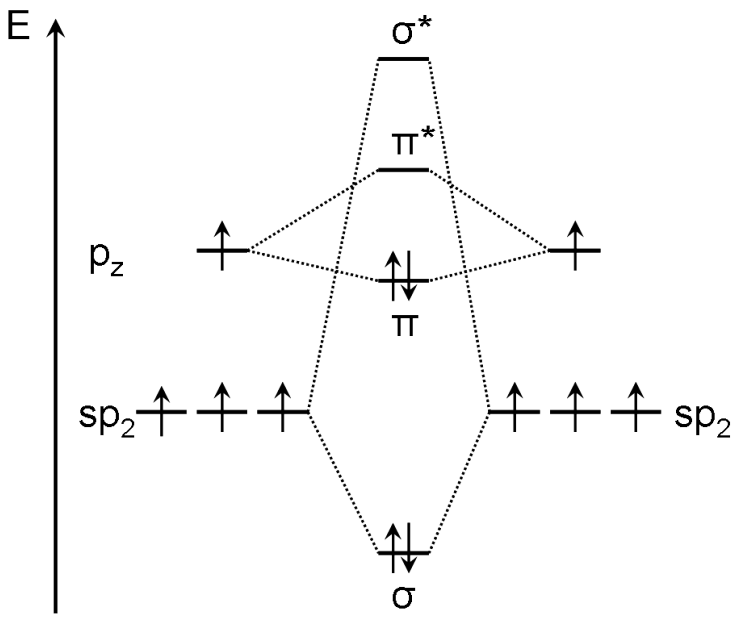

Figure 1.1: Orbitals and bonds for two sp^2-hybridized carbon atoms.

anti-bonding orbitals (σ^*) have a large energy difference beyond the visible spectral range. On the other hand, the neighboring p_z orbitals overlap and form the so-called π-bond, creating a delocalized electron density. The energy difference between the bonding and anti-bonding π-orbitals is much smaller thus contributing to semiconducting properties. The electronic properties of the material are determined by the π-electrons in the highest occupied molecular orbital (HOMO), as they are the most-easily excited into the lowest unfilled π^*-orbitals, known as lowest unoccupied molecular orbital (LUMO).[1] A schematic of the orbitals and bonds is shown in Figure 1.1.

The field of conjugated organic materials is largely divided into two categories - small-molecules and polymers. Polymers are large molecules with repeating units known as monomers. Conjugated polymers have π-systems that extend along the carbon backbone chain forming one-dimensional electronic systems, resulting in considerable bandwidth (on the scale of eV). Polymer-based devices are fabricated via solution processing.[4] The photoexcited states are generally singlet excitons, which

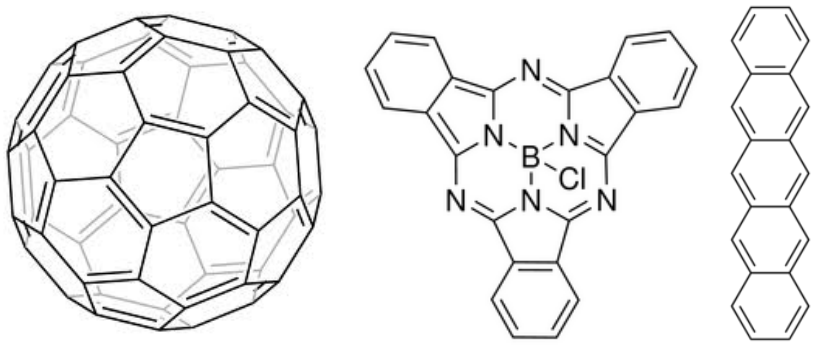

(a) (b) (c)

Figure 1.2: Examples of small-molecule organic semiconductors. (a) C_{60} is the most widely used acceptor material in organic photovoltaic cells. (b) SubPc is an archetypal donor material in OPVs. (c) Pentacene is a common p-type channel material in organic thin-film transistors.

can generate polaron pairs via interchain or intrachain interactions.[5, 6]

On the other hand, the term small-molecule refers to small molecular weight (<1000 g/mol) organic semiconductors. Figure 1.2 shows the molecular structure of three small-molecule materials. Fullerene C_{60} and boron sub-phthalocyanine chloride (SubPc) are widely used acceptor and donor materials in organic photovoltaic cells (OPVs) (Fig. 1.2(a) and (b)). Pentacene (Fig. 1.2(c)) is used as the p-type channel material in organic thin-film transistors (OTFTs), with carrier mobility exceeding 1 $cm^2/V{\cdot}s$.[7]

Amorphous thin films of small-molecules are the most commonly seen in literature, as they are easily fabricated and do not require post-processing. It has been shown, however, that devices benefit from crystallization, as carrier and exciton transport are enhanced via crystalline domains.[8, 9, 10] Single crystals of small-molecules can also be produced, providing an extraordinary system to study the electronic structure and properties of organic materials.[11, 12] Despite the difference in molecular structure between polymers and small-molecules, the photoexcitation and carrier transport processes in these materials are similar in nature, thus theoretical approaches often apply

to both categories. Since conjugated small-molecules are the foundation of this thesis, all following introduction to the physics and applications of organic semiconductors will focus on small-molecules.

1.2 Electronic processes in organics

1.2.1 Excitons

1.2.1.1 Excited states in organic molecules

Upon absorption of a photon, the electron in the HOMO is excited into the LUMO. The lowest energy required for such a transition to occur is the HOMO-LUMO gap minus the exciton binding energy, also called the optical gap, which is typically between 1-4 eV for the organic materials concerned in this thesis. The excitation results in 25% of singlet (spin = 0) and 75% of triplet (spin = 1) states. According to conservation of angular momentum, transitions between singlet and triplet states are forbidden. However, intersystem crossing exists when strong spin-orbit coupling is present. For example, transition metal complexes such as fac tris(2-phenylpyridine) iridium ($Ir(ppy)_3$) can achieve efficient intersystem crossing, thus are used as high-efficiency phosphorescent materials in organic light-emitting diodes (OLEDs).[13] Figure 1.3 shows the radiative and non-radiative processes and corresponding rates in a typical organic molecule. Once an electron is excited from the ground state (S_0) to the singlet state S_1, it can decay radiatively (fluorescence) or nonradiatively from the singlet state, or go through intersystem crossing to the triplet state (T_1), then decay radiatively (phosphorescence) or nonradiatively. The rate of internal conversion is several orders of magnitude higher than other decay processes, thus relaxation from the excited state is generally assumed to be from the lowest vibronic state.

All the processes compete with one another. The overall lifetime of a given singlet

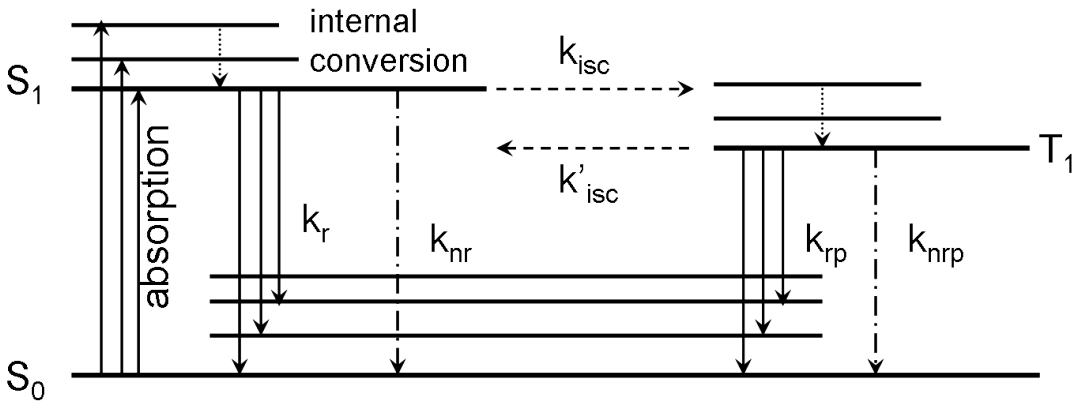

Figure 1.3: Radiative and nonradiative processes in organic materials. The subscripts r and nr represent the radiative and nonradiative decay in the singlet manifold, and rp and nrp represent processes in the triplet manifold. The subscript isc stands for intersystem crossing.[1]

state is determined by the rates of all processes, viz:

$$\tau_0 = (k_r + k_{nr} + k_{isc})^{-1} \tag{1.1}$$

Here k_r, k_{nr} and k_{isc} are rates corresponding to radiative, nonradiative decay, and intersystem crossing. The natural lifetime of excited states in organic molecules are on the order of nanoseconds for singlets and microseconds for triplets.[14, 15]

The above describes photoexcitation in isolated molecules. When molecular aggregates are formed, the excitation can migrate among molecules. The movement of excited states in aggregates is described by quasi-particles known as excitons. First proposed by Frenkel then generalized by Wannier, the concept of exciton describes the particle-like traveling of the excitation energy between molecules.[16, 17] Excitons are viewed as bound electron-hole pairs with zero electric charge. Excitons in organic aggregates largely resemble excited states in isolated molecules, since the intermolecular interaction is weak.[1] Excitons are generated primarily by direct optical excitation in the case of organic photovoltaic cells and photodetectors, and by carrier recombination in the case of organic light-emitting diodes. They are central to all

energy generation and transfer processes in organic materials.

1.2.1.2 Types of excitons

Excitons are categorized according to their spatial extent. The predominant type in organic materials is the Frenkel exciton, where the electron-hole pair resides on the same molecule and migrates among molecules as a unit.[16] The radius of the Frenkel exciton is on the order of the size of a single molecule, generally below 5 Å. Such a tightly bound electron-hole pair is a result of the weak Coulombic screening, as the relative dielectric constant (ϵ_r) in organic materials is small ($\sim$3). On the contrary, the large ϵ_r of inorganic semiconductors (ϵ_r(Si)=11.7, ϵ_r(GaAs)=12.9) results in strong Coulombic screening, thus the excited states are loosely bound Wannier-Mott excitons with the electron-hole separation on the order of 40-100 Å.[17] The general expression of exciton binding energy is shown in Equation 1.2.

$$E_B = \frac{e^2}{4\pi\epsilon_0\epsilon_r r} \tag{1.2}$$

Here E_B is the binding energy, e is the elementary charge, ϵ_0 is the vacuum permittivity, ϵ_r is the relative dielectric constant and r is the electron-hole separation. The binding energies of Wannier-Mott excitons are small, thus the excitons in bulk inorganic semiconductors are easily dissociated into free charge carriers at room temperature. Excitonic behavior in inorganic materials is observed at low temperature or under quantum confinement. The third category of exciton is the charge transfer (CT) exciton, which is a neutral excited state that extends to one or two nearest-neighbor intermolecular distances.[1] The CT excitons are particularly important in fullerene (C_{60} and C_{70}) thin films, with significant contributions to absorption and photocarrier generation.[18]

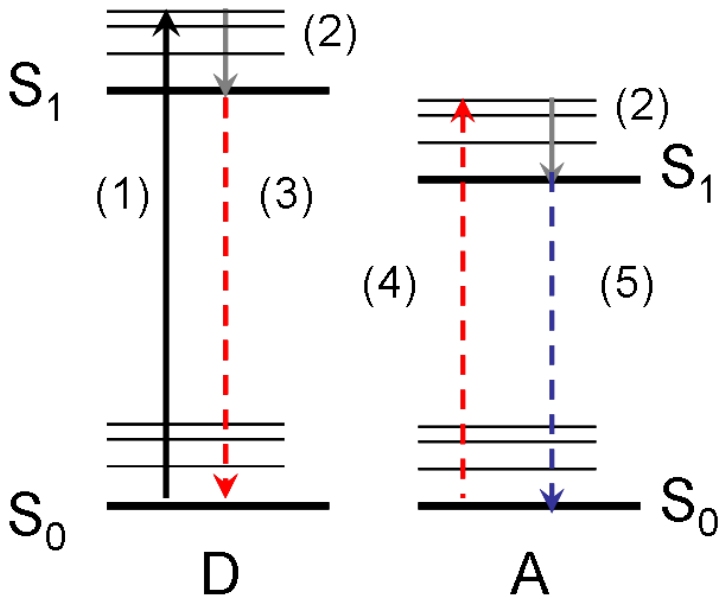

Figure 1.4: A schematic of Förster energy transfer. The labeled processes are: (1) Donor excitation; (2) Internal conversion in donor and acceptor; (3) Nonradiative decay in donor; (4) Acceptor excitation; and (5) Acceptor emission. Processes (3) and (4) are the resonance energy transfer.

1.2.1.3 Exciton energy transfer

The movement of excitons in organic materials is governed by energy transfer processes. In organic devices, nonradiative energy transfer processes dominate. Förster resonance energy transfer is an energy transfer process through nonradiative dipole-dipole interaction.[19] In a Föster transfer, the nonradiative decay of the donor excited state and excitation of the acceptor are resonant processes due to the overlap in the emission and absorption spectra. Here the terms donor and acceptor denote the giver and receiver of excitation energy. They can be the same or different molecular species. In the acceptor, the excited state can either quickly go through vibronic relaxation and reach the lowest vibronic state, making the transfer process irreversible; or transfer the energy to another molecule, enabling diffusion process. Figure 1.4 shows a schematic of the energy transfer process.

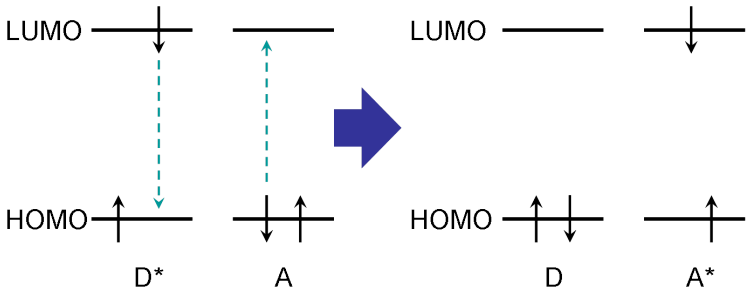

(a)

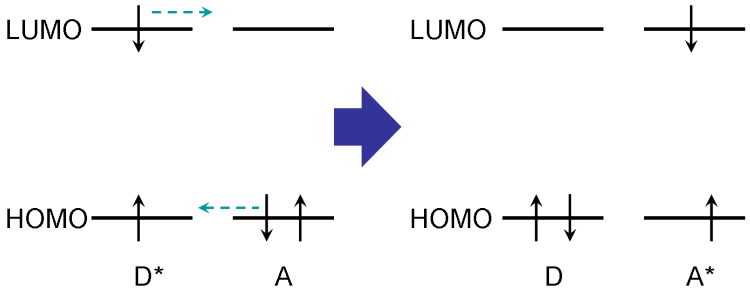

(b)

Figure 1.5: Comparison between (a) Förster and (b) Dexter energy transfer

The Förster transfer rate is given by:

$$K_{D\to A}^{F} = \frac{1}{\tau_D}\left(\frac{R_0}{R}\right)^6, R_0^6 = \frac{3c^4\Phi_{em}}{4\pi\omega^4 n_0^4 \tau_D R^6}\int F_D(\omega)\sigma_A(\omega)d\omega \tag{1.3}$$

where R is the distance between donor and acceptor molecules, $F_D(\omega)$ is the normalized fluorescence emission spectrum, $\sigma_A(\omega)$ is the normalized acceptor absorption cross section, τ_D is the natural exciton lifetime of the donor, n_0 is the refractive index and Φ_{em} is the emission quantum yield.[19, 1] At the Förster radius $R = R_0$, the Förster transfer rate equals the natural lifetime, and the transfer efficiency is 50%. The Förster radius depends on the spectral overlap between the donor emission and acceptor absorption.

In 1953, Dexter proposed a nonradiative energy transfer process where donor and acceptor molecules exchange electrons.[20] Figure 1.5 shows the difference between Förster and Dexter transfer processes.

Dexter energy transfer is allowed when spin is conserved in both molecules, thus both singlet-singlet and triplet-triplet Dexter transfer is possible. The transfer rate is given by:

$$K_{D\to A}^{D} = 2\pi \left|\beta_{DA}\right|^2 \int F_D(\omega)\sigma_A(\omega)d\omega \tag{1.4}$$

Here β_{DA} is the exchange energy interaction between the donor and acceptor molecules. The transfer rate again depends on the spectral overlap of donor emission and acceptor absorption. Dexter energy transfer is a much shorter range interaction, which only occurs when the donor and acceptor molecules are nearest neighbors. The Förster radius, however, can be on the order of a few nanometers.[14]

Radiative energy transfer is also possible. In a radiative energy transfer process (photon re-absorption), the fluorescence emitted from the donor material is reabsorbed by the acceptor material. Photon reabsorption is an important incoherent transfer process at longer distance (>10 nm). It requires the donor and acceptor materials to have large oscillator strengths and significant overlap between emission and absorption spectra. It also leads to an increase in observed singlet lifetime.

1.2.1.4 Exciton diffusion

The ability of excitons to migrate in the material is described by the exciton diffusion length, $L_D = \sqrt{D\tau_0}$, where D is exciton diffusivity and τ_0 is exciton natural lifetime. The diffusion length is on the order of 10 nm for amorphous films.[9, 14] Diffusion lengths on the order of microns have been reported for highly ordered structures such as anthracene crystals.[21, 22] The exciton diffusivity depends on the scattering time of excitons by optical and acoustic phonons, and the scattering and capture of excitons by impurities and defects.[23, 24] It was proposed that the scattering of excitons by impurities is negligible compared to the scattering by phonons even at relatively high impurity levels.[23]

The exciton motion in an isotropic medium is described by the exciton diffusion

equation:

$$\frac{\partial N_X(\boldsymbol{r},\lambda)}{\partial t} = D\frac{\partial^2 N_X(\boldsymbol{r},\lambda)}{\partial x^2} - k_0 N_X(\boldsymbol{r},\lambda) + G(\boldsymbol{r},\lambda) \tag{1.5}$$

Here, $N_X(\boldsymbol{r},\lambda)$ is the exciton density generated by absorption of photons of wavelength, λ, and at position, $\boldsymbol{r}$. Also, D is the exciton diffusivity, k_0 is the exciton natural decay rate in the film indicating the probability of exciton decay per unit time, and $G(\boldsymbol{r},\lambda)$ is the photogeneration rate of excitons in the device active layers determined by the local intensity of the optical electric field.[24] Usually, one-dimensional diffusion is assumed in organic devices to simplify the problem. Predicting exciton motion is particularly important to model performance of planar heterojunction OPVs, as only the exciton population that diffuses to the dissociating interface contributes to photocurrent.[15] Appendix B.2 provides details on simulation of exciton diffusion in organic devices.

1.2.1.5 Exciton quenching

Besides the unimolecular decay processes indicated in Fig. 1.3, the excited states can also interact with other free or trapped excitons, chemical impurities or crystal defects. The impurities create mid-energy states that can quench excitons. One method to analyze the trap-induced quenching is the approach-collision model, where the exciton diffuses to the trap center and is captured.[24, 25] The trap-induced quenching rate is given by:

$$k_{XT} = 8\pi D R_C \tag{1.6}$$

where R_C is the trap capture radius for excitons.

The trap-induced quenching shortens the exciton lifetime by:

$$\frac{1}{k} = \frac{1}{k_0 + k_{XT}} \tag{1.7}$$

where $1/k$ is the observed exciton lifetime. In Chapter VI we analyze the formation

of trap states, and their impact on OPV device performance.

There are other exciton loss mechanisms such as triplet-triplet annihilation and singlet-triplet annihilation.[1, 26] In such processes two excitons transfer energy and create a highly excited state and a ground state, leading to a loss of one exciton. They play a larger role in OLEDs as the exciton density is much higher than that of OPV and organic photodetector (OPD) devices.

1.2.2 Charge carriers

1.2.2.1 Carrier generation

Charge carriers are essential to optoelectronic device operation. The intrinsic carrier density is determined by the number of carriers thermally excited from the HOMO to the LUMO of organic semiconductors (equivalent to valence band to conduction band excitation in inorganic semiconductors). Due to the large bandgap in organic materials ($\sim$ 2 eV), the intrinsic carrier density is extremely low ($\sim$ 10^5 cm^{-3}) compared to inorganic semiconductors (n_i(Si) = 10^{10} cm^{-3}). These materials only exhibit semiconducting properties when carriers are extrinsically generated by methods such as injection from electrodes, dissociation of optically excited states and doping.

In OPVs, the carriers are generated by dissociated excitons. In a heterojunction, the energy difference between the HOMO of the donor and LUMO of the acceptor is smaller than the binding energy (E_B) of the exciton, thus providing the driving force for dissociation. It has been proposed that the dissociation of exciton forms a nascent hot CT exciton, which then creates polaron pairs that further dissociate into carriers.[27] Jailaubekov et al., probed the hot CT exciton formation and relaxation, and proposed that charge separation at the donor/acceptor (D/A) interface occurs on a picosecond timescale.[28] A diagram of the dissociation processes occurring at a heterojunction interface is shown in Fig. 1.6.

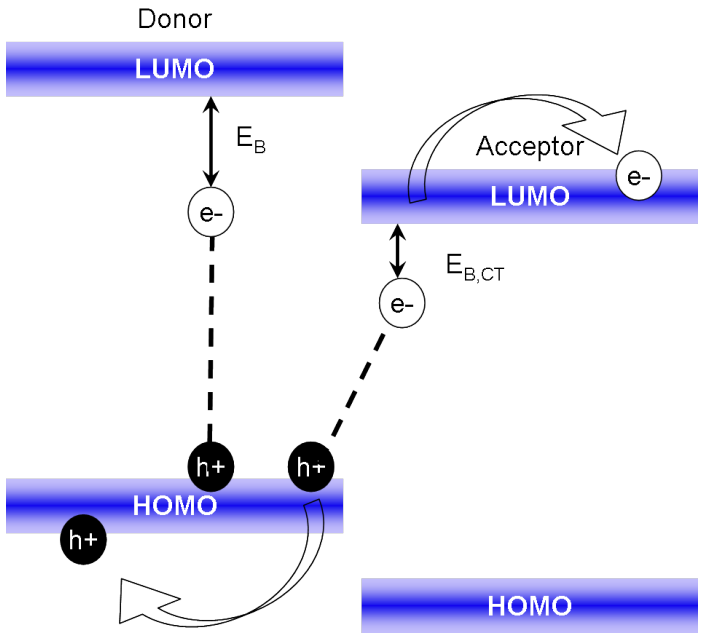

Figure 1.6: Exciton dissociation process. Excitons that reach the D/A interface dissociate to CT excitons, due to the difference in binding energy. The CT excitons form polaron pairs that further dissociate into charge carriers.

1.2.2.2 Carrier transport

Carrier transport in a bulk material is determined by the interaction energy between neighboring molecules and the polarization energy of the molecule. When the interaction energy is large, the carriers move in a transport band as a delocalized plane wave. On the contrary, when the polarization energy is large, the carriers are localized and transferred via hopping.[1] In band transport, the mobility of carriers has a temperature dependence of $\mu \propto T^{-n}$, n >1; while in the hopping case mobility follows $\mu \propto \exp(-E_A/kT)$, where E_A is the activation energy. In organic materials, the charged molecule easily polarizes its neighboring molecules and creates geometric distortions in its local environment. The charge carrier changes the spatial distribution of electrons in the σ-orbitals and thus bond lengths. The energy associated with the change is the geometric reorganization energy. The often-used terms "carrier", "electron", and "hole" actually refer to the charge carrier and its accompanying polarization field - a polaron - in the context of organic semiconductors. The polarons

hop from molecular site to site, with a thermally-activated mobility $\ll 1$ cm^2/V·s.

The carrier density and mobility are improved by doping of the material. For example, it has been shown that oxygen doping in phthalocyanines significantly increases the carrier density and dark conductivity.[29, 30, 31] Intentional n-type and p-type doping are used in organic semiconductors to improve carrier transport. Alkali metals or Lewis acids have been used as effective dopants, however, they are likely to diffuse into the active layers and introduce instability in their properties.[32, 33] More recently, conjugated small-molecules are used as dopants. Lüssem et al provided a comprehensive review of doping in organic materials and how it affects the Fermi level, and the density and mobility of the carriers.[34] Moreover, ultralow level of doping fills and passivates intrinsic trap states, leading to a 3 orders of magnitude increase in the electron mobility in C_{60}.[35]

1.3 Processing techniques

1.3.1 Organic materials deposition

Thermal evaporation in vacuum is the most commonly used fabrication technique for smallmolecule organic thin films. Generally, the source material is placed in a resistive heating element inside a high vacuum chamber with base pressure of 10^{-6} - 10^{-8} torr. The materials are evaporated by Joule heating as current flows through the evaporation boats. The evaporated molecules nucleate on the cold substrate and form a thin film. Baffled box boats are typically used as they reduce the power loss from radiative heating, and provide more directional deposition. The evaporation rate of organic materials is usually kept below 3 Å/s, to prevent decomposition of materials.

One of the biggest advantages of thermal evaporation is the precise control of film thickness and doping ratio. The thickness of the deposited thin film is measured by a

quartz crystal monitor in the chamber and can be calibrated ex-situ by ellipsometry. Monolayer thickness control can be achieved. Moreover, the evaporation systems usually have the capability to evaporate two or more sources simultaneously while monitoring the rate of each material, enabling doping of organic thin films. The high accuracy in doping ratio is essential in organic devices. For example, the quantum efficiency of phosphorescent OLEDs has been found to depend strongly on the doping concentration of the emissive layer.[13] In OPVs, a graded bulk heterojunction active layer has been employed, where the ratio between donor and acceptor materials is varied continuously throughout the active layer, providing better charge transport and device efficiency.[36] Molar doping ratios on the order of 10^{-4} have been used to study the tail states in organic semiconductors.[35] High precision control makes thermal evaporation the primary processing method for small-molecule organic devices.

There are many other techniques to deposit organic thin films. Solution processing is a procedure where a drop of the material in solution is applied to the substrate. A spinner then rotates at high speed (∼2000 - 6000 rpm) and spreads the material to a uniform coating on the substrate. Solution processing is widely used in polymer devices and occasionally employed in small-molecule device fabrication, especially when the material is not thermally stable.[10, 37, 38, 39] The thickness of the spin-cast film is given by $d(t) = d_0 \left(1 + \frac{4\rho\omega^2}{3\mu_v} d_0^2 t\right)^{-1/2}$, ignoring evaporation, where d is the thickness of the film as a function of spin time, t, initial thickness, d_0, angular velocity, ω, and the density (ρ) and viscosity (μ_v) of the solution.[40] Sub-nanometer control of the film thickness is difficult. The desired thickness is achieved by calibration of conditions for a given material, solvent and equipment combination. Organic vapor phase deposition (OVPD) is another promising method.[41] This low vacuum (0.1 - 10 Torr) technique uses a flow of inert gas to carry the evaporated molecules to the substrate. Precise control and monitoring of thin film growth can be achieved by methods such as laser-induced fluorescence.[42] It is suitable for large-area, uni-

form deposition of organic materials.[43] By incorporating OVPD into a jet-printing configuration (organic vapor jet printing), micron scale patterning of organics can be realized.[44, 45]

1.3.2 Electrode preparation

The organic optoelectronic devices are sandwiched between two electrodes, usually a reflective metal contact and a transparent conducting contact. Low work function metals such as Al, Ag, Ag:Mg are often used as the reflective cathode materials.[46, 47, 48] Similar to deposition of organic materials, the metal contact is thermally evaporated. Since the evaporation temperature of the metal is much higher than that of the organic materials, the metal atoms arrive at high kinetic energy, resulting in damage states when metal is deposited onto organic layers.[49, 50] The defect states are known to assist carrier extraction in OPVs.[49] The damage depth is on the order of a few nanometers and can be prevented by intensive cooling of the substrate during deposition.[50, 51] Sufficient cooling of the substrates reduces lateral and vertical diffusion of the metal atoms, thus decreases the probablility of defect states generation.

The most widely used transparent conducting anode is indium-tin oxide (ITO). Alternatives to ITO have been explored, such as ultrathin metal layer, metal grid + poly(3,4-ethylenedioxythiophene) poly(styrenesulfonate) (PEDOT:PSS), metal nanowires, and carbon nanotubes.[52, 53, 54, 55, 56, 57] These contacts are more compatible with flexible OLED and OPV devices, compared to the brittle ITO. However, ITO still possesses the best combination of transparency (>80% in the visible range) and conductivity (10-20 Ω/sq), thus is the preferred choice for transparent contact.

Methods for ITO deposition include reactive ion plating, chemical vapor deposition and radio frequency (RF) sputtering.[58, 59, 60, 61] Here we briefly describe the most commonly used RF sputtering technique.

In sputtering, ions from an excited inert gas plasma are accelerated towards a target under an electric field. The atoms are bombarded from the target, nucleate on the substrate and form a thin film. The electric field is applied in DC or RF mode. In the DC mode, a constant negative voltage is applied to the target. If the target is not very conductive, the DC mode will lead to charge build-up on the target surface and hinder further bombardment. In such a situation, RF sputtering is employed, where the field alternates at a frequency higher than 50 kHz to prevent charge build-up. Sputtering maintains the stoichiometry of the target, thus is an effective method to deposit oxides. It has been found that the properties of ITO, such as optical constants, sheet resistance, surface morphology and work function, depend on the sputtering and post-deposition treatment conditions.[60, 61] For example, low sheet resistance is achieved with optimized sputtering power, and post-deposition thermal annealing in vacuum.[60] The work function of ITO is increased by increasing the oxygen partial pressure during sputtering, or applying post-deposition UV-Ozone treatment, thus improving carrier collection or injection at the contact.[62, 63]

1.4 Applications

1.4.1 Organic photovoltaic cells

1.4.1.1 Basic principles and characterization methods

Renewable energy sources are of interest due to concerns with global warming, pollution and energy shortage. Photovoltaic cells are promising renewable energy sources compatible with large-area electricity production. The photovoltaic effect was first introduced by Becquerel.[64] Upon photoexcitation of a semiconductor, charge carriers are generated and then extracted to the electrodes due to the built-in electric field, creating a photocurrent in the external circuit. Typical current density-voltage (J-V) characteristics of a solar cell are shown in Fig. 1.7.

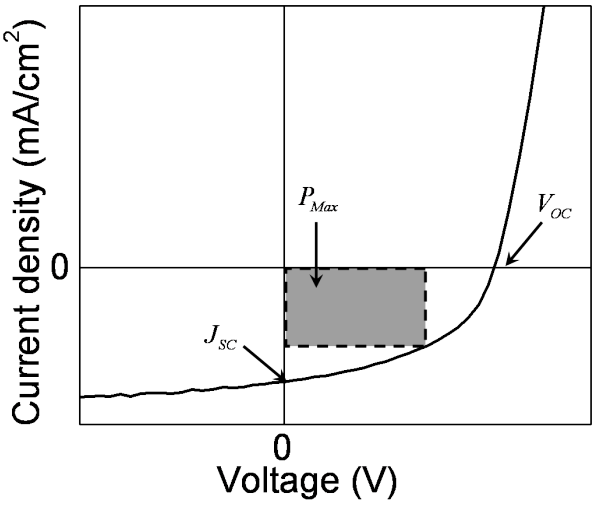

Figure 1.7: Typical current-voltage characteristics of a solar cell. The open-circuit voltage, V_{OC}, short-circuit current,J_{SC}, and the maximum power output, P_{Max}, are labeled on the curve.

The solar cell outputs power in the fourth quadrant, where $J \times V < 0$. The performance of the PV is evaluated by the power conversion efficiency (PCE), defined as the ratio of the maximum power output to the incident power (P_{Inc}).

$$PCE = \frac{\max(-J \times V)}{P_{Inc}} \tag{1.8}$$

The power conversion efficiency depends on the photocurrent at zero bias, short-circuit current (J_{SC}); the photovoltage under open-circuit, open-circuit voltage (V_{OC}); and the fill factor (FF), $FF = P_{Max}/J_{SC}V_{OC}$. The electrical sensitivity of a solar cell to incident light is quantified by external quantum efficiency (EQE):

$$EQE = \frac{\text{number of extracted charge carriers}}{\text{number of incident photons}} \tag{1.9}$$

To measure the performance of a solar cell, the device is illuminated by a simulated 1 sum, AM1.5G optical source and the J-V characteristics are recorded. To measure device EQE, a lock-in amplifier is used to measure the device current output

under chopped monochromated light. EQE is calculated by using a Si photodiode to calibrate the monochromated light intensity, .

As we have shown in Section 1.2.1, the photoexcited states in organic semiconductors are tightly bound Frenkel excitons; thus heterojunctions are required in order to generate carriers. An example of device operation of a planar OPV is shown in Figure 1.8. The incident illumination through the transparent electrode is absorbed by the active layers with efficiency, η_A. The generated excitons then diffuse to the D/A interface with efficiency η_{ED}. The number of excitons that reach the interface can be estimated by solving the continuity exciton diffusion equation (Eq. 1.5). At the interface, the excitons dissociate into charge carriers with charge transfer efficiency, η_{CT}.[15] The charge carriers are then collected by the electrodes with efficiency η_{CC}. In a planar heterojunction OPV, the electrons and holes are spatially separated, thus η_{CC} is usually approximately unity.[15] In a bulk heterojunction OPV, however, carrier recombination mechanisms such as Langevin recombination and Shockley-Read-Hall recombination are significant.[65, 66] A much more complicated model is needed to describe the charge collection efficiency.[67]

The extended quantum efficiency is then:

$$EQE = \eta_A \eta_{ED} \eta_{CT} \eta_{CC} \tag{1.10}$$

The latter three efficiencies determine the internal quantum efficiency (IQE) of the device: $EQE = \eta_A \eta_{ED} \eta_{CT} \eta_{CC} = \eta_A \times IQE$. Ideally, every absorbed photon can be converted into an extracted charge, resulting in 100% IQE, however, this is not the case due to exciton diffusion and charge recombination losses.

With a known EQE, the photocurrent (J_{ph}) under a given incident spectrum is:

$$J_{ph} = q \int EQE(\lambda) S(\lambda) \frac{\lambda}{hc} d\lambda \tag{1.11}$$

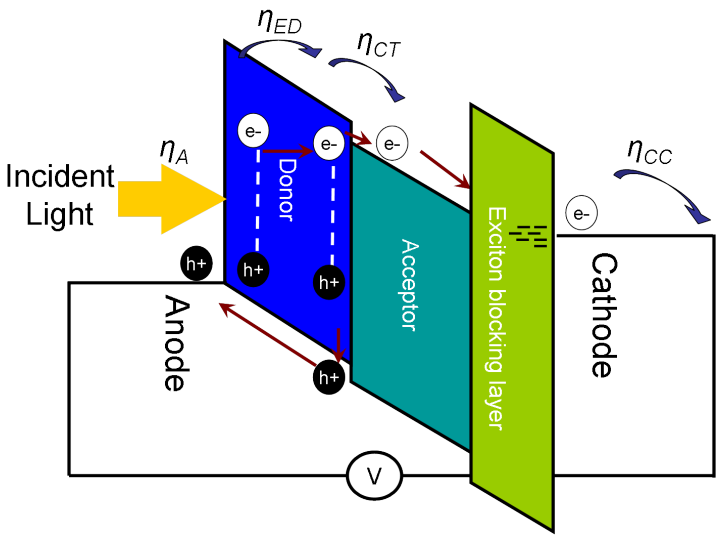

Figure 1.8: Device operation of a planar heterojunction organic photovoltaic cell. The external quantum efficiency is determined by the product of the absorption (η_A), exciton diffusion (η_{ED}), charge transfer (η_{CT}) and charge collection (η_{CC}) efficiency.[15]

Here $S(\lambda)$ is the power spectrum of the incident light, q is the elementary charge, λ is the wavelength, h is Planck's constant and c is the speed of light.

Standards have been developed to measure the solar cell performance under simulated test conditions.[68] A standard Air Mass 1.5 global (AM1.5G) spectral irradiance should be used for solar cell testing ,with an integrated 1 sun power density of 1000.4 W/m^2.[69, 70] Among all the white light sources, the Xenon-arc lamp provides an approximate spectral match to 1 sun, AM1.5G illumination, and thus is used as a solar simulator light source. Figure 1.9 shows the comparison between a 1 sun, AM1.5G illumination and a Xenon-arc lamp spectrum.

According to Eq. 1.11, any spectral mismatch between the measurement conditions and 1 sun, AM1.5G illumination condition will lead to a difference in photocurrent. The spectral mismatch factor (M) has been introduced to correct for the measurement

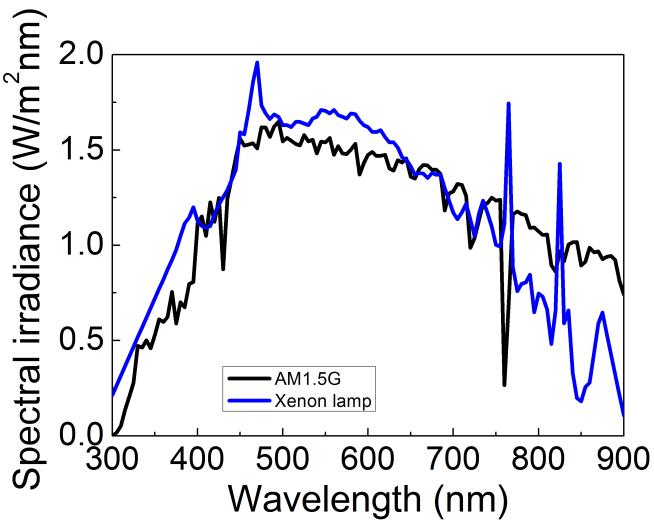

Figure 1.9: Comparison between 1 sun AM1.5G spectrum and Xenon-arc lamp spectrum.

error.[71, 72]

$$M = \frac{\int S_{SIM}(\lambda)EQE_D(\lambda)d\lambda \cdot \int S_{AM1.5G}(\lambda)EQE_R(\lambda)d\lambda}{\int S_{AM1.5G}(\lambda)EQE_D(\lambda)d\lambda \cdot \int S_{SIM}(\lambda)EQE_R(\lambda)d\lambda} \tag{1.12}$$

Here the subscripts AM1.5G and SIM represent the standard 1 sun, AM1.5G spectrum and that of the solar simulator, respectively. The subscripts R and D stand for the device and the reference cell used to measure spectra. The power spectra of the solar simulator and AM1.5G appear in both the numerator and denominator, eliminating the need for measuring absolute values of these quantities. Moreover, exact measurement of the device active area is not necessary. The spectral mismatch factor provides a convenient way to translate measurement results to device performance under standard conditions.

1.4.1.2 Diode equation for organic photovoltaic cells

The J-V characeristics of a p-n junction diode are described by the Shockley equation:[73]

$$J = J_S \left[\exp\left(\frac{V_a - JR_{SA}}{nk_BT/q} \right) - 1 \right] - J_{ph} \tag{1.13}$$

Here J_S is the reverse saturation current density, V_A is the applied voltage, R_{SA} is the series resistance, n is the ideality factor, k_B is the Boltzmann constant, and J_{ph} is the photocurrent.

Setting $J = 0$, the open-circuit voltage can be obtained:

$$V_{OC} = \frac{nk_BT}{q} \ln\left(\frac{J_{ph}}{J_S} + 1 \right) \tag{1.14}$$

The Shockley equation was derived for inorganic p-n junctions with well-defined band structure. Since the photoexcited states in organic materials are tightly bound Frenkel excitons, the physics is fundamentally different. Several studies have modeled the J-V characteristics of OPVs and arrived at similar expressions of Eq.1.13 with very different physical pictures.

Giebink et al., analyzed the J-V characteristics of a planar heterojunction OPV based on the polaron pair dynamics at the D/A interface.[74] As shown in Fig. 1.10, at the D/A heterojunction, the excitons diffuse to the interface with current density J_X and form polaron pairs. The polaron pairs then recombine or dissociate with rates k_{PPr} and k_{PPd}. The free electron (n_I) and hole (p_I) at the interface can also recombine and form polaron pairs, with a recombination rate k_{rec}.

By incorporating exponentially distributed trap states, Giebink et al., derived the

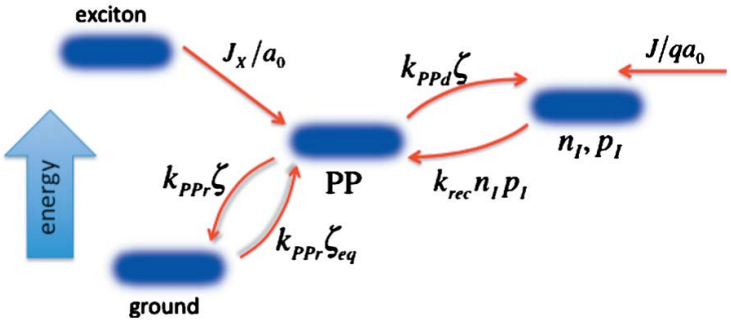

Figure 1.10: Processes at the donor/acceptor heterojunction. Adapted from Ref. [74]

ideal diode equation for organic solar cells.

$$J = J_{sD}\left[\exp\left(qV_a/n_D k_B T\right) - \frac{k_{PPd}}{k_{PPd,eq}}\right] + J_{sA}\left[\exp\left(qV_a/n_A k_B T\right) - \frac{k_{PPd}}{k_{PPd,eq}}\right] - q\eta_{PPd}J_X \tag{1.15}$$

Here J_{sD} and J_{sA} are reverse saturation current density, n_D and n_A are the ideality factors corresponding to the donor and acceptor layers, respectively. Moreover, k_{PPd} and $k_{PPd,eq}$ are the polaron pair dissociation rates and η_{PPd} is the polaron pair dissociation efficiency. The reverse saturation current density and ideality factors depend on the density of states at the HOMO and LUMO, the characteristic trap temperature, the injection barrier and voltage drop across the donor and acceptor layers, respectively. In an ideal case with symmetric injection barriers, Eq. 1.15 is reduced to an expression.

$$J = J_{sym}\left[\exp\left(qV_a/n_{sym}k_B T\right) - \frac{k_{PPd}}{k_{PPd,eq}}\right] - q\eta_{PPd}J_X \tag{1.16}$$

Studies have focused on determining the V_{OC} of the bulk heterojunction devices, in particular, the origin of recombination losses that lead to the difference between V_{OC} and the HOMO-LUMO gap of the donor and acceptor. Blakesley et al., showed that Eq. 1.14 is valid for an ideal bulk heterojunction, assuming constant electron-hole pair generation rate and detailed balance.[75] By including exponentially distributed

energetic disorder, the dependence of V_{OC} on light intensity is accurately predicted.

1.4.1.3 Types of organic photovoltaic cells

Organic photovoltaic cells are categorized according to the structure and morphology of the active layers. The term planar heterojunction OPV denotes a device structure where the active layer comprises two neat layers of donor and acceptor materials with a planar interface. Tang introduced the first efficient planar heterojunction OPV with >1% efficiency.[76] In a planar heterojunction cell, the excitons generated in the donor and acceptor materials dissociate at the D/A interface. Therefore, the PCE of a planar heterojunction OPV is limited by the exciton diffusion length in small-molecule organic semiconductors, which is usually below 40 nm.[15, 14, 4] To overcome this limit, bulk heterojunction OPVs were introduced, where the active layer utilizes a mixture of donor and acceptor, allowing excitons to dissociate immediately. The morphology of the mixed layer can be a controlled interpenetrating network of donor and acceptor layers, or a random mixture of the two materials.[77, 78, 79] It is generally agreed that a continuous charge extraction pathway is necessary to minimize charge recombination in the bulk heterojunction. Devices usually achieve higher PCE when the bulk morphology is designed to improve charge extraction, such as a "finger" interpenetrating donor/acceptor network or a graded bulk heterojunction.[77, 36]

1.4.2 Organic thin-film transistors

Transistors are indispensable components of all electronic devices. Organic thin-film transistors have inherently lower carrier mobility and switching speed compared to their inorganic equivalents. However, they possess the advantages of flexibility, low processing temperature and compatibility with a large variety of substrates. OTFTs have attracted significant research interest for potential low-cost bendable electronics.[80]

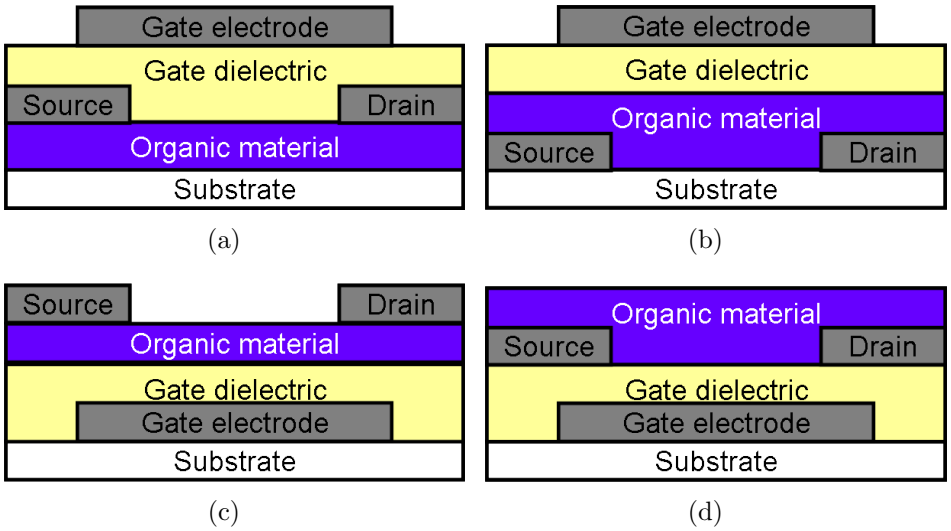

Figure 1.11: Four organic thin film transistor structures. (a) Top-contact, top-gate OTFT. (b) Bottom-contact, top-gate OTFT. (c) Top-contact, bottom-gate OTFT. (d) Bottom-contact, bottom-gate OTFT

Typically, an OTFT uses the metal-insulator-semiconductor field-effect transistor configuration. The organic semiconductor is connected to the source and drain electrodes, and separated from the gate electrode by a layer of insulating dielectric. When a gate voltage (V_{GS}) is applied, carriers are generated at the organic/dielectric interface and subsequently swept out of the channel by the applied drain-source voltage (V_{DS}). By tuning V_{GS}, the current flow across the channel can be controlled. Depending on the relative position of each material, four OTFT configurations can be fabricated, as shown in Fig. 1.11.

The performance of top-drain-source-contact OTFTs is superior to that of bottom-contact devices. The difference has been ascribed to large contact resistance, poor organic morphology, and a large potential drop at the source/organic interface due to deficiency of carriers.[81, 82, 83, 84, 80] Bottom-gate devices benefit from dielectric surface modification, resulting in improved morphology of organic layers and proper dipole alignment at the interface.[80]

The majority of OTFTs are p-type transistors, where holes are transported through

the HOMO of the channel. Small-molecule organic semiconductors such as pentacene, sexithiophene and copper phthalocyanine (CuPc) are often used as the p-channel materials.[80] It is more difficult to fabricate n-type OTFTs, as the energy barrier between the Fermi level of the contacts and LUMO of the organics is much larger. Moreover, it has been reported that electron trapping at the interface, grain boundaries and environmental impurities are more significant for electrons than holes.[85] Nonetheless, much progress have been made in n-type OTFTs, as they are key components for low-power-consumption complementary circuits.[86] The carrier mobility can be further improved when the gate dielectric surface is modified by a self-assembled monolayer, as it has been shown that growth on a low-energy surface favors carrier transport.[80, 87]

1.4.3 Other applications

Organic optoelectronic devices have many other applications that are beyond the scope of this thesis. Research in optically-pumped organic lasers, organic polariton lasers, and OLEDs has made significant progress in the past few decades.[88, 89, 12, 90, 91, 92] Among all the applications of organic optoelectronics, OLEDs is by far the most successful and commercialized technology. They have been growing rapidly in the flat panel display market. Lighting sources utilizing OLEDs are also progressing. A few selective OLED products are shown in Figure 1.12.

Compared to dominant LCDs, OLED technology has the advantage of being energy-efficient, ultra-thin, light-weight and flexible. By incorpoarting individual emissive RGB pixels, OLED displays provide high contrast ratio and vibrant colors. As of 2013, mobile devices using OLED displays have become common, and large-area OLED TVs emerging. OLED is also a promising technology for lighting sources. Currently, compact fluorescent and incandescent lamps dominate the lighting market, and light-emitting diode (LED) lamps are becoming popular. However, each tech-

(a) (b) (c)

Figure 1.12: Commercial organic light emitting diode products. (a) A Samsung Galaxy S4 phone using a 5-inch, 441 ppi active-matrix OLED display.[93] (b) An LG 55-inch OLED TV (right) compared to a conventional LCD (left).[94] (c) Philips Lumiblade OLED light source.[95]

nology has its drawbacks. Incandescent bulbs are notoriously inefficient. LED bulbs require aggressive cooling and outcoupling structures. On the other hand, OLEDs have the benefit of high energy efficiency, ultra-low operating temperature, low driving voltage, tunable color, a good color rendering index and good color temperature. It is suitable for large-area diffusive lighting sources. The flexibility and form factor of OLEDs also opens up possibilities for creative architectural design.

Organic semiconductors have attracted extensive research interests in device physics and applications. In particular, organic photovoltaic cells are promising sources for solar energy conversion. This thesis consists of two parts that focus on the application and reliability of OPVs. Part I - Inverted organic photovoltaic devices - discusses the design, fabrication, device physics and application of top-illumination small-molecule OPV cells, in search of novel and cost-effective ways to utilize OPVs. Inverted OPVs eliminate the need for a transparent substrate, and thus have the potential as cost-effective power generation coatings. Part II - Reliability of organic photovoltaic cells - investigates the long-term stability and degradation mechanisms of OPV cells. Methods that alleviate device degradation are proposed. A conclusion and future outlook is provided in the last chapter.

PART I

Inverted organic photovoltaic devices

CHAPTER II

Inverted small-molecule solar cell on reflective substrates

As OPVs gain recognition for their potential as promising solar energy conversion sources, it is important to explore ways to cost-effective utilization. Conventionally, OPVs are fabricated on transparent substrates such as glass or plastics, and employ a transparent anode consisting of ITO.[76] In this chapter, we explore the possibility of building small-molecule OPVs on reflective substrates. The inverted architecture eliminates the need for comparatively high-cost transparent substrates, allowing for use in applications such as power-generating coatings, or for growth on flexible and inexpensive opaque substrates. We demonstrate inverted small-molecule organic photovoltaic cells incorporating a reflective metal bottom contact, and a sputter-deposited transparent conducting oxide top contact.

The use of the term "inverted" is not to be confused with prior usage describing a different device architecture. In previous work, the term "inverted" has been related to bottom-illuminated solar cells grown on electron-extracting transparent ITO substrates. This requires the acceptor to be placed near the ITO contact in a planar OPV;[96, 97] or modification of the ITO by an electron selective interfacial layer, such as TiO_2,[98] or ZnO,[99] in a bulk heterojuction OPV. In this chapter, we use

inverted solar cell to describe top-illuminated cells grown on a reflective metal anode and sputter-deposited ITO as the top transparent cathode. The use of a top ITO cathode eliminates the need for transparent ITO/glass substrates or a conductive metal grid,[53] thus enabling more flexible structure design without sacrificing device active area.

2.1 Experimental procedure

The inverted structure uses a bilayer system consisting of the donor, CuPc, and the acceptor, 3,4,9,10-perylenetetracarboxylic bis-benzimidazole (PTCBI).[76] Quartz substrates were solvent cleaned,[100] then loaded into an electron beam evaporator where a 100 nm thick layer of Ni was deposited at a rate of 5 Å/s. The Ni anodes were exposed to ultraviolet (UV) ozone treatment for 30 minutes, then immediately loaded into a high-vacuum thermal deposition chamber with a base pressure of 5×10^{-7} Torr. Purified organic sources [100] were grown at a pressure of 1×10^{-6} Torr, and a rate of 1-2 Å/s. A vacuum break and exposure to air occurred before attaching a shadow mask to the deposited layers and substrate in an ultra-high-purity N_2 ambient. The top contact consisted of a 40 nm thick ITO layer sputter-deposited at 20 W (0.1 Å/s) and a pressure of 2 mTorr using Ar plasma.[61] An array of 1 mm diameter circular cathodes was defined by a shadow mask. Current-voltage (I-V) measurements were used to characterize the performance of the cells in the dark and under 1 sun, AM1.5G illumination (uncorrected for solar spectral mismatch) using a 150 W Xe arc lamp. A transfer matrix formalism was used to predict the J_{SC} under an AM1.5G solar spectrum at 1 sun (100 mW/cm^2) illumination.[15] The optical constants of organic materials and sputtered-ITO were measured using variable-angle spectroscopic ellipsometry of neat films grown on Si.

2.2 Challenges in designing inverted organic photovoltaic cells

Inverting the OPV structure introduces challenges in carrier transport and optical design. In a conventional OPV cell, a wide-bandgap buffer layer such as bathocuproine (BCP) or bathophenanthroline (BPhen) is often used prior to metal cathode deposition in order to prevent excitons from quenching at the organic/metal interface, as well as protect the photoactive layers from cathode deposition. Carrier extraction through such wide-bandgap materials is assisted via the damage states known to form upon hot metal deposition.[49] When the layer sequence is reversed, no defect state is formed, thus the carrier extraction becomes difficult. According to simulation, the photocurrent of an inverted device with the structure: quartz/Ag 100 nm/BCP 10 nm/PTCBI 30 nm/CuPc 15 nm/ITO 400 nm should be 94% of that obtained for a conventional device: glass/ITO/CuPc 15 nm/PTCBI 30 nm/BCP 10 nm/Ag 100 nm, assuming unity charge transfer efficiency and carrier collection efficiency.[15] As shown in Fig. 2.1, the lower photocurrent in inverted device is due to reduced EQE in the CuPc layer, attributed to the change in optical constants in the sputtered ITO, resulting in higher reflection at the air/ITO interface. However, this inverted structure showed high device resistance and minimal photoresponse, as seen in Fig. 2.2, possibly due to the BCP layer acting as an insulator, and damage in the CuPc layer due to ITO deposition. Similar results were observed when the BCP thickness was reduced. When the buffer layer was omitted entirely, the direct contact between the acceptor and metal cathode leads to shorts.

As shown in Sec.1.3.2, sputter-deposited ITO films require annealing (~ 400 ℃) in order to reduce sheet resistance. In the case of inverted OPVs, annealing the top ITO contact is not possible due to the low evaporation temperature of organic layers underneath. Thus the optical and electrical properties of the ITO film is inferior to that of commercial substrates. The extra absorption in sputtered-ITO can be

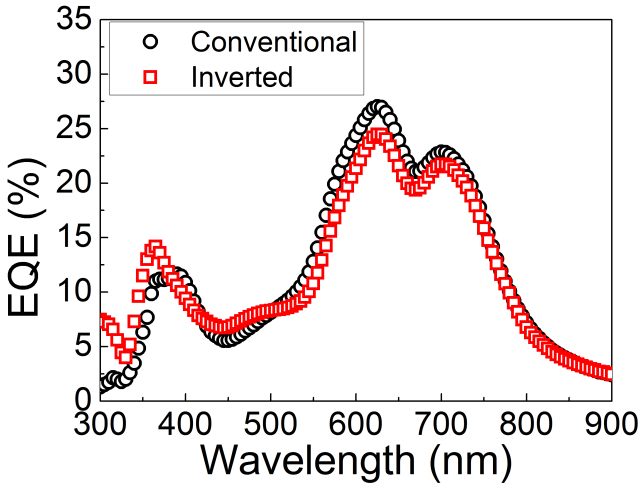

Figure 2.1: Simulation of EQE of conventional (circles) and inverted (squares) CuPc/ PTCBI devices with structure shown in text.

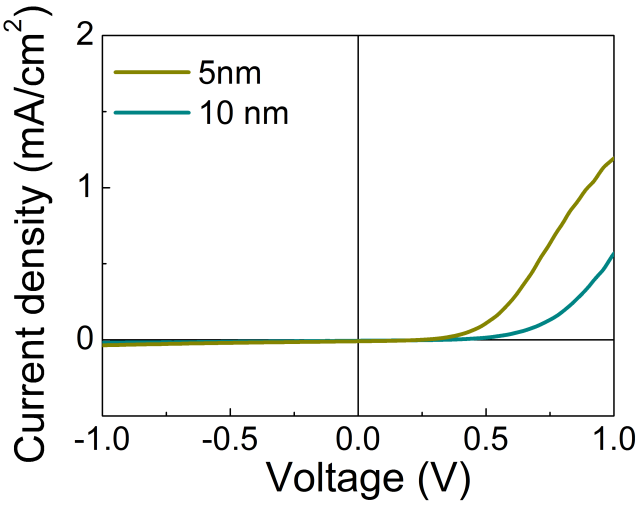

Figure 2.2: J-V characteristics of fully inverted CuPc/PTCBI devices quartz/Ag 100 nm/BCP 5(10) nm/PTCBI 30 nm/CuPc 15 nm/ITO 400 nm under 1 sun, AM1.5G illumination

limited by reducing the ITO thickness. The other optical loss in sputtered-ITO is the higher Fresnel reflection at the ITO/air interface compared to the glass/air interface in the conventional OPV case due to the difference in the refractive index of the materials ($n_{ITO} = 2.05$ and $n_{Glass} = 1.42$). Moreover, the sputtered-ITO exhibits higher sheet resistance resulting in the higher series resistance of inverted devices that can be solved by employing a metal grid subelectrode to reduced the distance between carrier generation and carrier collection.[101]

2.3 Inverted organic solar cells on reflective substrates

In this section, we explore inverted devices utilizing ITO as the top cathode while the organic layer sequence is kept the same as a conventional OPV device. In this structure, damage states which assist carrier extraction in BCP can form upon ITO deposition. Since the donor is adjacent to the metal anode, Ni is used as the electrode given its deep work function and reasonable reflectivity. Performance data for the inverted structure of quartz/Ni (100 nm)/CuPc (35 nm)/PTCBI (10 nm)/BCP (10 nm)/ITO (40 nm) are shown in Fig. 2.3. The power conversion efficiency peaks at $0.74 \pm 0.03\%$ under incident illumination power 98 mW/cm^2, with V_{OC}= 0.44 V and FF= 0.53. The V_{OC} increases without saturating as the incident power increases.[102] The peak $FF = 0.56$ at incident power 20 mW/cm^2. The dark current density-voltage (J_D-V) characteristics are fit to the modified ideal diode equation:[103] $J_D = J_S \left\{ \exp\left[\frac{q(V - J_D R_{SA})}{nkT}\right] - 1 \right\}$, giving an ideality factor $n = 1.78 \pm 0.004$, a series resistance (R_{SA}) $= 4.55 \pm 0.012\ \Omega \cdot \text{cm}^2$, and a reverse saturation current $J_S = 1.46 \times 10^{-7}$ A/cm^2.

Fig. 2.4 shows the comparison between the conventional and inverted CuPc/PTCBI devices in the dark and under 1 sun, AM1.5G illumination. The conventional device: glass/ITO/CuPc (20 nm)/PTCBI (25 nm)/BCP (10 nm)/Ag (100 nm) showed a V_{OC}

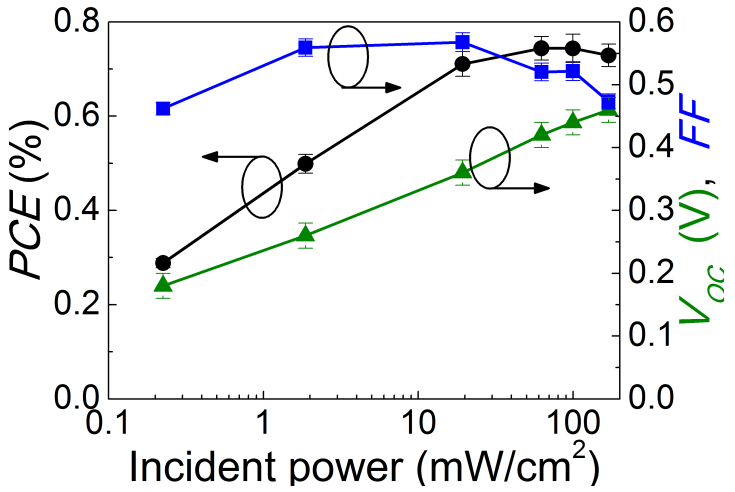

Figure 2.3: Performance of an optimized inverted CuPc/PTCBI device. PCE (circles), V_{OC} (triangles) and FF for the inverted device structure: quartz/Ni (100 nm)/CuPc (35 nm)/PTCBI (10 nm)
acbcp (10 nm)/ITO (40 nm) as a function of incident power density.

= 0.47 V, a $FF = 0.62$, and a responsivity $J_{SC}/P_{Inc} = 0.041$ A/W. Here, P_{Inc} is the incident optical power density under simulated AM1.5G illumination. These values result in a power conversion efficiency of $PCE = 1.2 \pm 0.1\%$, which is consistent with previous work.[104] Fits to the J_D-V characteristics give an ideality factor $(n) = 1.54$, $R_{SA} = 1.54\ \Omega \cdot \mathrm{cm}^2$, and a reverse saturation current density $(J_S) = 4.9 \times 10^{-8}$ A/cm^2. The high series resistance of the inverted device is due to the high sheet resistance of the sputtered-ITO.

The performance of the inverted device depends on the thicknesses of both the CuPc (t_{CuPc}) and PTCBI (t_{PTCBI}) layers, as shown in Fig. 2.5. For $t_{CuPc} < 35$ nm, the photocurrent (at 1 sun) increases monotonically with t_{CuPc}, due to the improved optical field distribution. In a thin-film layered stack, the optical field for long wavelength light is enhanced farther away from the reflective electrode due to interference effects.[15] Since CuPc absorbs in the 600-800 nm range,[105] as t_{CuPc} increases, the overall absorption in the CuPc layer increases, and is located near the D/A interface, resulting in higher photocurrent. On the other hand, the photocurrent is also lim-

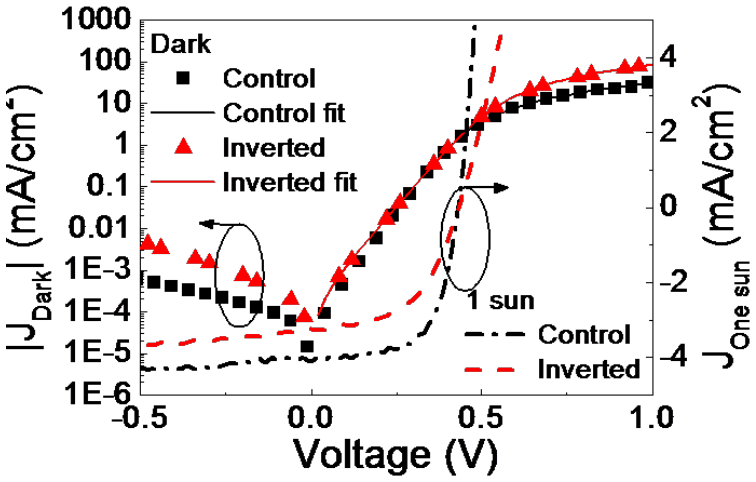

Figure 2.4: J-V characteristics of a conventional CuPc/PTCBI device in the dark (squares) and under 1 sun, AM1.5G illumination (dash-dotted lines), and for the optimized inverted structure in the dark (triangles), and under illumination (dashed line). The solid lines are fits to the measurement using theory in text.

ited by the exciton diffusion length (L_D) of the material, hence the enhancement in photocurrent reaches a plateau after 35 nm. Similarly, the roll-off of the measured photocurrent at larger thickness of PTCBI is partially due to the shift of the optical field intensity maximum away from the D/A interface, resulting in reduced exciton dissociation. From the fits to the data in Fig. 2.5, we obtain $L_D = 8 \pm 2$ nm for CuPc, and $L_D = 3 \pm 0.5$ nm for PTCBI, consistent with previously reported values for these materials.[15] The divergence between the simulated and measured data at $t_{CuPc} = 40$ nm is ascribed to a slightly decreased L_D, possibly a result of disruption of molecular stacking order as the film thickness is increased.[15] The V_{OC} does not vary significantly with CuPc thickness, as seen in Fig. 2.5(a). A $PCE = 0.74 \pm 0.03\%$ is achieved at a CuPc thickness of 35 nm, decreased to $PCE = 0.60 \pm 0.04\%$ at a thickness of 40 nm.

Figure 2.5(b) shows device performance as a function of PTCBI thickness, with $t_{CuPc} = 40$ nm. The low performance of the device with 0 nm PTCBI verifies that the

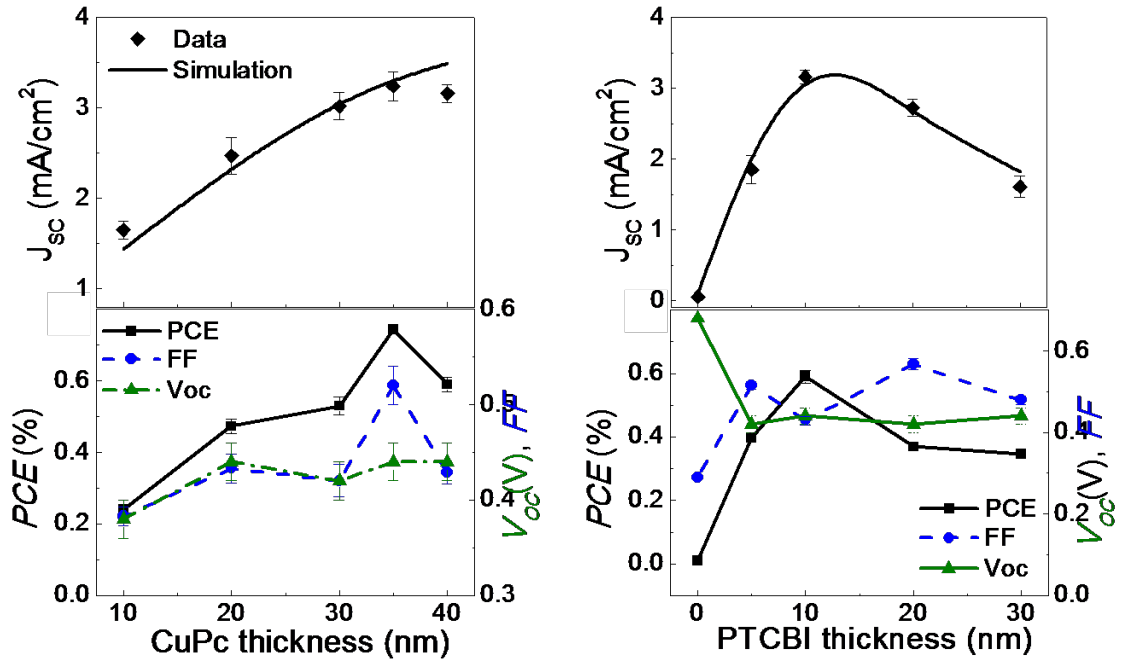

(a) (b)

Figure 2.5: Simulated (line) and measured short-circuit current (J_{SC}) at 1 sun intensity (diamonds) for quartz/Ni (100 nm)/CuPc (x nm)/PTCBI (y nm)/BCP (10 nm)/ITO (40 nm). Power conversion efficiency, PCE (squares), V_{OC} (triangles), and FF (circles) under simulated 1 sun, AM1.5G illumination are also shown. (a) $y = 10$ nm and x is varied from 10 to 40 nm. (b) $x = 40$ nm and y is varied from 0 to 30 nm.

CuPc-Ni interface does not form a photoactive Schottky diode, and the heterojuction is active in dissociating excitons. A fit to the data with $L_D = 8 \pm 2$ nm for CuPc and $L_D = 3 \pm 0.5$ nm for PTCBI is shown by the solid line. Similar to the case of varying CuPc thickness, V_{OC} and FF do not change significantly with PTCBI thickness, hence PCE follows the same trends as the photocurrent, peaking at $PCE = 0.6 \pm 0.04\%$ for $t_{PTCBI} = 10$ nm. For a 30 nm thick PTCBI layer, $PCE = 0.35 \pm 0.02\%$. When the thickness of the PTCBI layer is greater than 10 nm, the absorption in PTCBI occurs at distances considerably larger than the exciton diffusion length from the D/A interface. In this case, photogenerated excitons cannot be efficiently dissociated, resulting in a reduction in cell performance.

Using the experimentally determined values for L_D of CuPc and PTCBI, in Fig. 2.6 we simulate the photocurrent at 1 sun, AM1.5G illumination as a function of the donor and acceptor layer thicknesses. Exciton lifetimes of 2 ns are assumed for both CuPc and PTCBI.[15] The optimized photocurrent in Fig. 2.6 is 3.2 ± 0.002 mA/cm^2, consistent with experimental data. The inverted device exhibits inherently lower photocurrent compared to that of a conventional device due to the reverse active layer sequence. In order to maximize the absorption in the active layers, the material absorbing longer wavelength light should be placed farther away from the reflective electrode. In the next chapter we propose solutions to overcome this limit.

In summary, an inverted small-molecule organic photovoltaic cell employing a reflective Ni anode and an ITO cathode is demonstrated. Device performance is found to be in agreement with simulations with a measured peak power conversion efficiency of $0.74 \pm 0.03\%$. These devices have potential applications as power-generating coatings on a variety of flat or curved opaque surfaces.

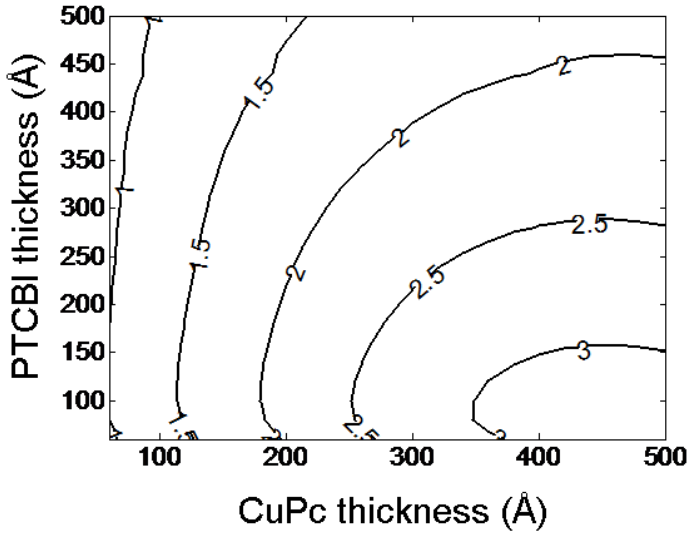

Figure 2.6: Simulated J_{SC} in an inverted CuPc/PTCBI solar cell as a function of CuPc and PTCBI thicknesses. The exciton diffusion lengths of CuPc and PTCBI are taken as 8 ± 2 nm and 3 ± 0.5 nm, respectively. The exciton lifetimes of 2 ns are used. Values of Ni anode, ITO cathode and BCP layer thicknesses are 100 nm, 40 nm, and 10 nm.

CHAPTER III

Inverted small-molecule photovoltaic cell with high open-circuit voltage

In the previous chapter, top-illuminated inverted OPVs utilize a bottom metal anode and a transparent top cathode without changing the deposition sequence of the organic layers. Although defect states assisting carrier extraction are present in the buffer layer in such structures, the resulting solar cells have limited efficiency because the optical field distribution is sub-optimal relative to the position of the donor and acceptor layers. For example, short wavelength light between $\lambda = 300$ nm and 550 nm is absorbed by the acceptor PTCBI, thus the acceptor should be placed near the reflective metal electrode. On the other hand, the phthalocyanine donor absorbs longer wavelengths, hence should optimally be adjacent to the transparent anode.

In this chapter, we demonstrate a top-illuminated organic solar cell based on vacuum-deposited SubPc and C_{60}, with an inverted layer structure optimized for maximum absorption of the optical field. Efficient carrier extraction is achieved by eliminating the BCP layer, thereby also eliminating the need for defect-induced carrier transport. In addition to preventing damage to the donor layer during ITO deposition, MoO_3 contributes to hole extraction.[106] The effects of varying the MoO_3 layer thickness and cathode materials are investigated. Inverted OPV cells on stainless steel substrates are also demonstrated.

3.1 Experimental procedure

To prepare both conventional and inverted devices, bare and ITO-coated glass substrates were cleaned by a standard solvent regimen followed by a UV-ozone treatment. [107] Materials were deposited at a rate of 2 Å/s for metals, and 1 Å/s for purified organics and MoO_3 in a high-vacuum thermal evaporation chamber (base pressure $< 4 \times 10^{-7}$ Torr). Prior to the deposition of the top contact, samples were transferred to an ultra-high-purity N_2 (<1 ppm O_2 and H_2O) where a shadow mask defining arrays of 1 mm-diameter circular openings was attached. The top ITO contact was sputter-deposited at a power of 40 W (0.2Å/s) and a pressure of 2 mTorr using Ar plasma.[61] All deposition rates and thicknesses were measured using quartz crystal monitors and calibrated by variable-angle spectroscopic ellipsometry. Device performance was measured in air using a semiconductor parameter analyzer in the dark and under illumination from a 150 W Xe lamp with AM1.5G filters using standard procedure.[108] Lamp intensity was varied with neutral density filters and measured by an NREL-calibrated Si photodiode. A transfer-matrix formalism was used to simulate the optical field and absorption, and to predict the J_{SC} of the device.[15] The aborption spectra of the materials were measured using a Lambda 1050 UV/Vis/NIR spectrophotometer.

3.2 Inverted solar cell with maximized absorption

The donor material that normally absorbs long wavelength light should be placed far away from the reflective electrode. The inverted structure design is restricted by the fact that they have low yield when the acceptor is in direct contact with an Ag contact. However, we find that shorting of the devices might be due to diffusion of Ag into the organic layers, and can be alleviated when the acceptor layer is thick and when other low-work-function metals are used. For devices using PTCBI as the acceptor,

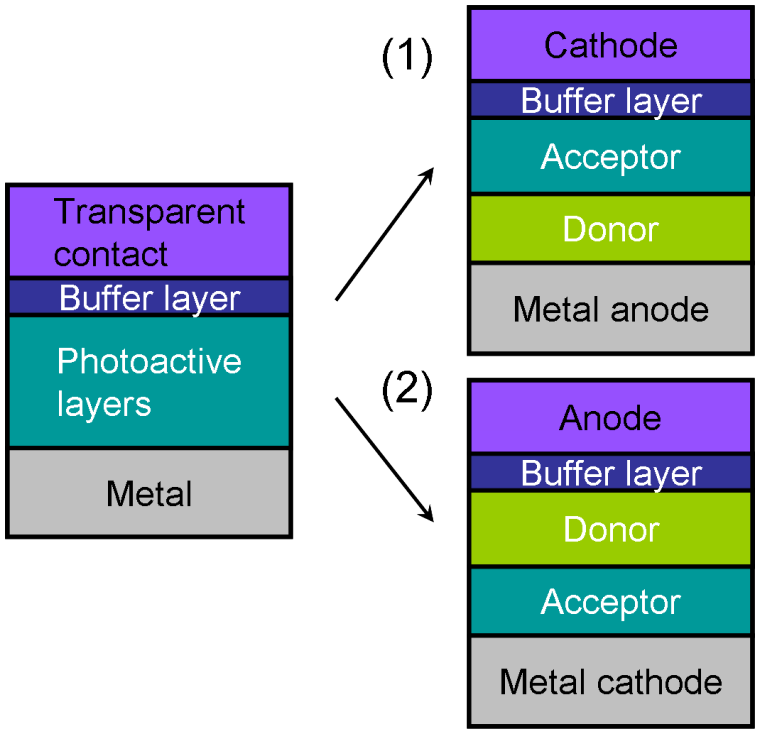

Figure 3.1: Two ways to construct photoactive layers in a planar inverted photovoltaic cell.

the thickness of PTCBI layer is kept thin due to the short exciton diffusion length of the material. When a material with a long exciton diffusion length such as C_{60} is used,[15] shorting of the devices is prevented, allowing for an inverted OPV structure optimized for optical field absorption. In Fig. 3.1 we show two different inverted structures, where only type (2) maximizes the absorption in the active layers.

To prevent damage to the donor during ITO deposition, a MoO_3 buffer layer is inserted into the following inverted structure: glass/Al 100 nm/C_{60} 50 nm/SubPc 9 nm/MoO_3 10 nm/ITO 40nm. This device showed $PCE = 0.86 \pm 0.08\%$, with responsivity $(R) = 0.032 \pm 0.002$ A/W, $FF = 0.48 \pm 0.01$ and $V_{OC} = 0.56 \pm 0.02$ V under 1 sun, AM1.5G illumination. For the inverted device, the ideality factor $n = 2.0 \pm 0.1$, $R_{SA} = 4.9 \pm 0.1\ \Omega \cdot \text{cm}^2$, and $J_S = (2 \pm 1) \times 10^{-5}$ A/cm^2 were obtained by fitting the J_D-V characteristics with the modified Shockley equation.[103] The conventional device with the structure: glass/ITO/SubPc 11nm/C_{60} 40 nm/BCP 10 nm/Al 100

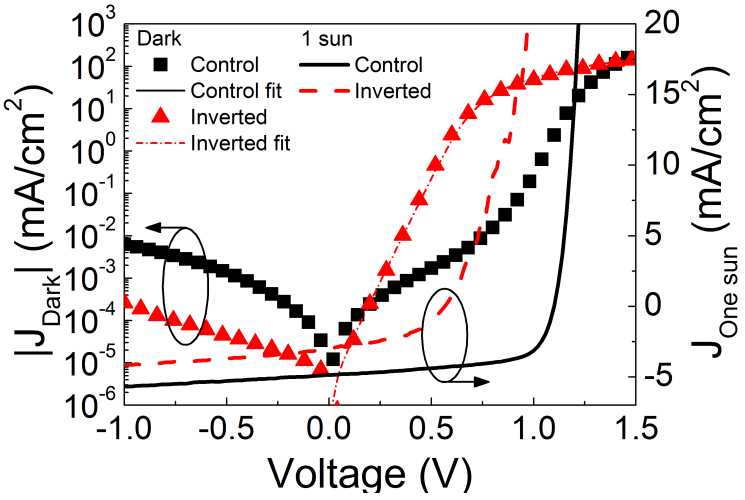

Figure 3.2: J-V characteristics of conventional and inverted SubPc/C_{60} devices with the structure: ITO-coated glass/SubPc 11 nm/C_{60} 40 nm/BCP 7 nm/Al 100 nm in the dark (squares) and under 1 sun, AM1.5G illumination (solid line); and glass/Al 100 nm/C_{60} 50 nm/SubPc 9 nm/MoO_3 10 nm/ITO 40 nm in the dark (triangles) and under 1 sun, AM1.5G illumination (dashed line). Fits according to the theory in text are indicated by thin solid lines.

nm achieved a responsivity of $R = 0.048 \pm 0.001$ A/W, $FF = 0.63 \pm 0.01$, and V_{OC} $= 1.10 \pm 0.02$ V, resulting in a $PCE = 3.3 \pm 0.1\%$ under 1 sun, AM1.5G illumination. A comparison of the J-V characteristics between the conventional device and inverted device is provided in Fig. 3.2.

The low V_{OC} of the inverted device is attributed to the low work function of sputtered ITO (4.03 eV) as compared to commercially-prepared and UV-ozone-treated ITO (4.7 eV) used in the conventional cell.[61] Large band bending occurs at the anode/donor interface when a shallow work function material is used as the anode, reducing the injection barrier at the anode/donor interface, thereby reducing V_{OC}.[109] Meanwhile, the change in contact work function also reduce the interface field, leading to an increase in the polaron pair recombination rate and a reduction in polaron pair dissociation rate. However, the V_{OC} change due to the field reduction is small, since the V_{OC} change follows $V_{OC} \propto k_b T \ln(k_{ppr}/k_{ppd})$, as indicated in Ref.[74] The

decreased fill factor is primarily due to the increased series resistance of the device from $R_{SA} = 0.24 \pm 0.05\ \Omega \cdot \mathrm{cm}^2$ to $R_{SA} = 4.9 \pm 0.1\ \Omega \cdot \mathrm{cm}^2$, a result of the higher contact resistance of the C_{60}/Al interface and sheet resistance of sputtered ITO.

3.3 Role of MoO_3

To increase V_{OC}, a series of inverted devices was fabricated with varied MoO_3 layer thicknesses from 10 nm to 70 nm, while using a low work function, 5 vol.% Mg:Ag cathode. It is found that V_{OC} increases from 0.78 ± 0.02 V to 1.02 ± 0.02 V when the thickness of MoO_3 layer thickness changes from 10 nm to 30 nm, and saturates for thicker films, as shown in Fig. 3.3(d). The responsivity peaks at 30 nm thick MoO_3,(Fig. 3.3(a)) consistent with optical simulations.

Previously it has been found that the ionization potential of MoO_3 increases logarithmically with layer thickness, leading to an increase in V_{OC}.[110] In an inverted device, since the MoO_3 is deposited on top of the organic layers, it is not possible to measure the energy level at the MoO_3/organic interface as a function of MoO_3 thickness. In Fig. 3.4 we show the measured absorption coefficient of MoO_3 films on quartz substrates, where the absorption edge corresponds to the MoO_3 band gap (E_g). It is found to increase by 0.43 eV as the thickness increases from 10 nm to 30 nm, and saturates thereafter. The absorption edge is also influenced by optical interference. After subtracting the optical effect, the increase in E_g is approximately 0.3 eV. The energy shift increases the build-in field in the active layers, thus improves the V_{OC} to 1.02 ± 0.02 V, close to that of the conventional device.

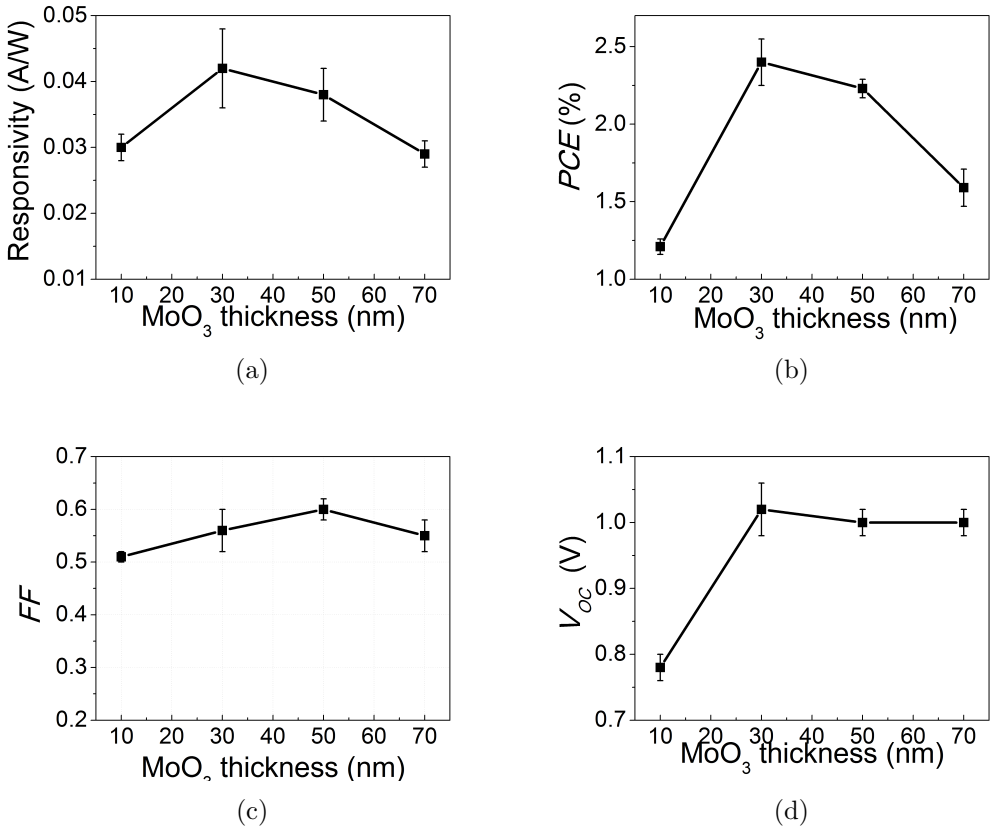

Figure 3.3: The influence of MoO_3 thickness on device characteristics under 1 sun, AM1.5G illumination. Sample structure: glass/Mg:Ag 100 nm/C_{60} 50 nm/SubPc 9 nm/MoO_3 x nm/ITO 40 nm. The MoO_3 thicknesses are x = 10, 30, 50, and 70 nm, respectively. (a) The dependence of R. (b) The dependence of PCE. (c) The dependence of FF. (d) The dependence of V_{OC}.

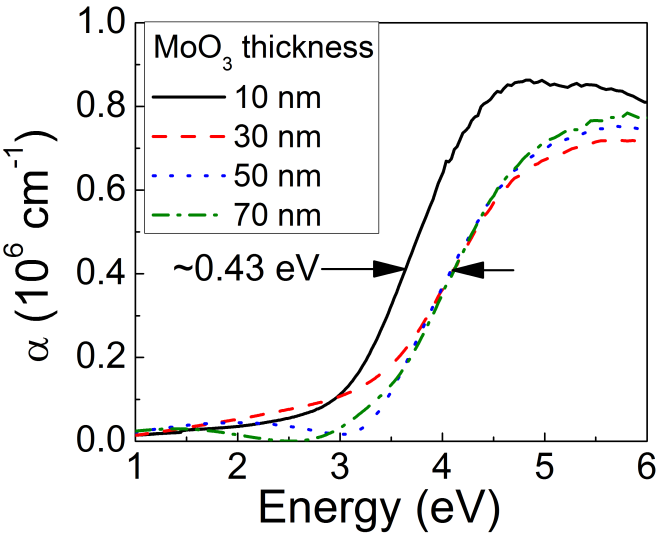

Figure 3.4: The absorption coefficient of MoO_3 on quartz for layer thicknesses of 10 (solid line), 30 (dashed line), 50 (dotted line), and 70 nm (dash-dotted line), respectively.

3.4 Effect of cathode work function on device performance

The influence of the cathode work function (Φ_{Cat}) on device performance is investigated, with results shown in Fig. 3.5. Values used for Φ_{Cat} are from Ref. [111]. Here, 100 nm thick layers of Ag, Al, Au and Mg:Ag were used as cathodes, with MoO_3 layer thicknesses of 10 nm and 50 nm. Note that devices with Ag as the cathode exhibit lower yield compared to other cathode materials. For devices with 10 nm MoO_3, V_{OC} increased significantly from 0.14 V to 0.91 V, while Φ_{Cat} decreased from 5.0 eV (Au) to 3.7 eV (Mg:Ag), as shown in Fig.3.5(d). The power conversion efficiency has a maximum at 2.23 ± 0.06 % for Mg:Ag cathode and 50 nm thick MoO_3 (see Fig. 3.5(b)). The increase in Φ_{Cat} results in more pronounced injection barrier increase at the metal/donor interface for devices using Au as the cathode than those that use Mg:Ag, hence the increase in MoO_3 thickness shows a much more dramatic improvement on V_{OC} (from 0.91 V to 1.02 V for Mg:Ag devices and 0.14 V to 0.7 V for Au-cathode devices.). We conclude that to achieve a high-efficiency inverted cell,

the electrodes and buffer layers must be chosen such that a sufficienty high built-in electric field (E_{bi}) is provided based on the energy levels of the photoactive layers.

3.5 Inverted organic solar cells on stainless steel substrates

Up until this point in Part I, the inverted solar cells have been built on glass or quartz substrates for the ease of substrate preparation. Since the inverted OPVs are grown on vacuum-deposited metal electrodes, the underlying substrate material does not affect device performance. In this section, the OPV devices are built on 76 μm stainless steel foil substrates (SUS). The SUS substrates are first smoothed by mechanical polishing to reduce surface roughness to below 3 nm, then further planarized by spun-cast PEDOT:PSS.

The method for polishing stainless steel involves the following steps: (1) The foil substrates are bonded to a 105 mm glass carrier disc using quartz wax heated to 80 ℃; (2) After cooled to room temperature, the glass carrier is mounted onto a vacuum chuck on the lapping jig; (3) The foils are then polished at 20 rpm under 1300 gram of force, using a free flowing slurry composed of 1 μm calcined aluminum oxide and DI water; (4) After polished for 30-45 minutes, the foils are removed from the glass carrier by melting the wax; (5) The foils are sonicated in xylene to remove the residual wax, then cleaned in acetone and boiling isopropanol. The resulting surface is non-directional, highly reflective and sufficiently smooth for thin-film solar cell fabrication. A layer of PEDOT:PSS is spin-casted at 1000 rpm for 30 seconds followed by 6000 rpm for 1 minute to provide a better planarized surface and better wetting for the metal electrode. Fig. 3.6 and Fig. 3.7 show the scanning electron microscope and atomic force microscope images of the foil substrates before and after polishing. The roughness is reduced from $>$ 200 nm to 3 nm. With further planarization using PEDOT:PSS, OPV cells can be grown on low-cost metal foil

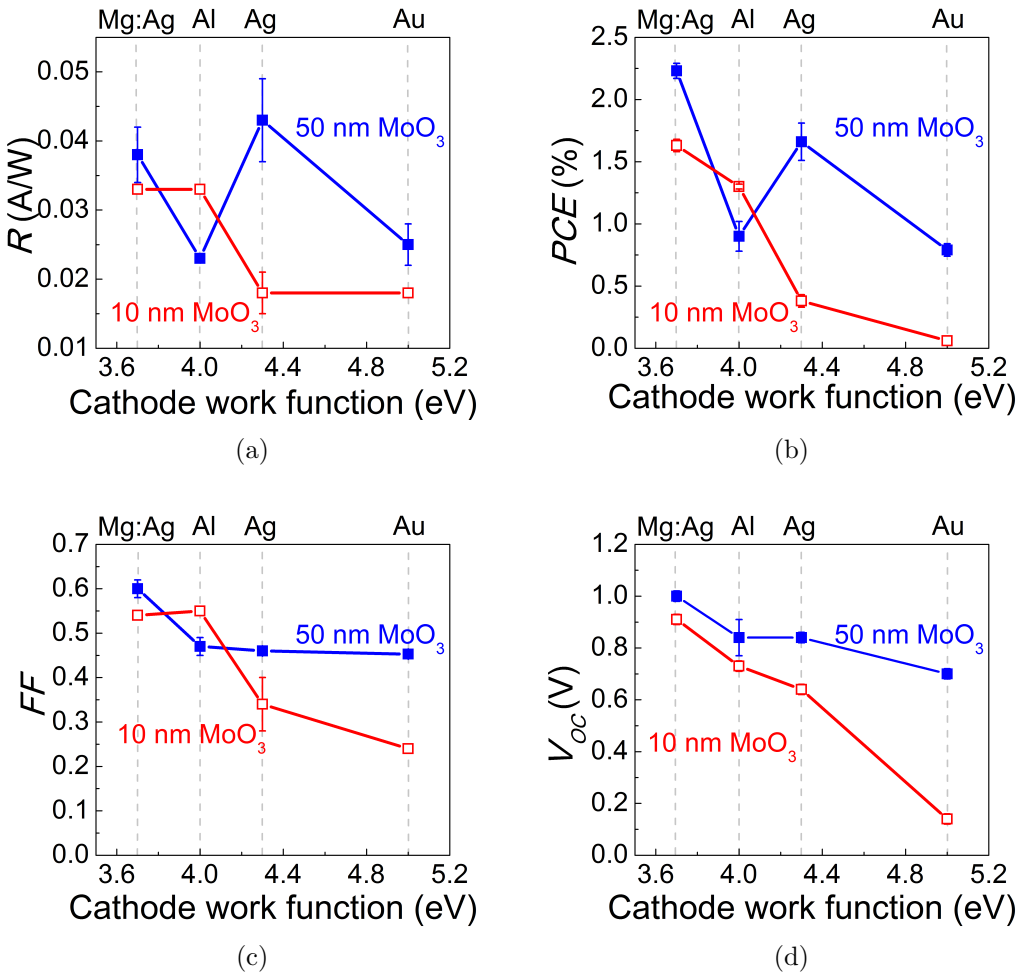

Figure 3.5: The influence of cathode work function (Φ_{Cat}) on device characteristics under 1 sun, AM1.5G illumination. Sample structure: glass/cathode 100 nm/C_{60} 50 nm/SubPc 9 nm/MoO_3 x nm/ITO 40 nm. The cathode is composed of Mg:Ag, Al, Ag, and Au respectively. The MoO_3 thicknesses are $x = 10$ nm (open symbols) and 50 nm (closed symbols). Cathode work functions (from Ref.[111]) are indicated by dashed vertical lines. (a) The dependence of R. (b) The dependence of PCE. (c) The dependence of FF. (d) The dependence of V_{OC}.

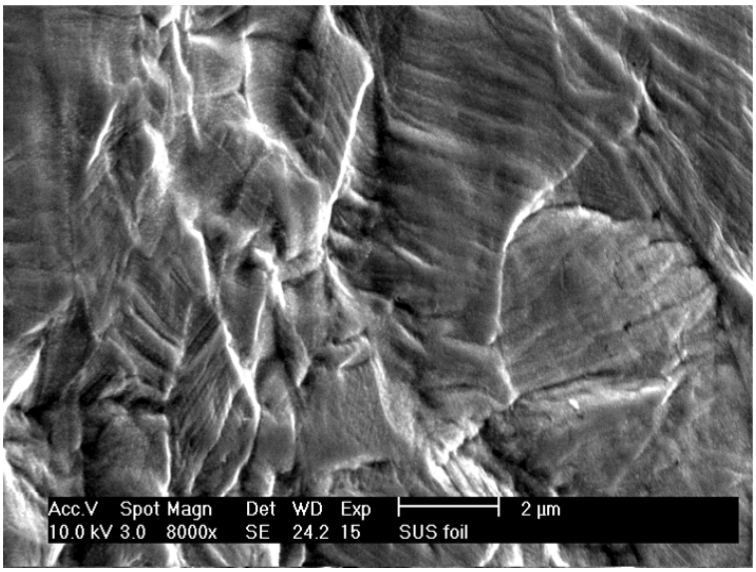

Figure 3.6: Scanning electron microscope image of stainless steel foil substrates before polishing.

substrates.

Fig. 3.8 shows the J-V characteristics of a conventional SubPc/C_{60} described in Section 3.2, as well as inverted devices on quartz and SUS, with the structure: substrate/Mg:Ag 100 nm/C_{60} 50 nm/SubPc 9 nm/MoO_3 30 nm/ITO 40 nm. The inverted device on SUS substrates exhibited a $PCE = 2.3 \pm 0.1$ %, with a $FF = 0.56 \pm 0.02$ and $V_{OC} = 1.0 \pm 0.02$ V. Moreover, $> 70\%$ yield can be achieved when PEDOT:PSS is used. The identical performance of inverted devices regardless of substrate materials indicates that the inverted device can be used in novel power-generating coating applications.

In conclusion, we demonstrate 2.4 ± 0.2 % power conversion efficiency in planar inverted small-molecule organic photovoltaic cells. A buffer between the cathode and photoactive layer is not necessary, allowing for device structure design optimized for active materials absorption. The inverted device performance can be substantially improved by employing a compound MoO_3/ITO anode and a shallow-work function

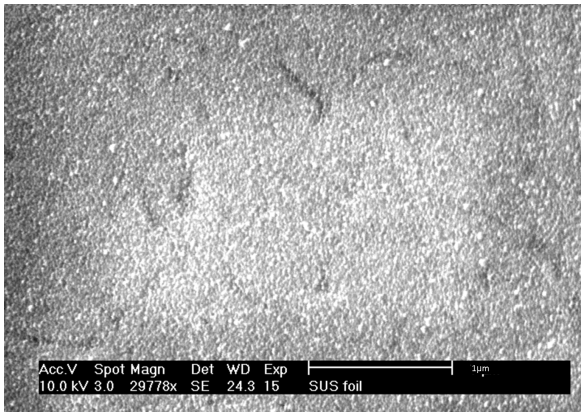

(a)

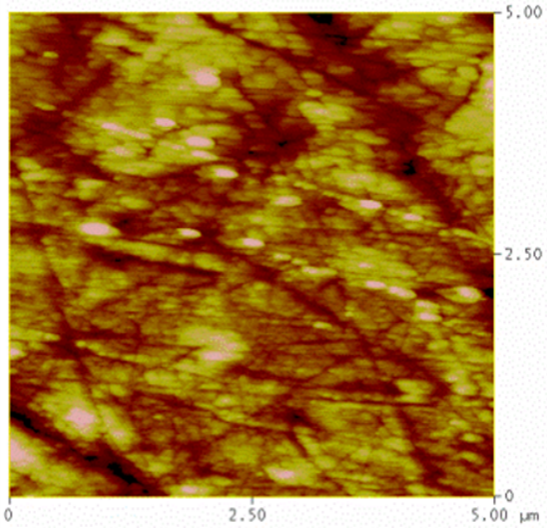

(b)

Figure 3.7: Stainless steel foil substrates after polishing. (a) Scanning electron microscope image. (b) Atomic force microscope image

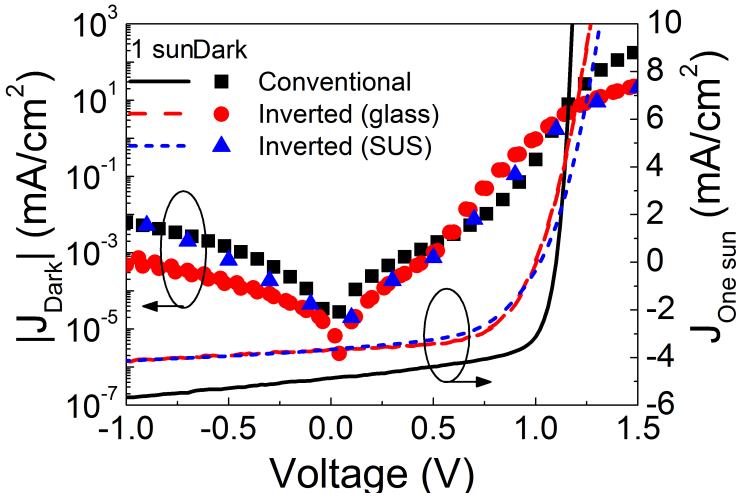

Figure 3.8: J-V characteristics of conventional and inverted SubPc/C_{60} devices on quartz and stainless steel substrates in the dark (symbols) and under 1 sun, AM1.5G illumination (lines).

cathode, which enhance the device V_{OC} by providing a sufficient built-in field. Finally, we demonstrate inverted OPVs can be fabricated on a variety of substrates and achieve nearly identical performance.

PART II

Reliability of organic photovoltaic cells

CHAPTER IV

Overview of organic photovoltaic cell reliability

The power conversion efficiency of organic photovoltaic cells has been improving steadily over time. State-of-the-art organic solar cells exhibit power conversion efficiencies of 8.9% for small-molecule bulk-heterojunction devices;[112] 9% for polymer bulk-heterojunction devices;[113] and 12% for tandem devices.[114, 115] The increase in efficiency has drawn more attention to studying the long-term operational lifetime of OPVs. In the second part of this thesis, we study the degradation mechanisms of small-molecule organic photovoltaic cells and propose methods to mitigate degradation pathways thus prolonging device lifetime. We will begin with a review of the current research progress in lifetime of organic solar cells, followed by investigations of burn-in degradation and long-term stability of OPVs.

In this chapter, we discuss laboratory characterization of OPV reliability, encapsulation techonologies and provide an overview of the state-of-the-art in OPV reliability research. We will organize the overview in terms of the stability of active materials, buffer layers and interfaces with a focus on small-molecule OPVs. Stability of polymer OPVs and materials will be used for comparison as they dominate literature on OPV

reliability. Extensive reviews of OPV lifetime research can be found in publications by Jørgensen et al., and Krebs.[116, 117, 118]

4.1 Characterization of device lifetime

4.1.1 Device lifetime

The lifetime of an OPV is evaluated by the operation time until the PCE reaches 80% (T80) or 50% (T50) of its initial value. Figure 4.1 shows an example of the normalized PCE decay curve and the two common ways lifetime is defined. It can be the time until the efficiency drops to 80% of the initial value (from PCE to PCE_{80}), or to 80% of an arbitrary point (from PCE′ to PCE'_{80}). Many studies have reported a fast burn-in loss at the beginning of the aging, followed by a slow decay, similar to the example shown in Fig. 4.1. The burn-in degradation has been attributed to the oxidation of the metal contact, or trap formation that prevents carrier collection or exciton diffusion.[119, 120, 121] The second slow decay is often approximated as a linear process and attributed to the diffusion of oxygen and water into the device active layers.[116] The diffusion process is not a linear function of time. The linearity may arise from the steady minute permeation of oxygen and water into device packaging, while the diffusion and degradation reactions occur at a much faster rate compared to aging time. For devices that exhibit large intial burn-in degradation, the T80 is more meaningful as an indicator of long-term operational lifetime.

4.1.2 Characterization methods

In Section 1.4.1, we have discussed typical characterization methods to evaluate the performance of an as-grown OPV device. The OPV lifetime measurements often involve examining the performance parameters as a function of time. Among all the characterization tools, testing device J-V characteristics as a function of time is the primary method to evaluate lifetime, as it directly provides the time dependence of

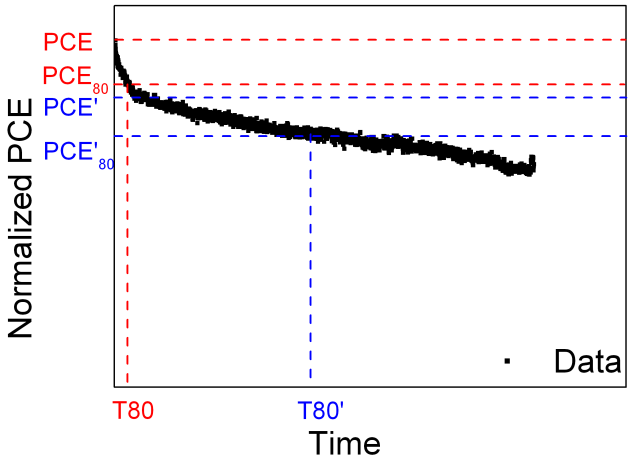

Figure 4.1: Typical power conversion efficiency decay curve and the two ways device lifetime T80 is defined.

photovoltaic parameters. In a lifetime study, the OPVs are aged under pre-defined environmental conditions (see Section 4.1.3), and the J-V characteristics under 1 sun, AM1.5G illumination are measured over time. If the dark J-V curve is also recorded, it can give insights of the changes in the series resistance, reverse saturation current and ideality factor.[15] An example of parameter degradation curves is shown in Figure 4.2.

In an OPV device, the donor and acceptor materials generally absorb in different wavelength ranges and may degrade at different rates. For devices that exhibit significant photocurrent loss, EQE is useful to identify the degraded species as it reveals the device photoresponse as a function of wavelength. A few studies measured the EQE before and after aging, and showed that some devices had uniformly degraded EQE, ascribed to reduced carrier extraction;[122, 123] while in other cases one material dominates the degradation process and the device EQE drops more significantly at the corresponding wavelength range.[124, 121] Device absorption data are necessary to interpret the change in EQE, as the drop could be due to a reduction in absorption, carrier generation, or an increase in quenching of carriers or excitons.

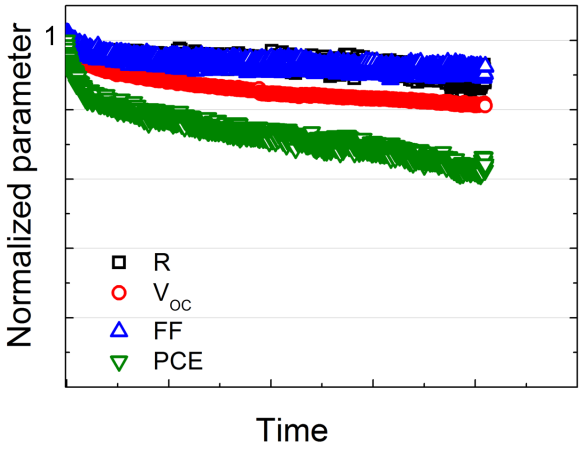

Figure 4.2: An example of photovoltaic parameters as a function of time for a mixed SubPc:C_{60} device with the structure: glass/ITO/MoO_3 10nm/ SubPc:C_{60} 55nm/PTCBI 8nm/Al 100nm.

Even when the *EQE* degrades uniformly across the entire spectral range, it is useful to test *EQE* throughout the aging experiment, instead of only at the beginning and the end, as it provides infomration about the relative degradation speed of one photoactive material to the other.

4.1.3 Testing conditions

Determining the lifetime and degradation mechanisms of a photovoltaic cell is a complex task that requires highly controlled environment and testing conditions. For inorganic photovoltaics, there are well-established qualification test standards by the International Electrotechnical Commission (IEC), such as IEC 61215 for crystalline silicon terrestrial photovoltaic modules, IEC 61646 for thin-film terrestrial photovoltaic modules, and IEC 62108 for concentrator photovoltaic modules and assemblies. Scientists have gained considerable knowledge into the degradation mechanisms of inorganic solar cells after decades of research. For example, studies on crystalline Si PV systems have suggested that degradation is often due to the failure in solder joints or interconnects, or degradation of encapsulants.[125, 126] Amorphous Si solar

cells suffer from light-induced degradation reversible by thermal annealing.[127] On the other hand, organic PV technologies are relatively young and diverse. The wide variety of OPV materials, device architectures, and processing techniques makes it difficult to have a universal standard to study device lifetime. Reese et al. published a consensus on OPV test conditions aiming to provide a better guideline for reporting reliability results.[128] The article summarizes OPV test conditions in terms of aging and testing light source, environment, humidity, temperature, and electrical load conditions, as shown in Table 4.1. Following the standardized approach is useful as it allows for comparing data among different laboratories and OPV systems.

Environmental factors may cause different device degradation routes, which can be separated by using controlled aging conditions. In 2008, Gevorgyan et al., introduced a setup where the oxygen level, humidity, atmosphere, temperature and light intensity are individually controlled.[129] In this setup, up to 2 devices are placed in an atmospheric chamber with quartz windows for illumination, electrical feedthroughs and flanges connected to vacuum pumps and gas sources. Temperature control is achieved by applying cooling fluid or heating blocks. Environment conditions are measured by pressure gauges, thermocouples and oxygen and humidity sensors connected to the chamber. When ambient or artificial atmosphere is used, fans are used to eliminate temperature variations within the atmospheric chamber. The setup provides strictly controlled environments for aging studies yet is bulky in size. Given the testing area is limited by the illumination area of the solar simulator, it is neither efficient nor cost-effective to have a large atmospheric chamber. The authors later improved the testing setup to a more compact design, where 4 substrates (16 devices) can be studied simultaneously in different gas environments.[130] Reese et al., demonstrated a simple miniature atmospheric chamber that also serves as encapsulation.[131] In the atmospheric chamber, the back of the device substrate is directly pressed against an o-ring seal. The device is then capped with either an encapsulation cover with a

Table 4.1: Overview of different types of test protocols adapted from Ref. [128]

Three levels							
Basic (Level 1) **Intermediate (Level 2)** **Advanced (Level 3)**			"Hand held" measurements using the simplest equipment and few conditions Fixed conditions and protocols suited for most labs Standardized tests applied in certified labs. Extended range of parameters to monitor, etc.				
Test type	**Dark**			**Outdoor**			
Test ID	ISOS-D-1 Shelf	ISOS-D-2 High temp. storage	ISOS-D-3 Damp heat	ISOS-O-1 Outdoor	ISOS-O-2 Outdoor	ISOS-O-3 Outdoor	
Light source	None	None	None	Sunlight	Sunlight	Sunlight	
Temp.[a]	Ambient	65/85 °C	65/85 °C	Ambient	Ambient	Ambient	
Relative humidity (R.H.)[a]	Ambient	Ambient (low)	85%	Ambient	Ambient	Ambient	
Environment[a]	Ambient	Oven	Env. chamber	Outdoor	Outdoor	Outdoor	
Characterization light source	Solar simulator or sunlight	Solar simulator	Solar simulator	Solar simulator	Sunlight	Sunlight and solar simulator	
Load[b]	Open circuit	Open circuit	Open circuit	MPP or open circuit	MPP or open circuit	MPP	
Test type	**Laboratory weathering testing**			**Thermal cycling**			
Test ID	ISOS-L-1 Laboratory weathering	ISOS-L-2 Laboratory weathering	ISOS-L-3 Laboratory weathering	ISOS-T-1 Thermal cycling	ISOS-T-2 Thermal cycling	ISOS- T-3 Thermal cycling	
Light source	Simulator	Simulator	Simulator	None	None	None	
Temp.[a]	Ambient	65/85 °C	65/85 °C	Between room temp. and 65/85 °C	Between room temp. and 65/85 °C	−40 to +85 °C	
Relative humidity (R.H.)[a]	Ambient	Ambient	Near 50%	Ambient	Ambient	Near 55%	
Environment/setup	Light only	Light & Temp.	Light, Temp. and R.H.	Hot plate/oven	Oven/env. chamb.	Env. chamb.	
Characterization light source	Solar simulator	Solar simulator	Solar simulator	Solar simulator or sunlight	Solar simulator	Solar simulator	
Load[b]	MPP or open circuit	MPP or open circuit	MPP	Open circuit	Open circuit	Open circuit	
Test type	**Solar-thermal-humidity Cycling**						
Test ID	ISOS-LT-1 solar-thermal cycling		ISOS-LT-2 solar-thermal-humidity cycling	ISOS-LT-3 solar-thermal-humidity-freeze cycling			
Light source	Simulator		Simulator	Simulator			
Temp.	Linear or step ramping between room temp. and 65 °C		Linear ramping between 5 and 65 °C	Linear ramping between −25 and 65 °C			
Relative humidity (R.H.)	Monitored, uncontrolled		Monitored, controlled at 50% beyond 40 °C	Monitored, controlled at 50% beyond 40 °C			
Environment/setup	Weathering chamber		Env. chamb. with sun simulation	Env. chamb. with sun simulation and freezing			
Characterization light source	Solar simulator		Solar simulator	Solar simulator			
Load[b]	MPP or open circuit		MPP or open circuit	MPP or open circuit			

[a] The ambient conditions are defined as 23 °C/50%RH in general, and 27 °C/65%RH accepted in tropical countries according to ISO 291(2008): Plastics—Standard atmospheres for conditioning and testing.

[b] Open circuit refers to a simply disconnected device or device connected to a sourcemeter set to 0 current.

getter to maximize device lifetime, or a cover with gas ports to control the chamber environment. The devices are connected by pogo pins and electrical feedthroughs to the source measurement unit. The authors also proposed methods to incorporate temperature control. A Ca test (See Section 4.2.1) showed that the chamber has a moisture ingress of $\sim 0.5\mu g/day$ when desiccant is included. This atmospheric chamber design minimizes the error in illumination intensity as no quartz window is used and the light intensity on the substrate can be directly calibrated.

Jørgensen et al., proposed that commercial weather chambers should be used to control the environmental factors.[118] The commercial chambers accurately control temperature and humidity. Cycling of temperature and illumination intensity is also programmable. Such a setup provides consistent control of aging environments. However, the gas composition cannot be changed and the equipment may be costly.

4.1.4 Accelerated aging

The time it takes for an OPV to degrade can take months to years, therefore accelerated aging is of interest.[132, 120] An acceleration factor such as light intensity, temperature or humidity is applied to the device and the degradation rate is measured under different conditions. Device lifetime under normal operating conditions can be extrapolated.

The degradation rate is extracted by assuming a linear or exponential decay of the parameter, viz.:

$$f(t) = f(t_0)\,(1 - k_{deg}t) \tag{4.1}$$

$$f(t) = f(t_0)\exp\left(-k_{deg}t\right) \tag{4.2}$$

Here $f(t)$ represents the parameter of interest and k_{deg} is degradation rate. Degradation of OPVs generally exhibit a fast burn-in degradation for the initial few hours then a linear decay onwards, therefore Eq. 4.1 is used.[133, 129, 121, 118, 134] Material

systems that exhibit exponential degradation are rarely seen in the literature.[135]

Lifetime testing at elevated temperature is the most commonly used accelerating test. The temperature dependence of degradation rate follows the Arrhenius relationship:

$$k_{deg} = A \exp\left(-\frac{E_A}{k_B T}\right). \tag{4.3}$$

Here A is the prefactor, E_A is the activation energy, k_B is Boltzmann constant and T is temperature. Therefore the acceleration factor from temperature T_1 to T_2 is defined as:

$$K = \frac{k_{deg}(T_1)}{k_{deg}(T_2)} = \exp\left[\frac{E_A}{k_B}\left(\frac{1}{T_1} - \frac{1}{T_2}\right)\right]. \tag{4.4}$$

The activation energy is highly material-dependent in OPVs. Schuller et al., studied the degradation of MDMO-PPV/[6,6]-phenyl-C_{61}-butyric acid methyl ester (PCBM) bulk heterojunction solar cells and obtained an activation energy of 300-350 meV for photocurrent degradation.[133] Gevorgyan et al., investigated the aging of poly(3-hexylthiophene) (P3HT)/PCBM and found the activation energy of efficiency degradation is 103 meV when aged in ambient atmosphere and 29 meV when aged in N_2.[129] Moreover, competing degradation mechanisms may have different dependence on temperature, making projection of device lifetime from one temperature to another difficult. Nonetheless, high-temperature accelerated testing does provide useful insights on degradation kinetics, however, care must be taken to verify no new degradation mechanism is introduced at higher temperature.

Elevated humidity can also be used in accelerated testing. Voroshazi et al., quantitatively analyzed the shelf-life of devices as a function of humidity.[136] It was found that high humidity level caused P3HT/PCBM OPVs to degrade faster when PEDOT:PSS was employed as the hole transport layer, and the effect of humidity was not as strong when MoO_3 serves as the hole transport layer, despite that both

transport layers are water-soluble.

Another method to accelerate device aging is to apply concentrated illumination. Hermenau et al., examined the accelerated aging of zinc phthalocyanine (ZnPc):C_{60} OPVs and concluded that the degradation can be described by the total extracted charge carriers.[137] The degradation of device PCE is only proportional to the number of total extracted carriers when aged under white LEDs for intensities varied between 163-872 mW/cm^2. However, the proportionality does not hold when different intensities of blue illumination were used, and devices aged under different wavelength light degraded differently. Therefore it is unclear if the relationship between extracted carriers and lifetime holds for devices aged under AM1.5G illumination, given the spectrum may play an important role in degradation behavior.

4.1.5 Data reporting

The OPV lifetime is affected by numerous factors, therefore all the necessary details in terms of device performance, aging conditions and testing conditions need to be reported. The device T80, reflected by the degradation in PCE, is a combined result of the change in R, V_{OC} and FF, which should all be shown. Moreover, the decay curve of the dominant degradation parameter should be provided. The aging conditions such as the encapsulation of the device, testing environment, temperature, humidity, aging light spectrum and intensity, and electrical load conditions need to be clarified, allowing for comparison across different laboratories.

4.2 Hermetic packaging

Studies have shown that organic semiconductors are sensitive to moisture and oxygen, thus effective encapsulation is necessary to extend device operational lifetime.[138, 116] In this section we review hermetic packaging techniques that have been applied to organic optoelectronic devices.

4.2.1 Evaluation of packaging quality

Generally, the packaging quality is assessed by the water vapor transmission rate (WVTR) of the barrier. So far, no definitive WVTR value for long-lifetime organic devices has been suggested, given the moisture sensitivity and degradation mechanisms of organic devices are highly material-dependent. Burrows et al., proposed that WVTR below 10^{-5} g/(m^2d) is required to achieve long operational lifetime in OLEDs.[139] Cros et al., investigated the effect of water vapor on the lifetime of conventional and inverted polymer devices and concluded that lifetime of several years can be achieved with barrier WVTR of $\sim 10^{-3}$ g/(m^2d).[140] Currently there is no conclusion on whether OPVs are more resistant to humidity than OLEDs, yet it is likely that long operational lifetime can be achieved in OPVs with low-cost barrier technologies.

Standard ASTM F1249-06 provides a guideline for measuring the WVTR of film or sheeting barriers. To measure ultra-low WVTR in a laboratory, the Ca test is one of the most widely employed methods owing to its easy implementation. The test is based on the reaction of Ca with water and oxygen, resulting in the change in the color (opaque to transparent) and conductivity (conductive to insulating) of the Ca thin film. The reactions involved in the Ca test are:

$$\mathrm{Ca} + \mathrm{H_2O} \longrightarrow \mathrm{CaO} + \mathrm{H_2},$$
$$2\,\mathrm{Ca} + \mathrm{O_2} \longrightarrow 2\,\mathrm{CaO}, \text{ and}$$
$$\mathrm{CaO} + \mathrm{H_2O} \longrightarrow \mathrm{Ca(OH)_2}.$$

In a Ca test, a thin film of Ca is deposited on the substrate, which is then encapsulated with the barrier in test and placed in a highly controlled environment. Accelerated testing may be employed where the temperature and humidity of the ambient are elevated. The transparency or conductivity of the Ca film is monitored over time and WVTR is calculated accordingly. This method can differentiate between pinhole-

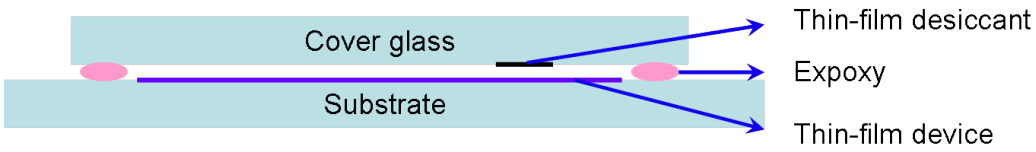

Figure 4.3: Schematic of glass-on-glass encapsulation. The dimensions are not to scale.

induced permeation and bulk permeation based on the uniformity of the property change. Schubert et al., provided full test layout and calculation methods.[141]

4.2.2 Encapsulation methods

A glass lid with UV-cured epoxy resin has often been used for encapsulation. The sample is placed in an inert gas environment such as N_2. After the epoxy is dispensed around the edges, a glass lid is placed on top forming a seal around the perimeter. The epoxy is then cured under a UV lamp. Moreover, a thin-film getter such as BaO or CaO is used to adsorb any residual water and oxygen in the encapsulated volume. A schematic of glass-on-glass encapsulation is shown in Figure 4.3.

The glass encapsulation is rigid and not compatible with flexible OPV design, therefore researchers have explored thin-film encapsulation and barrier lamination. In a thin-film encapsulation process, an inorganic thin film is deposited as the barrier via atomic layer deposition, plasma-enhanced chemical vapor deposition, or sputtering. [142] Currently, the inorganic materials for thin-film encapsulation mostly comprise Si- or Al-based oxides or nitrides. Research efforts are focused on reducing the defect density, thus WVTR, in the barrier. Lamination of a barrier film directly onto the device is suitable for roll-to-roll processing. WVTR on the order of 10^{-2} g/(m^2d) has been reported for OPV modules with a laminated multi-layer barrier.[2]

4.3 Stability of photoactive materials

The photoactive layers in an OPV are susceptible to degradation, as they are at higher energy excited states. The degradation of active materials directly leads to deterioration of device performance, thus understanding active materials stability is important for improving device lifetime. Organic materials are prone to photochemical reactions such as bond brokerage, crosslinking reactions and rearrangements.[117] Finding active materials with good photostability is a necessary but insufficient condition to long-lifetime OPVs, thus is an important starting point.

Fullerene C_{60} has been the most widely-used acceptor material due to its wide absorption range, long exciton diffusion length and charge mobility.[143, 15] The photostability of C_{60} has been studied prior to its utilization in organic photovoltaic devices. Taylor et al. first reported photoinduced decomposition of C_{60} in solution.[144] Rao et al. showed photoinduced polymerization of C_{60} thin films in an oxygen-free environment. The vacuum-deposited C_{60} thin film was polymerized up to C_{600} as shown in laser desorption mass spectroscopy data after 12 hours of illumination under a 300W Hg lamp. However, no similar phototransformation has been observed in OPV degradation studies. It is possible that such phototransformation requires a large dose of UV illumination, which is hard to achieve since ITO absorbs the majority of light below 320 nm.

Besides intrinsic degradation, C_{60} is also affected by environmental factors such as water and oxygen. Matsushima et al. investigated the effect of absorbed oxygen and water in a C_{60} OTFT.[145] An increase in the electron trap density was observed, which decreased the mobility in the material. The degradation was reversed by thermally annealing the C_{60} thin film. Lessman et al. studied long-term reliability of a planar heterojunction ZnPc/C_{60} solar cell at different temperatures and under illumination of a blue LED at 475 nm.[124] The devices exhibited a significant increase in sheet resistance, a decrease in FF and a drop in photocurrent after 1200 h of ag-

ing. The loss in photocurrent was primarily due to the lesser contribution from C_{60}, as indicated by EQE. The time-of-flight matrix-assisted laser desorption/ionization spectroscopy (MALDI) data suggested that the degradation is due to photooxidization of C_{60}. Similar incorporation of oxygen in C_{60} was found in a degradation study of P3HT/C_{60} OPV.[132] The authors proposed that oxygen diffused through pinhole defects in the electrode then further diffused laterally, therefore attacking the device. The donor polymer was not significant affected in either study.

Opposite results were found when the active layer is based on a mixed heterojunction comprised of ZnPc and C_{60}. In another study on degradation of a ZnPc:C_{60} OPV, it was found that oxidation of the donor material is far more pronounced than C_{60}. Hermenau et al., studied the effects of water and oxygen on a mixed ZnPc:C_{60} bulk heterojunction OPV aged in isotopically labeled $H_2^{18}O$ and $^{18}O_2$:N_2.[146] By combining X-ray photoelectron spectroscopy (XPS) and time-of-flight secondary ion mass spectrometry (TOF-SIMS), the authors identified that water molecules causing oxidation of ZnPc was the main degradation mechanism. By mapping the oxygen content using TOF-SIMS, it was found that the oxygen diffused through pinholes in the Al electrode. The oxidation was accelerated by illumination and does not occur when aged in dry O_2. The acceptor C_{60} was not affected by oxygen in this case. Water caused the device to fully degrade within hours, while devices aged in dry N_2 exhibit a T80 of 405 h.

Active materials in polymer OPVs may also degrade. Seemann et al., investigated the degradation of P3HT:PCBM solar cells by J-V characteristics, impedance measurements and charge extraction by linearly increasing voltage.[147] The degradation in the presence of oxygen was ascribed to photochemical formation of carbonyl and carboxylic groups that trap electrons. The degradation was accelerated by illumination and partially reversible.

4.4 Degradation of non-active layers and interfaces

Deterioration of buffer layers and the electrode/organic interface can also degrade performance. The metal electrode in an OPV device is usually deposited via thermal evaporation, which leads to pinhole defects in the thin film. Environmental contaminants such as water and oxygen molecules will migrate along the defects and cause metal oxidation at the metal-organic interface.[146] Several studies have shown that water-induced oxidation of electrodes does not depend strongly on illumination.[146, 148] Studies have found that the metal electrode may diffuse through the organic layer. However, whether the metal diffusion deteriorates device performance is controversial.[146, 132]

PEDOT:PSS is a common hole transport layer that is extensively used in polymer OPVs. Yamanari et al., found that the hygroscopic and acidic nature of PEDOT:PSS accelerated oxidation of the Al electrode, while devices using MoO_3 or no buffer layer showed superior lifetime.[149]

Using an inverted device structure may prolong device lifetime. Zimmermann et al., studied the degradation of a top-illuminated inverted device using PEDOT:PSS and metal grid as the transparent top contact.[150] The devices were packaged and then aged under a sulfur plasma lamp at 1 sun, AM1.5G illumination (AM1.5G) and 50℃. Auger electron spectroscopy showed that the metal contact was partially oxidized leading to a drop in FF. The lifetime was improved when a metal with a semiconducting oxide such as Cr was used. Norrman et al., proposed that phase segregation of PEDOT:PSS and oxidation occuring at the PEDOT:PSS/active layer interface was the main degradation mechanism for a bottom-illuminated inverted cell.[151]

Schäfer et al., examined the degradation of ZnPc:C_{60} bulk heterojunction devices aged under illumination and in inert gas.[138] The degradation was ascribed to a change in the ITO work function caused by illumination in the UV. The lifetime was

investigated within a very short aging period (7 minutes) and the effect on long-term degradation is unclear.

In Chapter V, we present a compact testing system that is used to measure the degradation of OPVs at elevated temperature. In Chapter VI, we will examine the physical mechanisms leading to the burn-in degradation in small-molecule OPV photocurrent, and propose methods to mitigate the process. In Chapter VIII, we examine the activation energy, degradation mechanisms and long-term stability of small-molecule organic photovoltaic cells.

CHAPTER V

Experimental setup for long-term reliability testing

112 In this chapter, we present an, automated indoor laboratory solar cell testing system for studying long-term operational lifetime of organic photovoltaic cells. As discussed in Chapter 1, OPVs are susceptible to degradation when exposed to water and oxygen. All devices are encapsulated, and tested under continuous AM1.5G illumination and at different temperatures, in accordance with stability measurement protocol ISOS-L-1.[128] The testing system is fully automated with individual substrate temperature control, device current-voltage (I-V) measurement and data analysis and logging.

5.1 Light source

The illumination is provided by an AM1.5G, Class AAA solar simulator with an illumination area of 8 inch $\times$ 8 inch. Previous lifetime studies have employed single color or white LEDs and sulfur plasma lamps as illumination sources.[124, 152] As we will show in Chapter VI, the OPV aging behavior depends on the number of photons absorbed, therefore the incident spectrum may have little effect on device degradation. However, for devices employing donor and acceptor materials with small absorption overlap, the illumination source may play a bigger role on device degradation, given each active material responds strongly to different parts of the spectrum. Xenon lamps should be used as the light source for indoor lifetime testing, as the spectral

match best simulates the aging conditions under a solar spectrum.

The solar simulator intensity is controlled by a built-in photodetector and proportional - integral - derivative controller (PID controller). The intensity fluctuation caused by Xenon bulb flickering is monitored by a 1 cm^2 Si photodectector during I-V measurement to minimize error in data analysis.

5.2 Device characterization

The device aging behavior is analyzed by measuring the I-V characteristics over time. The system utilizes custom-built printed circuit boards for device mounting, a Keithley 2400 sourcemeter for measurement, and a Keithley 2700 datalogger with 7705 module combined with custom-built printed circuit boards (PCBs) for device switching.

5.2.1 Device encapsulation and mounting

Each substrate contains four 1 cm^2 devices with the area defined by the overlap between 1 cm wide strips of ITO anode and an Al cathode. The devices are encapsulated by UV-cured epoxy and cover glass. Prior to encapsulation, a 50 nm thick Ca film is thermally evaporated on the cover glass to provide visual aid of packaging quality.[141] A thin-film BaO desiccant is attached to the cover glass to adsorb any residual moisture within the package. The schematic of the packaged device is shown in Fig. 5.1.

Once encapsulated, the substrate is connected to a carrier board, which then connects to the motherboard in the testing system. Individual carrier boards enable easy device mounting and minimal interference with the devices already on test. The electrical connection between the substrate and the carrier board contact pads is achieved by silver paste and gold wire, which are found to be the most reliable

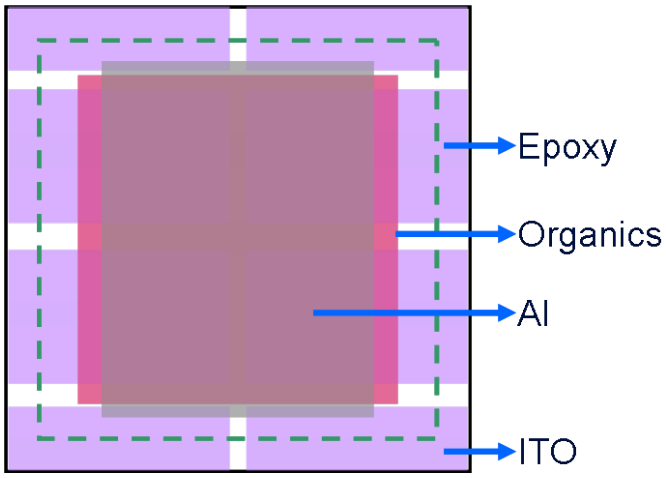

Figure 5.1: Schematic of a packaged device

connection over long duration testing.

5.2.2 Device switching and measurement

The electrical connection between the computer, instruments and devices for switching and measurement is defined by custom-built PCBs. The circuit layout for the main switching board is shown in Fig. 5.2.

The 24-pin connectors link to a motherboard that holds three carriers. Each pair of device electrical contacts are connected to a relay that switches between measurement and idle conditions. A pair of 12-pin female headers are used to set the device electrical connection during idle condition, such as short-circuit, open-circuit or at maximum power point (MPP). The relays interface with the computer via Keithley 2700 datalogger and 40-channel 7705 module. One channel on the module is dedicated to a calibrated Si photodiode to monitor the light intensity. When a device is measured, the datalogger controls the relay to switch to the sourcemeter for I-V characteristic scanning. Immediately after measurement, the module switches to measure the current output from the Si photodiode in order to obtain the light intensity for data analysis, and the device is set back to idle condition.

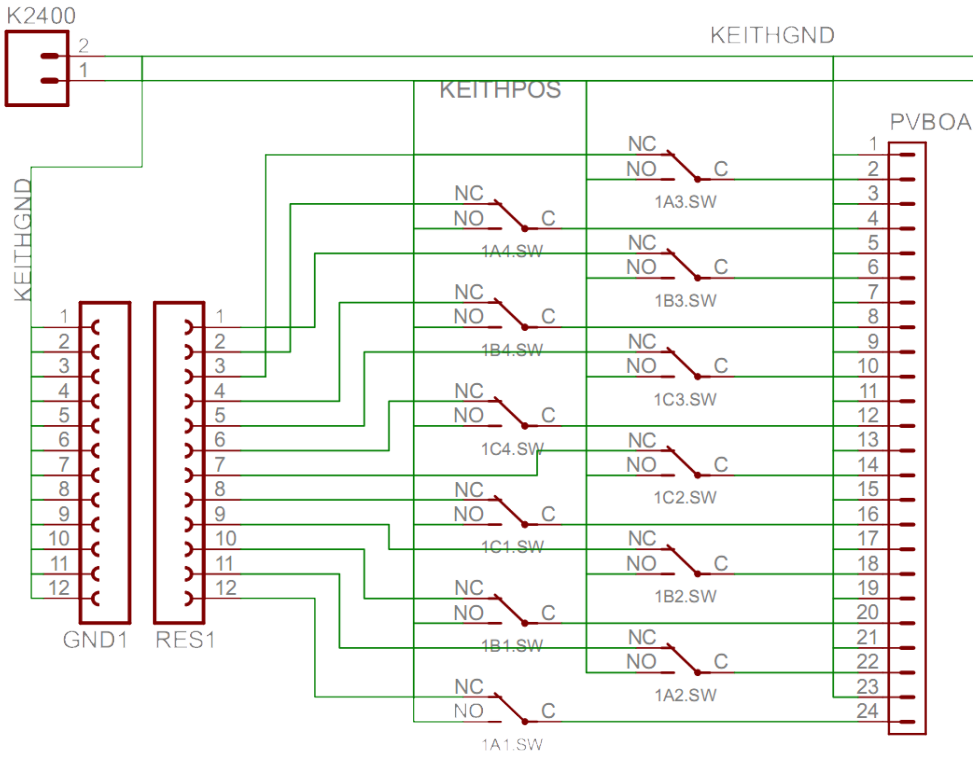

(a)

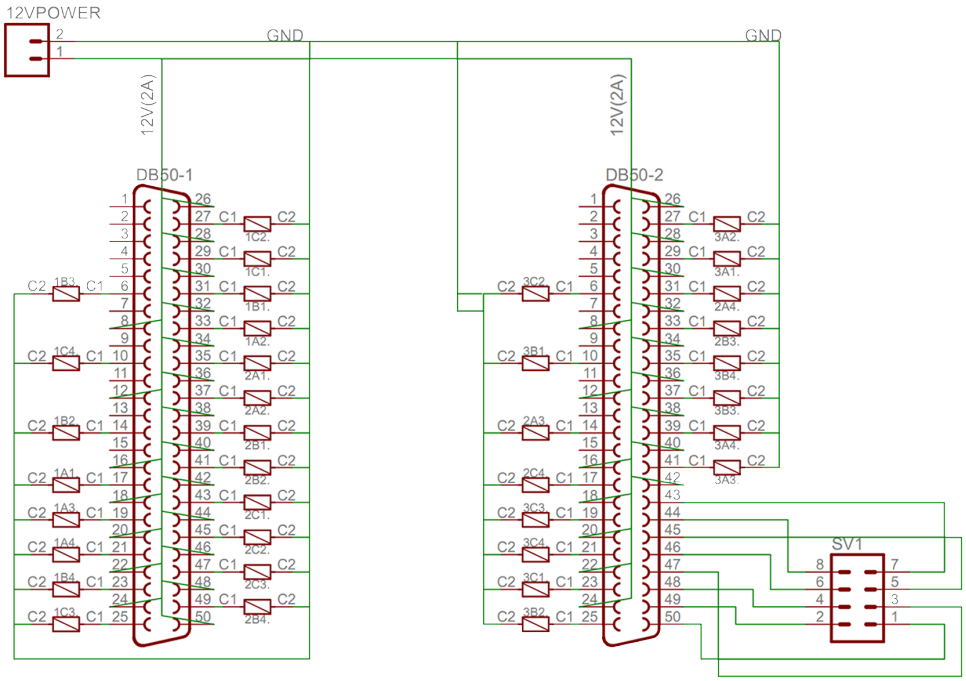

(b)

Figure 5.2: Circuit layout of the main switching board. (a) Relay contacts switching the device contacts (24-pin header) between the measurement condition (sourcemeter) and idle condition (two 12-pin header resistor banks). (b) Relay windings controlled by the datalogger (DB-50 connectors).

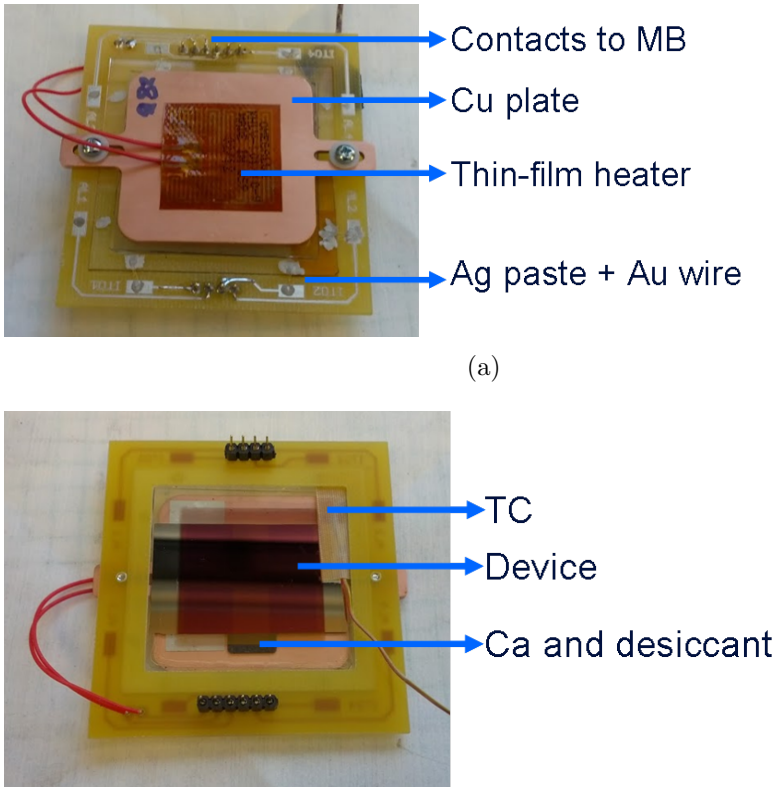

Figure 5.3: The completed carrier board layout demonstrating device mounting with temperature control. (a) Back side of the carrier board showing the contacts to the motherboard, thin-film Kapton heater, copper plate, and Ag paste and Au wire connection between device and board. (b) Front side of the board showing the device area, thermal couple, and thin-film desiccant and Ca in the encapsulation.

5.3 Temperature control

Aging devices under elevated temperature allows for accelerated lifetime testing as well as measuring the activation energy associated with the degradation mechanisms. In our test setup, each substrate is connected to an individual thin-film Kapton heater. A copper plate is inserted between the heater and the cover glass for more uniform heating. A K-type thermal couple is adhered to the device on the substrate side. All the heaters and thermal couples are conected to an Omega CN616 temperature controller, a power supply and custom-built relay control board. Figure 5.3 shows a

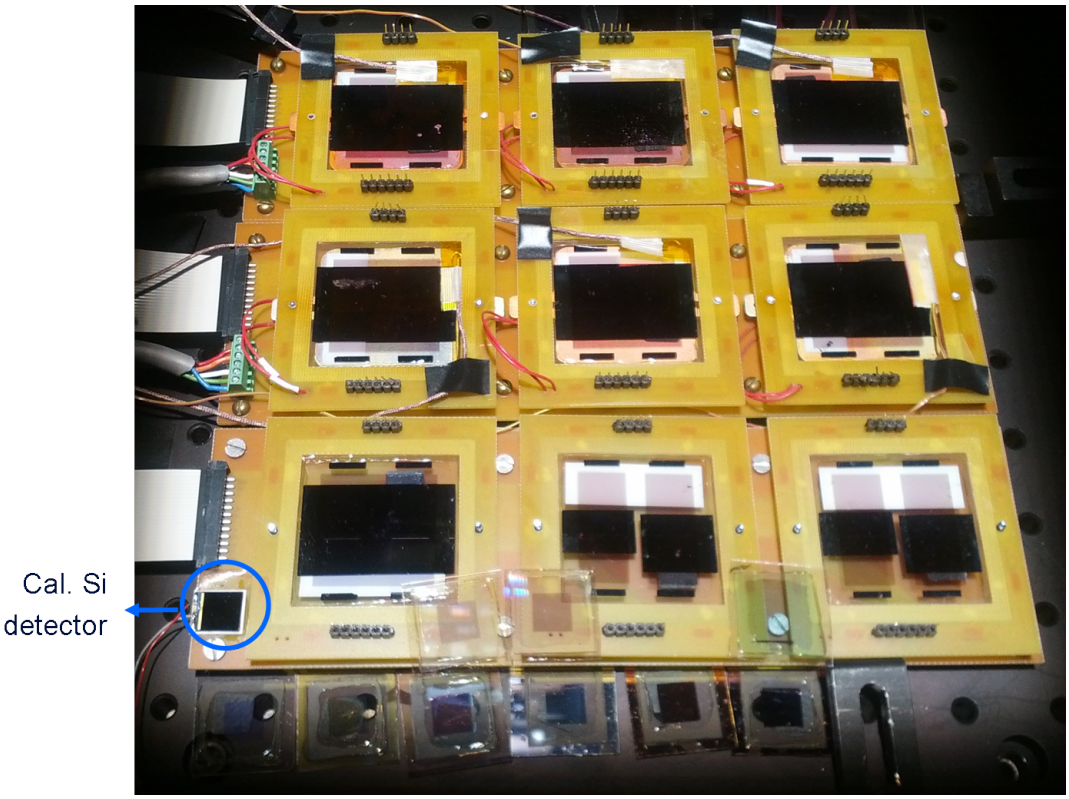

Figure 5.4: The lifetime testing system operating in full capacity. The bottom two substrates have 4 devices of different device area, while the other 7 substrates have four 1 cm^2 devices.

completed device on carrier board ready for testing.

The testing system has a total capacity of nine substrates, thirty-six 1 cm^2 devices with individual substrate temperature control. By employing custom circuit boards, all the electrical connections are pre-defined, allowing for consistent lifetime measurement with convenient device mounting. A picture of the system testing in full capacity is shown in Fig. 5.4.

CHAPTER VI

Intrinsic limits to small-molecule organic photovoltaic cell operational lifetimes

Practical and economical solar module installations require operational lifetimes of 15 years or more.[153] An overview of the state-of-art in OPV reliability research is provided in Chapter 1. Previous studies have suggested that photo-induced chemical degradation of the molecules comprising the OPV active region is the primary source of long-term deterioration in device performance. Hence, the devices are found to be stable when stored in the dark, whether or not they are connected to an electrical load.[120] In polymer OPVs, the degradation has been attributed to photo-oxidation leading to the formation of defects in the active layer,[120, 154, 155, 156, 157] buffer layer [158] and at interfaces.[159, 122, 160] The defect trap states cause nonradiative recombination, reduce carrier mobility, or result in build-up of space charge in the device active region. In small-molecule organic solar cells, studies have shown that degradation can be caused by oxygen-induced exciton quenching in C_{60},[124] degradation of the exciton blocking layer,[161] and a reduction in the ITO work function due to irradiation by UV light.[138] While there have been several previous studies of aging phenomena in a variety of OPVs, to our knowledge none have applied physics-based models that can quantitatively and accurately model the observed degradation processes.

In this chapter, we develop a systematic, analytical model to describe the early aging (i.e. the "burn-in") of SubPc donor/fullerene acceptor OPVs in the absence

of water and oxygen. We find that the photo-induced degradation is due to reduction of exciton lifetime at exciton-induced defects in the photoactive layers, either through quenching of the excitons or generation of new species with shorter exciton lifetime. The model accurately predicts the time dependence of the efficiency during the burn-in period. The defect formation can be decelerated by reducing the exciton density; therefore, mixed donor/acceptor OPV devices and materials systems [162] are more stable than their planar analogues. Furthermore, devices employing a C_{70} acceptor exhibit improved stability compared to those with C_{60}, suggesting mixed donor/acceptor (D/A) devices employing C_{70} can be used in OPVs with extended long-term performance.

6.1 Degradation mechanism

Upon illumination of the OPV, excitons are formed and subsequently diffuse to a nearby D/A interface where they dissociate into free charges. The steady-state exciton distribution is described by the diffusion equation:

$$\frac{\partial N_X(x,\lambda)}{\partial t} = D\frac{\partial^2 N_X(x,\lambda)}{\partial x^2} - k_0 N_X(x,\lambda) + G(x,\lambda) = 0 \tag{6.1}$$

Here, exciton density ($N_X(x,\lambda)$) is the exciton density generated by absorption of photons of wavelength, wavelength (λ), and at position, x. Also, D is the exciton diffusivity, exciton natural decay rate (k_0) is the exciton natural decay rate in the as-grown film including the natural (τ_0) and nonradiative (τ_{nr}) decay lifetimes (i.e.,$k_0 = 1/\tau_0 + 1/\tau_{nr}$), and $G(x,\lambda)$ is the photogeneration rate of excitons in the device active layers determined by the local intensity of the optical electric field.[15] Details regarding the optical modeling of layered structure and exciton diffusion process can be found in Appendix B.

The energetically photoexcited states can induce chemical reactions and create

dissociative defect states on the molecular sites on which they occur. Previously, it has been shown for OLEDs that such defects can be formed due to excess energy released from polarons in an Auger process, or from exciton localization, exciton-exciton annihilation, and exciton-polaron annihilation, depending on the nature of the reaction.[163] Materials absorbing photons whose energies are well in excess of their energy gaps are the most vulnerable to degradation by these mechanisms. If the resulting defects behave as deep *charge* recombination centers, they can reduce the efficiency of photogenerated charge collection. The loss in EQE, in this case, is expected to be uniform across the entire spectral range where the affected material normally absorbs. On the other hand, when defects act as nonradiative *exciton* recombination centers, the exciton diffusion process is directly affected, and the changes in EQE over time will exhibit a wavelength dependence. Here the defect states are assumed to be of the latter species, and formed by exciton localization in accordance with experimental observations in Sec. 6.3. The proposed mechanism during burn-in differs from that leading to the long-term aging of OLEDs where exciton-polaron annihilation is the dominant mechanism,[163] possibly due to the relatively high charge mobility typical of efficient OPV devices, where the polaron density is expected to be low.

The decay pathways introduced by defect states ultimately reduce the exciton lifetime through increased recombination. Consequently, Eq. 6.1 is modified to account for trap generation and sebsequent recombination, viz.:

$$\begin{aligned}\frac{\partial N_X(x,\lambda)}{\partial t} &= D\frac{\partial^2 N_X(x,\lambda)}{\partial x^2} - k' N_X(x,\lambda) + G'(x,\lambda) \\ &= D\frac{\partial^2 N_X}{\partial x^2} - N_X(k_0 + k_{XT}N_T + k_F) + G'\left(1 - \frac{N_T}{N_M}\right) \\ &= 0 \end{aligned} \tag{6.2}$$

Here the increased decay rate, k', includes: (i) exciton quenching at traps (at

rate $k_{XT}N_T$, where k_{XT} is the bimolecular reaction rate and N_T is the trap density; and (ii) exciton loss due to defect creation expressed by k_F, the trap formation rate. Furthermore, N_M is the molecular density in the layer, $G'(x, \lambda)$ is the generation rate including the change in optical constants due to both morphological and chemical changes in the film over time, and $(1 - N_T/N_M)$ accounts for the loss of photoactive molecular sites to defect formation. That is, it is assumed that the exciton generation rate decreases with time as an increasing number of degraded molecules no longer contribute free excitons. It has been shown that the exciton diffusivity does not depend strongly on defect density,[23] therefore exciton diffusivity (D) is approximated as a constant.

The capture of excitons by traps involves a two-stage approach-collision process.[25] In a material where the exciton diffusion length is much larger than the collision radius, the bimolecular quenching rate is expressed as:[25]

$$k_{XT} = 8\pi D R_C \tag{6.3}$$

where R_C is the trap capture radius for excitons.

Excitons form trap states through dissociative reactions on the excited molecules. The traps quench subsequent excitons that diffuse to within the trap capture radius, R. Hence, trap formation, exciton quenching at traps, exciton natural decay and exciton diffusion to a D/A interface are four principle competing processes, only the last of which generates charge. When the trap density is sufficiently high, trap-induced quenching becomes dominant, resulting in a significant loss in photocurrent.

When a molecule absorbs a photon, the generated exciton rapidly relaxes (over time scales of fs to ps), and reaches the lowest excited state before trap formation can occur on a time scale of $1/k_F \sim$ 10-100s. In this case the trap formation statistics are independent of wavelength. Therefore, the trap formation rate after the aging time,

t_a, at position, x, is proportional to the total exciton density N_{X-tot}:

$$\frac{\partial N_T(x,t_a)}{\partial t_a} = k_F N_{X-tot} = k_F \int_{\lambda_1}^{\lambda_2} N_X(x,\lambda,t_a)d\lambda \tag{6.4}$$

Here $[\lambda_1, \lambda_2]$ is the spectral range of absorption of the material.

Now, $N_X(x,\lambda)$ obtained from Eq. 6.2 implies that the exciton population is in steady-state, which is valid for time scales relevant to energy transfer and exciton transport (ps to μs), but not to that of degradation, aging time (t_a) (minutes to years). During the aging process, the excitons are more likely to be quenched before they can form traps. That is, the formation rate decreases with an increasing trap population. Here we assume the simple case where the formation rate decreases linearly with trap density. Then:

$$\frac{\partial N_T(x,t_a)}{\partial t_a} = k_F \left(1 - \frac{N_T}{N_{T\infty}}\right) \int_{\lambda_1}^{\lambda_2} N_X(x,\lambda,t_a)d\lambda \tag{6.5}$$

Here $N_{T\infty}$ is the saturation trap density. At saturation, the total trap density is sufficiently large that excitons are trapped at a defect, or diffuse to a D/A interface before they have an opportunity to form an additional trap on an otherwise undamaged molecule.

The progression of change in exciton density is found from the solution to Eq. 6.2 using Eq. 6.5. The EQE can be determined by the dissociated exciton flux at the D/A interface normalized to the incident photon flux, viz.:

$$EQE(\lambda) = D\frac{\partial N_X(x,\lambda)}{\partial x}\Big|_{D/A} \Big/ \frac{1}{2}\frac{c\epsilon_r\epsilon_0|E|^2}{hc/\lambda} \tag{6.6}$$

We assume that both the charge transfer and charge collection processes achieve unity efficiency in an optimized device. Details on high-performance implementation

Table 6.1: Parameters and values used to simulate the degradation of an archetype SubPc/C_{60} planar heterojunction organic photovoltaic cell.

Parameter	Unit	Material	Value	Ref.
k_F	s^{-1}	C_{60}	$6.5 \pm 0.1 \times 10^{-3}$	[121]
$N_{T\infty}$	cm^{-3}	C_{60}	$1.2 \pm 0.4 \times 10^{17}$	[121]
k_0	s^{-1}	C_{60}	1×10^{6}	[164]
		SubPc	5×10^{8}	[9]
D	cm^2/s	C_{60}	1.6×10^{-5}	[15]
		SubPc	3.2×10^{-4}	[14]
R	nm	C_{60}	1	[165]
		SubPc	2	[166]
k_{XT}	cm^3/s	C_{60}	4.0×10^{-11}	[121]
		SubPc	1.6×10^{-9}	[121]

of solving the differential equations is provided in Appendix B.2.

In Fig. 6.1 we show the simulated change in the time dependence of total exciton density (N_{X-tot}) and trap density (N_T) 6.1(a), as well as EQE (Fig. 6.1(b)) as a planar SubPc/C_{60} OPV device is aged (see Table 6.1). Under illumination, excitons are generated in the active materials following the optical field distribution. The excitons generated remotely from the D/A interface have a greater opportunity to form defects before they rapidly decay via dissociation or other mechanisms. Once trap states are formed, they quench subsequently generated excitons, thereby reducing their lifetime and their probability of reaching a D/A interface is correspondingly reduced. Excitons generated by short-wavelength photons are located closer to the reflective electrode (away from D/A interface in a planar structure), and hence are more likely to be quenched at defects, while the distribution created by long-wavelength photons peaks at a location nearer to the D/A interface where they can immediately dissociate into free charge. Hence, in Fig. 6.1, the EQE shows a more significant decrease for wavelengths between $\lambda = 300$ nm and 500 nm than at longer wavelengths.

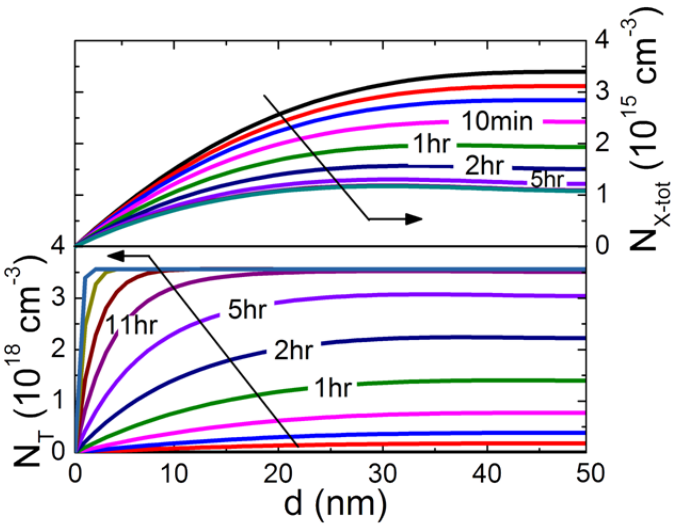

(a)

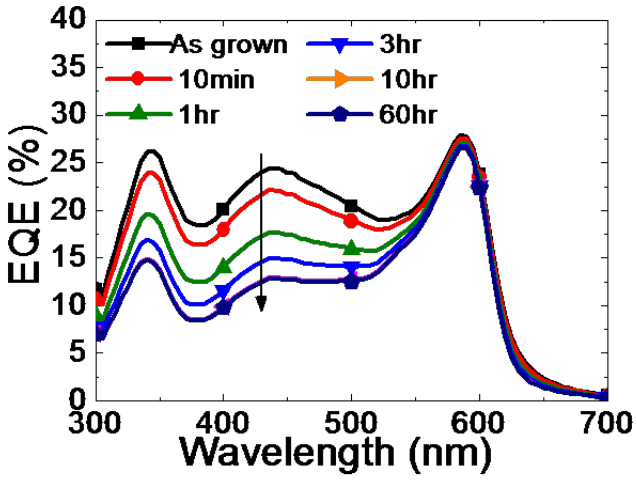

(b)

Figure 6.1: Simulated results for a planar SubPc/C_{60} OPV device. (a) The change in total exciton (N_{X-tot}) and trap (N_T) densities over aging time during burn-in. The x-axis is the position in the layer, where $x = 0$ is the location of the donor-acceptor interface. The total thickness is 50 nm. (b) Change in EQE as a function of device operating time during burn-in using the same analysis and archetype structure as in (a).

Trap-induced quenching becomes dominant when the number of defects increases and the quenching rate exciton-trap quenching rate $(k_{XT})N_T$ is comparable to the exciton natural decay rate k_0, leading to a drop in $N_X(x, \lambda)$ and thus the observed "burn-in" loss in EQE. Eventually the degradation stops when the trap density saturates at saturation trap density $(N_{T\infty})$, corresponding to the probability that an exciton is quenched by a defect or is collected before it has an opportunity to form an additional trap. The resulting EQE after the burn-in period depends on the quenching rate, k_{XT}, and the saturation trap density, which are functions of material properties (particularly the exciton natural decay lifetime and absorption spectra) and device structure.

6.2 Experimental procedure

Archetype SubPc/fullerene OPV devices were fabricated with the following structure: glass/ITO/MoO_3 10nm/active layer/PTCBI 8nm/Al 100nm. The active layer structures and thicknesses are provided in Table 6.2. Devices incorporating either a planar or mixed donor acceptor active layer with fullerene acceptors (C_{60} and C_{70}) are explored (Device P-60 corresponds to a planar SubPc/C_{60} active region, M-60 corresponds to an analogous OPV with a mixed active region, and P-70 and M-70 are similar architectures based on a C_{70} acceptor). The mixed photoactive layers have a 1:4 donor (SubPc):acceptor (fullerene) ratio, by volume.

Prior to thin-film deposition, ITO-coated glass substrates were solvent cleaned followed by CO_2 snow cleaning using procedures described previously.[167] Following UV-ozone treatment, substrates were loaded into a high-vacuum (base pressure $<4 \times 10^{-7}$ Torr) thermal evaporation chamber, where MoO_3, organic materials, and the Al cathode were deposited at a rate of 1 Å/s. The device size was defined by an array of 1 mm-diameter circular openings in a shadow mask, through which the cathode metal was deposited. All deposition rates and thicknesses were measured using a

quartz crystal thickness monitor. Thicknesses and optical constants were determined by variable-angle spectroscopic ellipsometry.

Device performance was measured with a semiconductor parameter analyzer using illumination from a source that provides 1 sun, AM1.5G illumination. The EQE spectra were measured using a lock-in amplifier and monochromated light from a 150 W Xenon lamp chopped at $\sim$ 200 Hz. The light intensities and spectra were determined using NREL-traceable calibrated Si photodiode standard.

The devices were aged at 35 ± 5 ℃ under varied applied bias, intensity and spectral ranges of simulated AM1.5G illumination. The bias conditions were controlled either actively by a source meter, or passively by a load keeping the device at the MPP with $\pm$10% accuracy. The illumination intensity and spectral range were adjusted using neutral density filters and band pass filters, respectively. The device J-V characteristics and EQE were automatically recorded periodically under continuous illumination. Devices were kept in an ultra-high-purity N_2 (<1 ppm O_2 and H_2O) environment for all transfer and testing procedures. Ellipsometry and atomic force microscopy measurements on 50 nm thick as-grown and aged neat photoactive films on Si were obtained in air to determine absorption and morphology changes over time. The aging of the neat film was performed on samples encapsulated with cover glass and UV-cured epoxy.

6.3 Burn-in degradation of planar and mixed SubPc/fullerene photovoltaic cells

Figure 6.2 shows the normalized performance as a function of aging time for Devices P-60 and M-60 under 1 sun, AM1.5G illumination. After 10 hr of device operation, Device P-60 exhibited a 28% drop in J_{SC} from its original value of 4.4 ± 0.2 to 3.2 ± 0.1 mA/cm^2, consistent with the change in its integrated EQE over

the incident spectrum, i.e., $J_{SC} = q \int EQE(\lambda) S(\lambda) \frac{\lambda}{hc} d\lambda$, where $S(\lambda)$ is the power spectrum of the incident light, c is the speed of light in vacuum, and q is the electron charge. Following aging, FF decreased from 0.63 ± 0.01 to 0.59 ± 0.01,while V_{OC} remained constant within experimental error. Taken together, these results yield a decrease in power conversion efficiency from $PCE = 2.9 \pm 0.1\%$ to $2.1 \pm 0.1\%$. The loss in PCE saturates after 10 hr once $N_T \rightarrow N_{T\infty}$.

For Device M-60, V_{OC} decreased from 0.99 ± 0.01 V to 0.91 ± 0.01 V after 48 hr, while FF and J_{SC} remained unchanged, leading to a decrease in PCE from $2.7 \pm 0.2\%$ to $2.4 \pm 0.2\%$. Both planar and mixed devices employing C_{70} exhibited improved stability compared with analogous devices employing C_{60}, as is apparent from the detailed J-V characteristics in Fig. 6.3. Device P-70 showed only a minor change in J_{SC} after 15 hr under illumination. The decrease in PCE from 2.8 ± 0.1 % to 2.7 ± 0.1 % is due to the change in FF from $0.60 \pm 0.03\%$ to 0.57 ± 0.02 %, whereas V_{OC} was unchanged at 1.07 ± 0.01V. All device performance parameters remained unchanged to within experimental error for Device M-70 after 15 hr. A summary of device performance is provided in Table 6.2.

The origin of photocurrent decrease in Device P-60 is primarily due to the decrease in the C_{60} response to the incident illumination, indicated by the spectrally-resolved EQE in Fig. 6.4(a). After 10 hr of 1 sun, AM1.5G illumination, the maximum drop of 45% in EQE in Device P-60 occurs at a wavelength of $\lambda = 450$ nm, from $23.9 \pm 0.5\%$ to $13.2 \pm 0.5\%$. To study the influence of different aging conditions, P-60 devices with an initial EQE_0 (at $\lambda = 450$ nm) $= 23.9 \pm 0.8$ % were aged at open-circuit and under AM1.5G spectrum with intensities of 33 mW/cm^2, 60 mW/cm^2, and 100 mW/cm^2 (the last corresponding to 1 sun intensity), and at $\lambda = 450 \pm 2$ nm, and 450 ± 2 nm by using band-pass filters with a full width at half maximum of 10 ± 2 nm. Figure 6.4(b) shows the loss in EQE, i.e., $\Delta EQE = EQE_0$ (as-grown) - EQE (aged) for the device

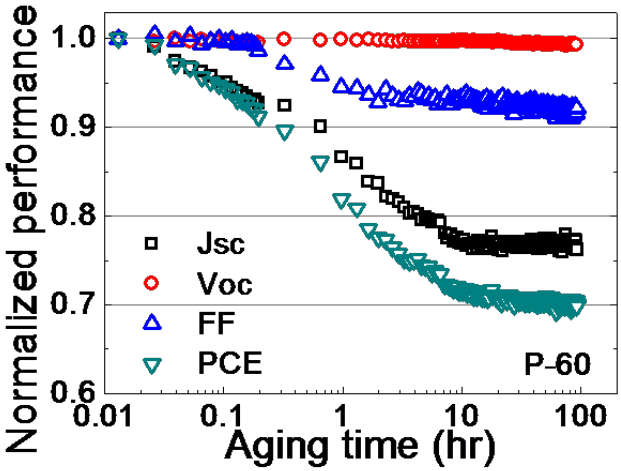

(a)

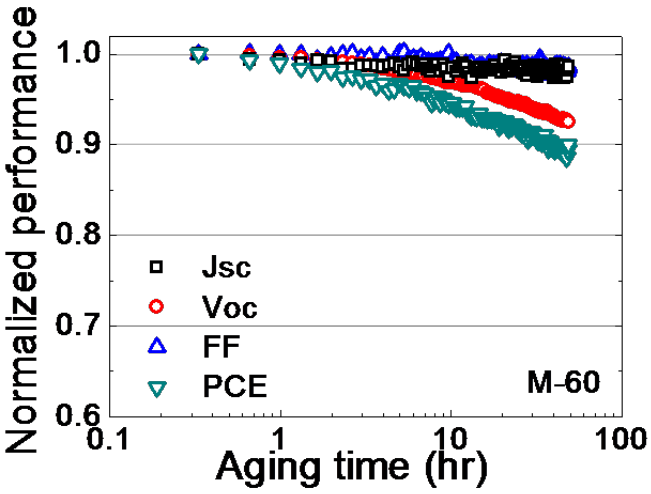

(b)

Figure 6.2: (a) Normalized planar SubPc/C_{60} (P-60) device performance characteristics vs. aging time (t_a) under 1 sun, AM1.5G illumination and at open-circuit bias: Short-circuit current (J_{SC}, squares), open-circuit voltage (V_{OC}, circles), fill factor (FF, up triangles), and power conversion efficiency (PCE, down triangles). (b) Normalized aging performance for a mixed SubPc/C_{60} (M-60) device.

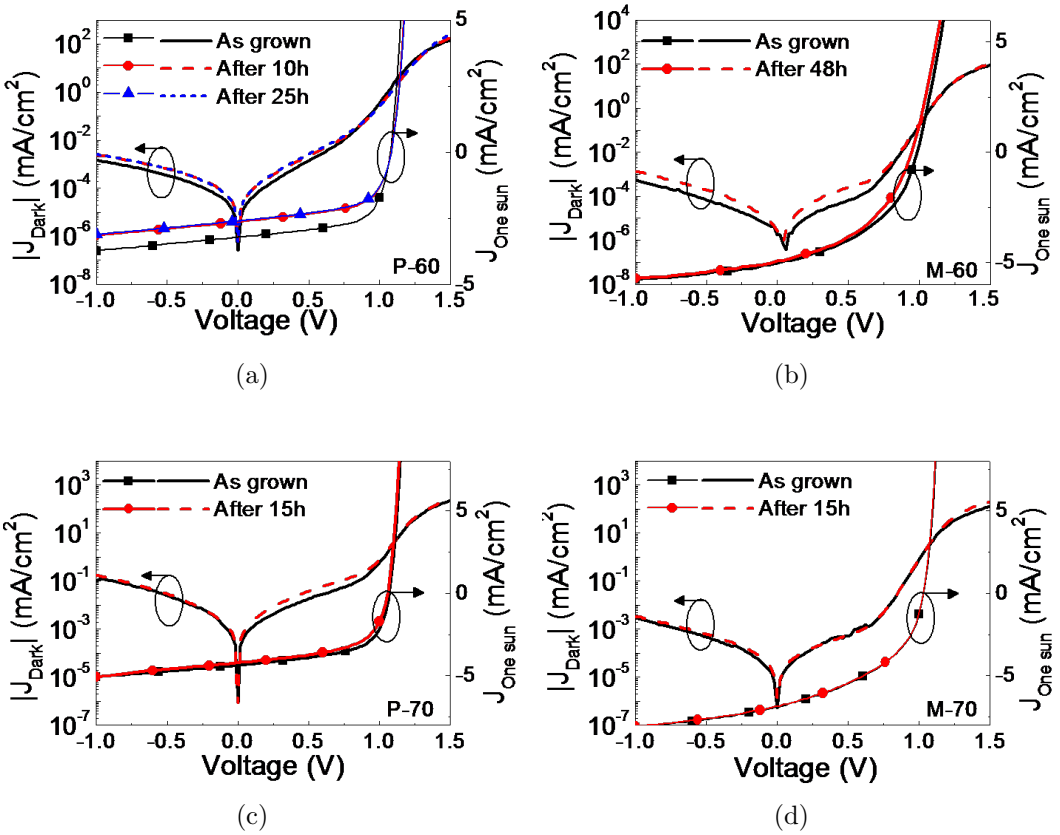

Figure 6.3: *J-V* characteristics in the dark (lines) and under 1 sun, AM1.5G illumination (symbols) for devices as grown, and after aging under simulated 1 sun, AM1.5G illumination. (a) Device P-60, (b) Device M-60, (c) Device P-70, (d) Device P-70.

Table 6.2: The performance of several archetype small molecular OPVs before and after burn-in aging at open circuit under simulated 1 sun, AM1.5G illumination

Device (active layers)	Condition	J_{SC} (mA/cm^2)	FF	V_{OC} V	PCE (%)
P-60 (SubPc 11 nm/C_{60} 50 nm)	As-grown	4.4 ± 0.2	0.63 ± 0.02	1.06 ± 0.01	2.9 ± 0.1
	Aged 10h	3.2 ± 0.1	0.59 ± 0.01	1.06 ± 0.01	2.1 ± 0.1
	Aged 25h	3.2 ± 0.1	0.59 ± 0.01	1.06 ± 0.01	2.1 ± 0.1
M-60 (SubPc: C_{60} 55 nm)	As-grown	6.0 ± 0.03	0.45 ± 0.01	0.99 ± 0.01	2.7 ± 0.2
	Aged 48h	6.0 ± 0.03	0.44 ± 0.01	0.91 ± 0.01	2.4 ± 0.2
P-70 (SubPc 11 nm/C_{70} 30 nm)	As-grown	4.4 ± 0.02	0.60 ± 0.03	1.07 ± 0.01	2.8 ± 0.1
	Aged 15h	4.4 ± 0.02	0.57 ± 0.02	1.06 ± 0.01	2.7 ± 0.1
M-70 (SubPc: C_{70} 55 nm)	As-grown	6.9 ± 0.02	0.45 ± 0.01	1.03 ± 0.01	3.2 ± 0.1
	Aged 15h	6.9 ± 0.02	0.45 ± 0.02	1.03 ± 0.01	3.2 ± 0.1

exposed to 1 sun, which has a distinctive spectral shape independent of aging time or condition, as shown in the plot of normalized ΔEQE.

Given the particular spectral dependence, only the change in EQE at one wavelength is needed to analyze the aging behavior, the change for other wavelengths can be derived thereafter. Figure 6.5(a) shows the relationship between the EQE at $\lambda = 450$ nm and the total number of absorbed photons per unit area (N_{ph}) in the C_{60} layer, where $n_{ph} = t_a \int_0^d \int_{\lambda_1}^{\lambda_2} G(x,\lambda) d\lambda dx$, with $[\lambda_1, \lambda_2]$ equal to the absorption range of C_{60}, and $d = 50$ nm is the layer thickness. We observe that ΔEQE is only a function of N_{ph}, and is independent of incident photon energy or illumination intensity. Moreover, we do not observe any dependence on bias between 0 V and V_{OC} used during aging. In Fig. 6.5(b) we show the normalized PCE as a function of time for 4 P-60 devices aged under MPP set with a passive load and open-circuit condition at 1 sun intensity. Note that there is no difference in aging when biased between open circuit (in the absence of current) and at MPP, where the power output is at maximum. From this it can be concluded that trap formation is due only to the

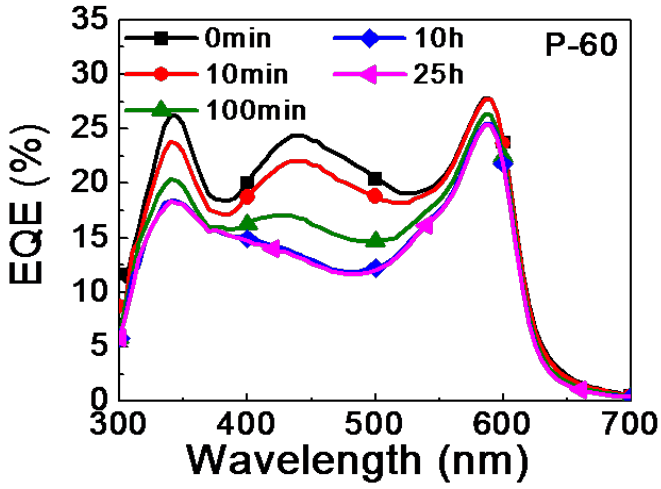

(a)

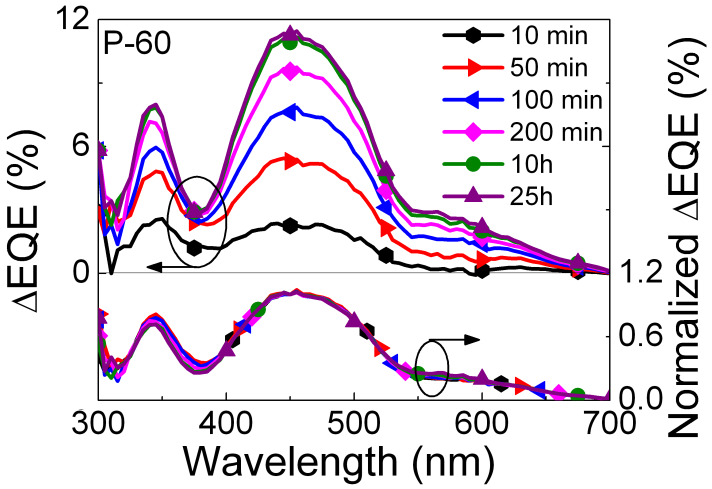

(b)

Figure 6.4: (a) EQE of Device P-60 before and after aging under simulated 1 sun, AM1.5G illumination. (b) Left axis: Evolution of the change in EQE (ΔEQE) from its value for an as-grown device for Device P-60 at different aging times under 1 sun, AM1.5G illumination. Right axis: Normalized difference in EQE from $t = 0$ to t_a, ΔEQE, after aging from $t_a = 1$ to 25 hours. Note that all exciton peaks corresponding to C_{60} absorption (at wavelengths less than 500 nm) decrease uniformly with time, whereas there is little change in the spectrum at longer wavelengths characteristic of absorption in SubPc.

localization of excitons without any interactions with charge, and the formation rate is proportional to the exciton density, as in Eq. 6.5.

The model described in Sec. 6.1 has been used to fit the decrease in EQE at $\lambda = 450$ nm of Device P-60, as indicated by the solid line in Fig. 6.6(a), with the fitting parameters that were used provided in Table 6.1. The theory predicts a saturation in device degradation at the end of the burn-in process after an extreme decrease in EQE of nearly 50% in this case. Following an initial steep efficiency decrease with time, the efficiency exhibits a second, slower and approximately long-term decrease arising from mechanisms such as multiple exciton annihilation and exciton-polaron effects not considered here.[163] The lifetime of the device to 80% of its original power conversion efficiency is 289 days (Fig. 6.6(b)), assuming an exposure of the cell to an equivalent of 5 hours of AM1.5G per day.

From the fits to the SubPc/C_{60} aging data in Fig. 6.6(a), the saturation trap density can be obtained, $N_{T\infty} = (1.2 \pm 0.4) \times 10^{17}$ cm^{-3}, or approximately 0.01% of the C_{60} molecular density has been damaged during burn-in. This density accounts for almost 30% loss in photocurrent. The total number of trap states is 6×10^{11} cm^{-2} in a 50nm thick C_{60} layer, which is reached after $\sim 10^{25}$ cm^{-2} excitons have been generated in the layer, suggesting that one out of 2×10^{13} excitons results in the formation of a defect state. Furthermore, the fits to the burn-in transient imply that the trap formation rate is $k_F = (6.5 \pm 0.1) \times 10^{-3}$ s^{-1}. This is much less than the trap-induced exciton quenching rate of $k_{XT} N_T \leqslant 4.8 \times 10^6 \mathrm{s}^{-1}$, indicating that the exciton loss due to formation of traps is negligible compared to quenching of excitons in steady-state operation under standard illumination conditions. As the device ages, trap states are rapidly generated at distances greater than an exciton diffusion length (typically $\sim$10 nm) from the D/A interface, where the exciton density is high. The resulting quenching reduces the diffusion length, leading to a reduction

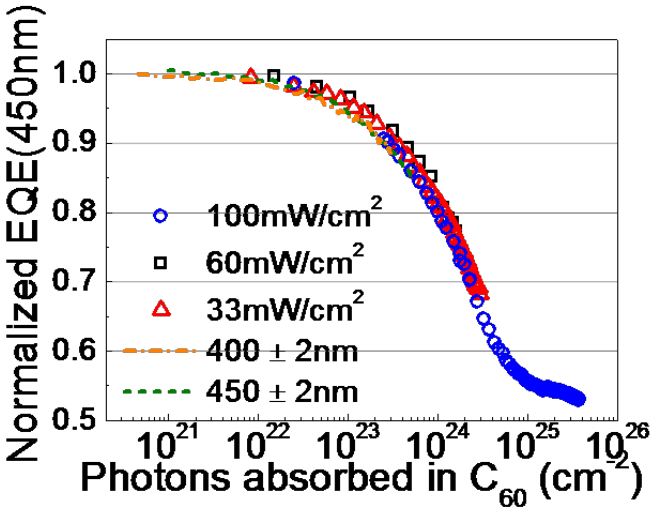

(a)

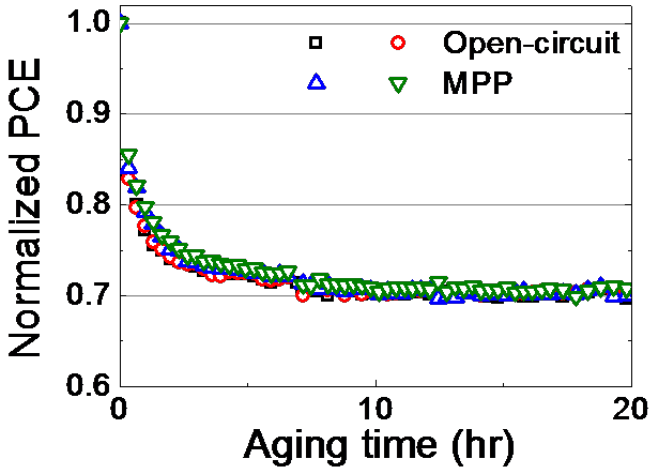

(b)

Figure 6.5: (a) Normalized EQE at a wavelength of $\lambda = 450$ nm as a function of N_{ph} absorbed in the C_{60} layer for Device P-60 EQE. Devices were aged at open-circuit bias and under AM1.5G spectrum at 100 mW/cm^2 (circles), 60mW/cm^2 (squares), 33mW/cm^2 (triangles), as well as 1 sun AM1.5G spectrum filtered by a band pass filter centered at $\lambda = 400$ nm with a spectral half width of 2 nm (dash-dotted line), and a band pass filter centered at $\lambda = 450$ nm with a spectral half width of 2 nm (short-dashed line). Note the spectral independence of the aging characteristic. (b) Normalized PCE as a function of time for four, P-60 devices aged under open-circuit bias (squares and circles), as well as at the MPP (up and down triangles).

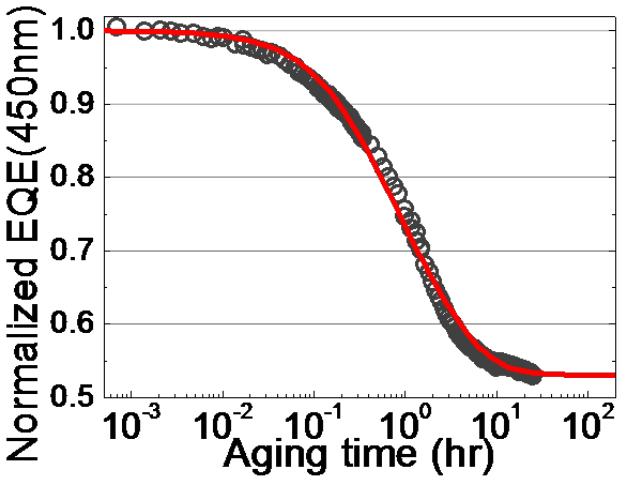

(a)

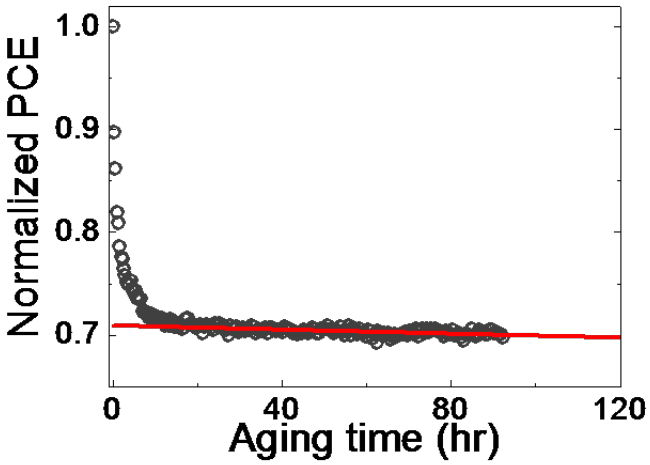

(b)

Figure 6.6: (a) Fit (line) of normalized EQE at 450 nm (data points) as a function of aging time, t_a, for Device P-60 aged under 1 sun, AM1.5G illumination to the exciton/molecular dissociation theory. (b) PCE on a linear time scale, emphasizing the change in slope of the change in efficiency with time past the burn-in duration of several hours. The straight line is a fit of normalized PCE as a function of t_a post burn-in.

in photocurrent.

Excitons in a degraded solar cell can undergo exciton diffusion, natural decay, trap-induced quenching or trap formation. Only the diffusion to a D/A interface results in photocurrent generation, while all other processes lead to loss. The efficiency of exciton diffusion to a D/A interface where dissociation into charge occurs, η_{ED}, can be expressed as the ratio:

$$\eta_{ED} = \frac{k_{Diff}(x)}{k_{Diff}(x) + k_0 + k_{XT}N_T + k_F} \tag{6.7}$$

Here the diffusion rate $k_{Diff}(x) = D\partial^2 N_X/\partial x^2$ represents the rate at which an exciton can diffuse to the interface. It depends on the location of the exciton in the layer and $k_{Diff}(x) \to \infty$ near the D/A interface.[28]

Similarly, the trap formation efficiency is:

$$\eta_{TF} = \frac{k_F}{k_{Diff}(x) + k_0 + k_{XT}N_T + k_F} \tag{6.8}$$

Therefore, as $k_{XT}N_T$ increases, the exciton diffusion efficiency is reduced. However, since the trap formation efficiency also decreases with $k_{XT}N_T$, the loss in EQE due to traps eventually reaches a steady-state value of $EQE = 13.2 \pm 0.5\%$ at a wavelength of $\lambda = 450$ nm. When a mixed donor-acceptor active layer is used, $k_{Diff}(x)$ is increased significantly, leading to an improved device lifetime, as is apparent in Fig. 6.2.

It should be noted that due to the complexity in the electronic structure of C_{60}, the reported exciton natural lifetimes range from less than 1 ns to over 1 ms. In this work, the values of $k_0 = 1$ μs and $L_D = 40$ nm are used, which agrees with the typical OPV device data. However, the actual D and exciton natural lifetime (τ_0) in our devices could be different, which will change the fitted results for k_{XT} and $N_{T\infty}$ accordingly, while the physical picture of the burn-in degradation remains the same.

6.4 Effect of exciton lifetime on burn-in degradation

Interestingly, C_{60} shows particularly pronounced burn-in degradation despite its small value of k_{XT} compared to either that of SubPc or C_{70}. Similar aging results have also been reported for planar OPVs where this phenomenon was attributed to irreversible C_{60} oxidation.[124] It is likely that the defect states in C_{60} are chemically damaged molecules. Fig. 6.7 shows the change in the optical constants for a 50 nm C_{60} neat film on Si after aging under AM1.5G. The peaks in the extinction coefficient broaden after illumination when the samples are encapsulated. The broadening is minor after 1 hr, while the same aging time causes degradation in the EQE of Device P-60 by almost 30%. Similar changes in C_{60} absorption have been reported in photopolymerized C_{60} transformed by prolonged high-intensity UV laser illumination,[168] where the chemical composition change was clear in MALDI.[169] However, the measurements reported here are conducted in a high-purity N_2 environment with < 1 ppm O_2, suggesting that oxidation may not be the primary source of degradation in this work. Moreover, based on the atomic force microscopy (AFM) images (6.8) and the apparent lack of significant changes in FF and V_{OC} over time for the P-60 devices, it is unlikely that the interfacial and bulk morphologies are significantly affected.

The difference in reliability between the species (i.e., SubPc, C_{70} and C_{60}) could be due to differences in their natural exciton lifetimes. That is, the long-lived triplet excitons ($\tau_0 = 1$ μs [164]) in C_{60} can lead to a high steady-state exciton density, thus a higher efficiency for forming dissociative traps, η_{TF}, while in materials with comparatively short exciton lifetime (e.g., C_{70},[170] SubPc,[9] or mixed D/A layers), the excitons decay before forming a defect state. This could explain why oxygen was found to have no effect on C_{60} in a mixed ZnPc:C_{60} OPV, while C_{60}-O species was diagnosed as the primary degradation mechanism in a planar ZnPc/C_{60} OPV.[146,

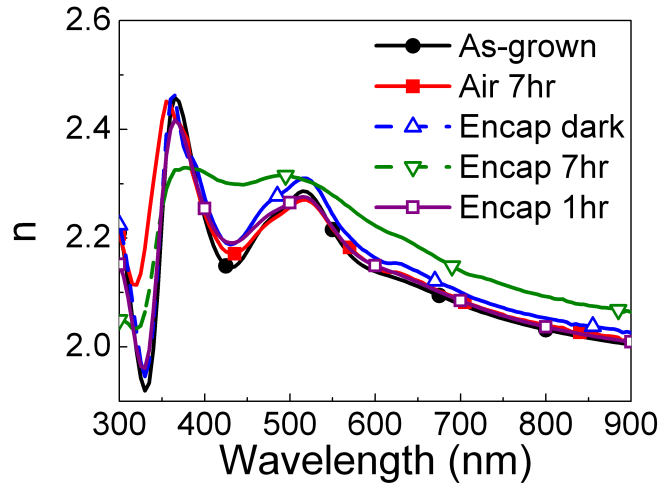

(a)

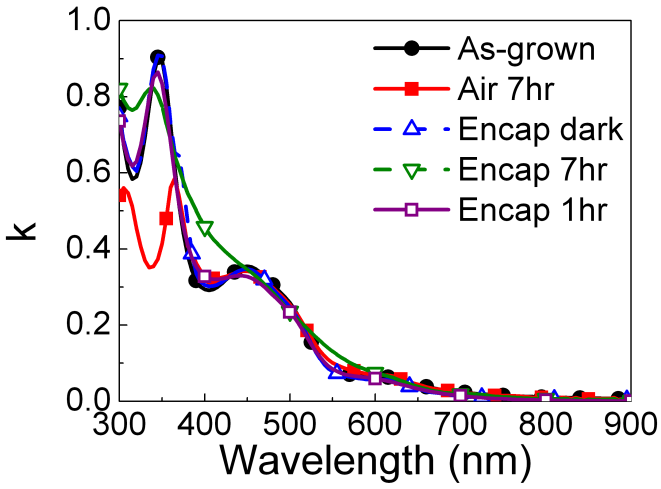

(b)

Figure 6.7: The change in the optical constants for a neat 50nm C_{60} film on Si. (a): The refractive index and (b): the extinction coefficient. The films were aged either encapsulated with quartz (open symbols), or exposed in ambient air (closed squares). The optical constants for the as-grown sample is shown for comparison (closed circles).

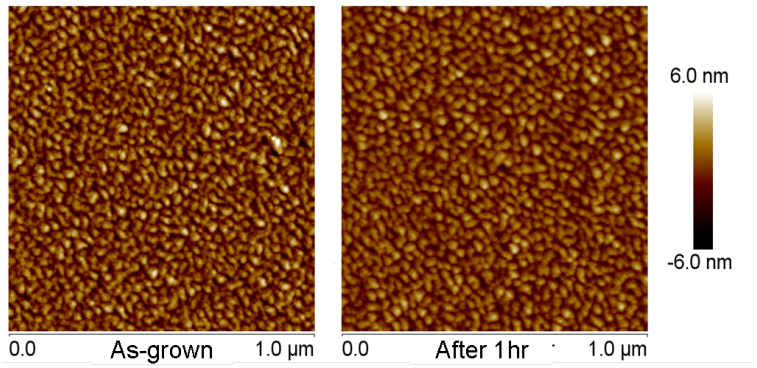

Figure 6.8: Atomic force microscope images of a 50 nm thick neat C_{60} film on Si (Left): before, and (Right): after aging under 1sun, AM1.5G illumination

124]

This dependence on k_0 is readily apparent in Fig. 6.9, where the simulated degradation behavior in devices as a function of the natural decay rate is shown. A comparison to the fit to the data for Device P-60 with $k_0 = 1\ \mu s$ is also shown. The exciton diffusion length ($L_D = \sqrt{D/k_0}$) is kept constant to maintain the same initial EQE in the original sample. All other parameters are given in Table 6.1. As k_0 increases, the trap-formation efficiency is reduced, and the trap density required to compete with natural decay is correspondingly increased. In this case, the onset ofthe burn-in is postponed, and the total drop in EQE to saturation is reduced. Note that increasing k_0 while keeping L_D constant implies that the exciton diffusivity increases accordingly, which is not achievable in a planar device. However, this is the case of incorporating a mixed D/A layer, where the effective exciton lifetime is reduced due to fast dissociation. Given the intrinsic stability of C_{70}, a mixed donor-C_{70} device could provide the most promising materials and structural routes to reliable organic solar cells.

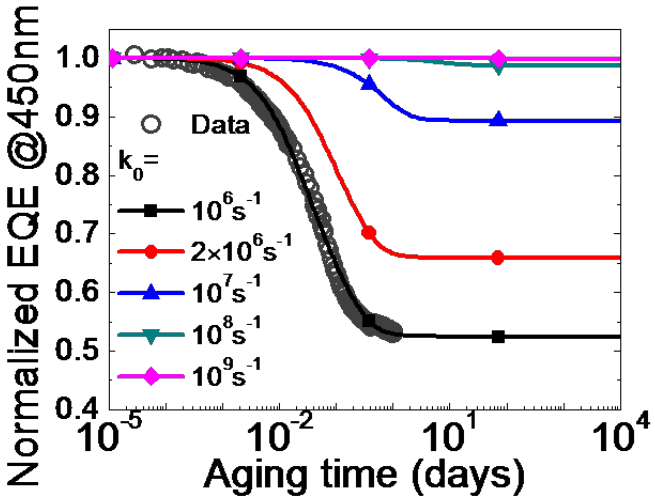

Figure 6.9: Simulated plots of the EQE at wavelength of $\lambda = 450$ nm as a function of aging time for different exciton natural decay rates, (filled symbols). The data (points) shown in Fig. 6.6(a) is reproduced for comparison to the fit at $k_0 = 1\mu$s (open circles). Parameter values other than k_0 used in the simulations are given in Table 6.1.

6.5 Burn-in degradation due to C_{60} polymerization

In Section 6.1, we developed a physical theory to accurately describe the burn-in degradation. However, the model does not provide information on the chemical nature of the trap states, and it is unclear why the trap states reach saturation before extending across the full film. In this section, we develop the theory with the hypothesis of C_{60} photopolymerization, discuss the similarity and differences to that of Section 6.1, and propose next steps necessary to confirm the chemical degradation mechanism.

In OLED lifetime studies, the degradation have been ascribed to exciton-quenching dissociative states, typically broken chemical bonds, generated through exciton-exciton or exciton-polaron annihilations.[163] As we have shown in Section 6.3, the formation of the degradation species in the burn-in period is through single exciton processes, with energy well below what is required to break C-C bonds (3.6 eV). In C_{60}, the large number of charge transfer excitons may facilitate dimerization and/or polymerization,

as illustrated in Fig. 6.10. It is known that C_{60} is susceptible to photopolymerization, potentially leading to degradation.[171, 168]

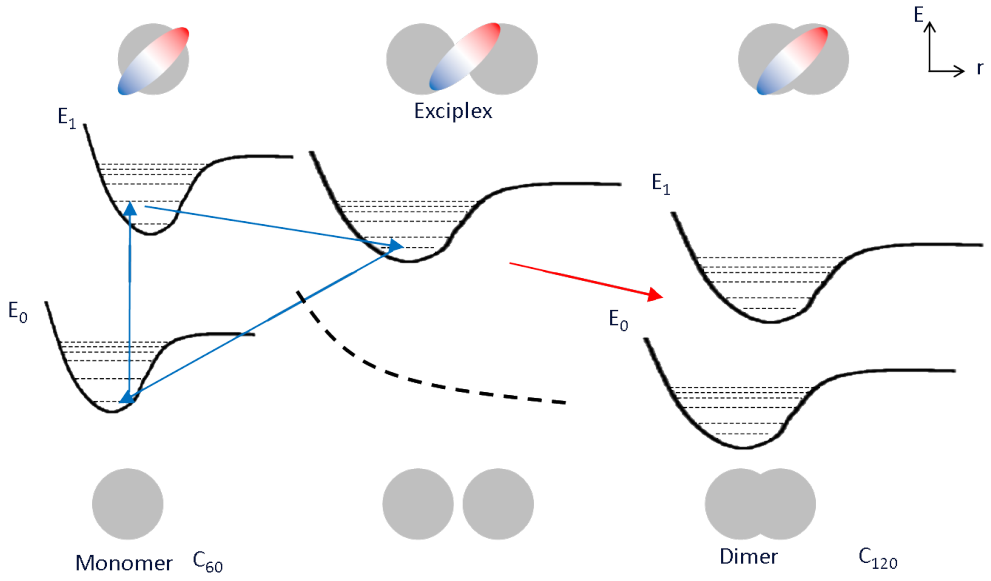

Figure 6.10: Configurational diagram of C_{60} degradation pathways

Studies have shown that the lifetime of the excited states in C_{120} is 3-10x shorter than that of C_{60}, but similar to that of C_{180}.[172, 173] There are key difference between burn-in degradation due to polymerization and the theory described in Section 6.1. In the case of photopolymerization, the exciton-induced degradation species does not quench excitons, but serve as a replacement to C_{60} molecules, with shorter excited states lifetime. As more C_{60} molecules are polymerized, on average the excited state lifetime is reduced, and fewer excitons can reach the dissociation interface, leading to the burn-in degradation. For simplicity we assume the excited state lifetime is the same for all polymer regardless of the order of polymerization, thus the exciton diffusion equation is modified as:

$$\frac{\partial N_X(x,\lambda)}{\partial t} = D\frac{\partial^2 N_X}{\partial x^2} - N_X[k_0\psi + k_{Poly}(1-\psi) + k_P] + G' = 0 \qquad (6.9)$$

Here k_{Poly} is the excited state lifetime of polymer, ψ is the fraction of monomer,

and k_P is the rate of polymerization. The change in absorption is accounted for in the generation term G'. As shown in Fig. 6.7, the change in C_{60} extinction coefficient does not change the absorption significantly, and the exciton generation rate is within 5% of the as-grown sample. The loss in monomer population is proportional to the polymerization rate, k_P, and number of remaining excited monomers, i.e.,

$$\frac{\partial N_{Monomer}(x,t_a)}{\partial t_a} = -k_P \psi N_{X-tot} = -k_P \psi \int_{\lambda_1}^{\lambda_2} N_X(x,\lambda,t_a) d\lambda \tag{6.10}$$

And by definition we have:

$$\psi = 1 + \frac{1}{N_M} \int_0^{t_a} \frac{\partial N_{Monomer}(x,t_a)}{\partial t_a} dt_a \tag{6.11}$$

Here N_M is the molecular density of C_{60}.

At the end of burn-in, the C_{60} film is fully polymerized, and the post-burn-in exciton density is determined by:

$$\frac{\partial N_X(x,\lambda)}{\partial t} = D\frac{\partial^2 N_X}{\partial x^2} - N_X k_{Poly} + G' \tag{6.12}$$

Similar to Section 6.1, degradation in EQE is calculated by solving Eq.6.9, Eq.6.10 and Eq.6.6 for the dissociated exciton flux at the D/A interface as a function of aging time. Fitting of the theory to the experimental data gives $k_{Poly} = 172 \pm 2$ ns, and $k_P = 12.5 \pm 0.5$ ms, with results shown in Fig. 6.11. The progression of EQE degradation and monomer concentration in the film are shown in Fig. 6.12. In the simulation, we assumed the extreme case where the C_{60} film is fully polymerized by the end of aging. Mathematically it is the same as if the film is partially polymerized, and the resulting exciton decay rate is the weighted average of monomer and polymer natural decay rates. The end state of the post-burn-in C_{60} film can be determined if one measures the remaining monomer concentration, or C_{60} polymer lifetime in thin

film.

The theory based on photopolymerization described in this section has a similar mathematical form as the trap-induced degradation theory discussed in Section 6.1. Both are based on exciton-induced degradation species that develop over time, and the growth rate is proportional to the exciton density in the film. In trap-induced degradation, since the quenching sites no longer contribute to exciton dissociation, a saturation trap density is arbitrarily put in the formation equation (Eq.6.5), in order to describe the post-burn-in saturation. On the other hand, the degraded species in the polymerization theory, the C_{60} polymers, have nonzero exciton lifetime, therefore saturation is reached when all C_{60} monomers are consumed. At the end of the burn-in period, the leading exciton decay rate, $k_{XT}N_{T\infty} = 210 \pm 40$ ns, is within error range of $k_{Poly} = 172 \pm 2$ ns.

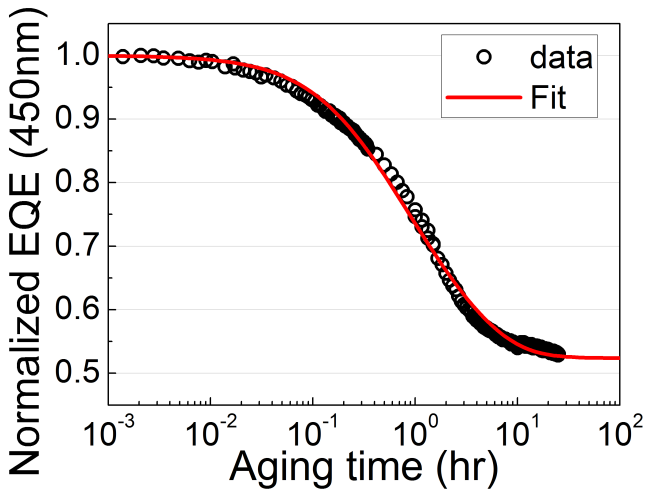

Figure 6.11: Fit (line) of normalized EQE at 450 nm (data points) as a function of aging time, t_a, for Device P-60 aged under 1 sun, AM1.5G illumination to the C_{60} polymerization theory.

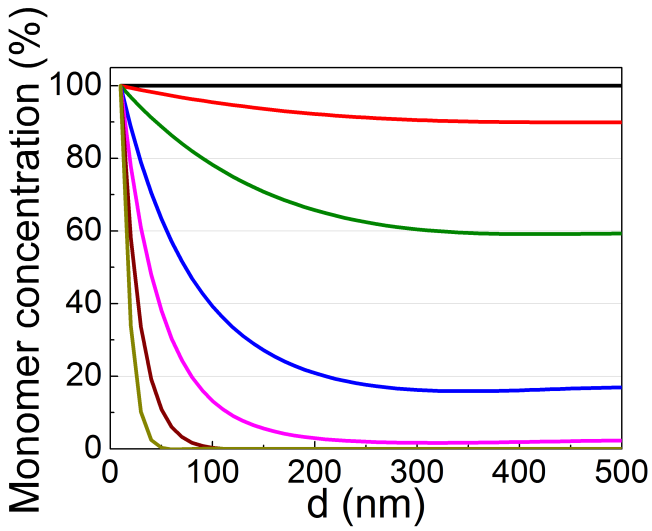

(a)

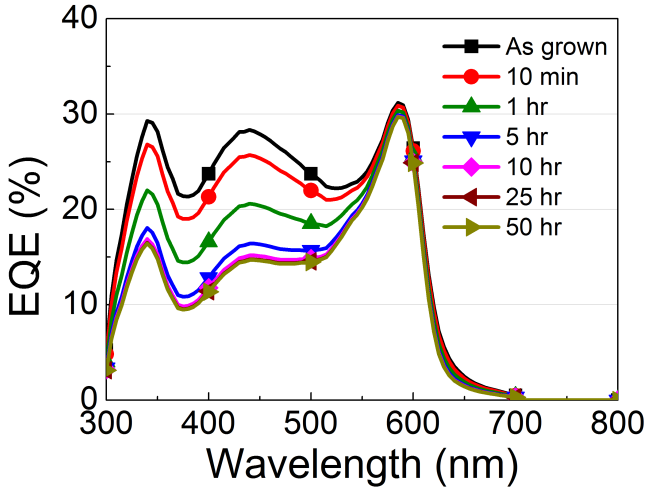

(b)

Figure 6.12: Simulated results for a planar SubPc/C_{60} OPV device assuming C_{60} polymerization. (a) The change in C_{60} monomer concentration over aging time during burn-in. The x-axis is the position in the layer, where $x = 0$ is the location of the donor-acceptor interface. The total thickness is 50 nm. (b) Change in EQE as a function of device operating time during burn-in using the same analysis and archetype structure as in (a).

In summary, quantitative models are provided which describes the physical processes resulting in a rapid fall-off in the efficiency of small molecular weight organic photovoltaic cells commencing immediately upon initial device operation. The models are based on degraded species with shortened exciton lifetime, or species that quench

subsequent excitons, and the growth rate is proportional to the exciton population in the film. In order to probe the chemical nature of the aged species, thereby identifying the degradation mechanism, accurate measurement of exciton lifetime and/or film composition at post-burn-in state is necessary. The aging of planar SubPc/C_{60} devices is accurately modeled. It was found that the operational lifetime of archetype small-molecule devices employing C_{60} can be significantly improved by employing a mixed donor-acceptor layer that reduces the natural lifetime of the C_{60} excitons, therefore inhibiting rapid generation of degraded species. Furthermore, it was found that C_{70} exhibits improved photostability compared to analogous C_{60}-based OPVs also due, in part, to the shorter exciton lifetime of the former molecule. A mixed donor/acceptor OPV using C_{70} is optimal for use in long-lifetime organic solar cells among the materials systems and device architectures explored here.

CHAPTER VII

Photodegradation of archetypal small-molecule organic semiconductors

In this chapter, we investigate the photostability of OPV active layers comprised of SubPc and fullerene thin films, aged under either AM1.5G or in the dark, and in either air or inert atmosphere. We show that the photodegradation mechanisms differ for donor and acceptor materials. However, all photodegradation can be mitigated by reducing the exciton lifetime using a donor/acceptor blend, similar to what we observed in Chapter VI. Under long-term exposure to light, we observe significant photobleaching and crystallization of SubPc. On the other hand, the photodegradation in C_{60} is led by photo-dimerization, suggested by the spectral change over time. Increasing the fraction of SubPc in SubPc:C_{60} blend leads to a decrease in the rate of photo-degradation, providing further evidence for C_{60} dimerization. Similar to the findings in Chapter VI, C_{70} is more stable than C_{60} due to its reduced tendency for photo-dimerization.

7.1 Experimental procedure

Thin films of active materials were deposited on Si or ITO-coated glass substrates that were solvent cleaned followed by CO_2 snow cleaned using procedures described previously.[167] Following UV-ozone treatment, substrates were loaded into a high-vacuum (base pressure $<4 \times 10^{-7}$ Torr) thermal evaporation chamber, where organic materials were deposited at a rate of 1 Å/s. All deposition rates and thicknesses were

measured suing a quartz crystal thickness monitor and calibrated using variable-angle spectroscopic ellipsometry.

A subset of deposited films was encapsulated in an ultra-high-purity N_2 (<1 ppm O_2 and H_2O) environment with a glass-on-glass configuration, using UV-cured epoxy as the sealant. Films were aged either in the dark, or at 35 ± 5 ℃ and under 1 sun, AM1.5G illumination. Optical intensity was calibrated using an NREL-traceable Si reference cell. Absorbane was recorded by a Lambda 1500 spectrophotometer. X-ray diffraction and atomic force microscopy measurements on as-grown and aged films were obtained in air.

7.2 Photo-degradation of active materials used in organic photovoltaic cells

The absorption spectra of SubPc (11 nm thick) samples aged in air are shown in Fig. 7.1. For the SubPc film kept in the dark, there is a moderate decrease of the peak absorption at a wavelength of $\lambda = 590$ nm after 30 hr. However, for the SubPc sample exposed to 1 sun intensity illumination, the same absorption peak disappears after 30 hour, indicating complete bleaching of SubPc film. In contrast, a SubPc:C_{60} (1:4, 55 nm thick) blend shows no degradation when kept in the dark, and the decrease in absorption for a similar sample under illumination indicates that the rate of photo-bleaching is significantly slower, with only ∼50% loss of the absorption peak at $\lambda = 590$ nm after 67 hr.

When packaged in N_2, the photo-degradation is substantially mitigated, as shown in Fig. 7.2. After 2000 hr, the reduction in SubPc film absorption is only ∼10%, considerably less than the sample exposed to air (Fig. 7.2(a)). However, after 660 hr, we observe a red shift of SubPc absorption at $\lambda = 590$ nm, while the intensity of the shoulder at $\lambda = 540$ nm increases slightly, along with a similar wavelength shift. After

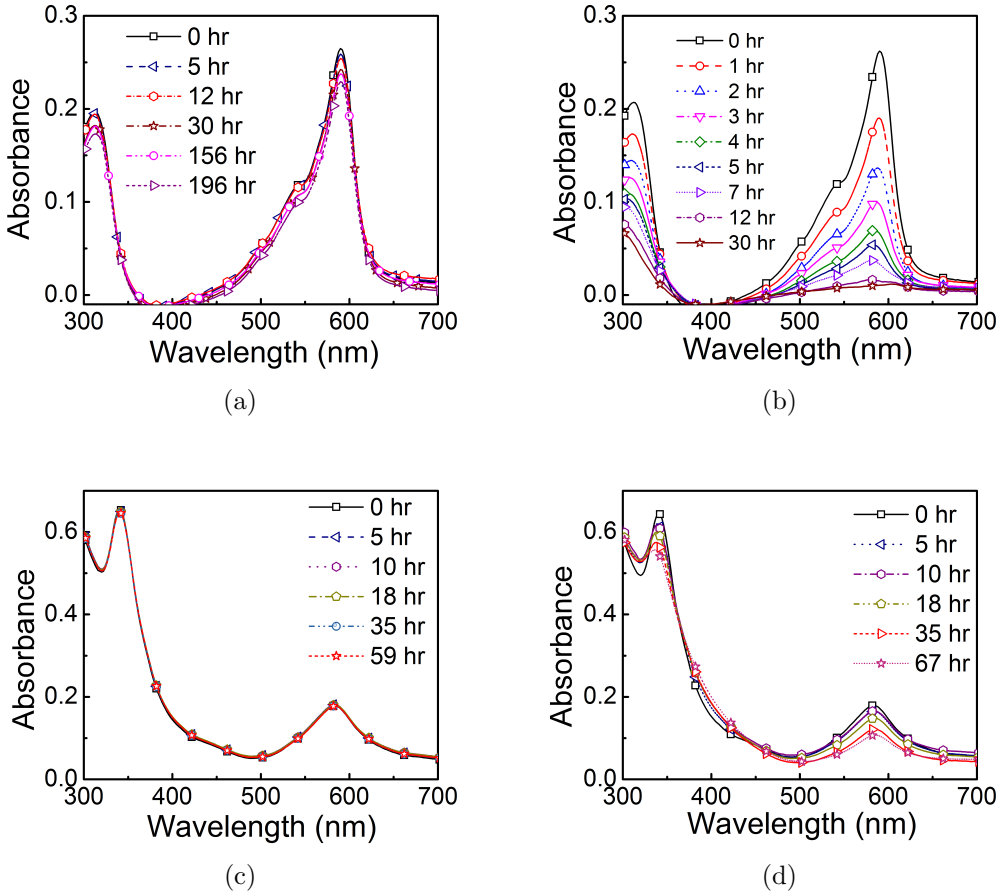

Figure 7.1: Time evolution of absorption spectra in air for (a) SubPc, kept in the dark; (b) SubPc, under 1 sun, AM1.5G illumination; (c) SubPc:C_{60} (1:4), kept in the dark; (d) SubPc:C_{60} (1:4), under 1 sun, AM1.5G illumination

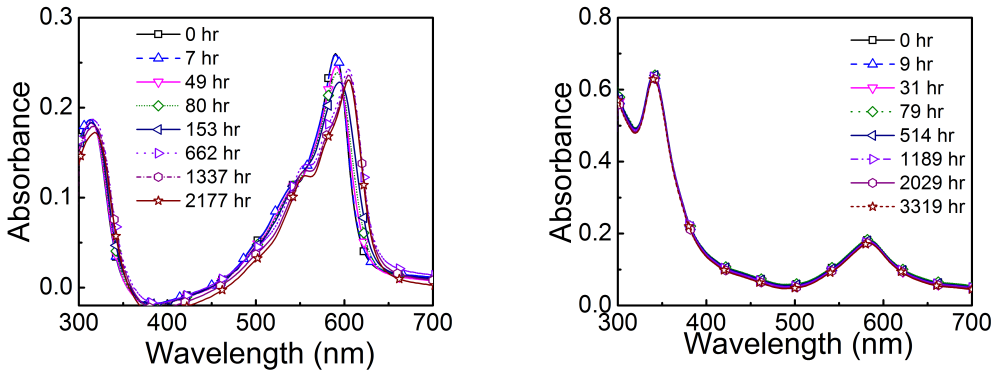

(a) (b)

Figure 7.2: Time evolution of absorption spectra for samples packaged in an ultra-high-purity N_2 environment and kept in the dark over the period tested, for (a) SubPc (arrow indicates the red shift in SubPc absorption at λ = 590 nm), and (b) SubPc:C_{60} (1:4).

mixing SubPc with C_{60} at 1:4 SubPc:C_{60} ratio, the absorption spectrum between λ = 300 nm and 700 nm is stable over 3300 hr (Fig. 7.2(b)).

The AFM images of fresh and aged SubPc films are shown in Fig. 7.3(a) and (b). The morphology of the as-grown SubPc layer in Fig. 7.3(a) indicates that the SubPc film has a root-mean-square roughness of $RMS = 1.5$ nm. On the other hand, after storing the sample in the dark for 385 hr, there is significant crystallization and a concomitant roughening to $RMS = 5.7$ nm, as shown in Fig. 7.3(b). Similar trends are observed for the SubPc film aged under 1 sun illumination. X-ray diffraction (XRD) patterns for as-deposited and aged (in the dark) SubPc films are shown in Fig. 7.3(c). The fresh SubPc film is amorphous, as indicated by the absence of a diffraction peak. Contrarily, the aged SubPc film has a peak at 20.8° that we assign to the $< 221 >$ plane, confirming crystallization over time.[174] Finally, a neat SubPc layer in a planar SubPc/C_{60} device aged at 80℃exhibits significant crystallization, leading to spherulitic growth, as shown in Fig. 7.3(d). Previously, it has been shown that spherulites cause pronounced surface roughening and the formation of current

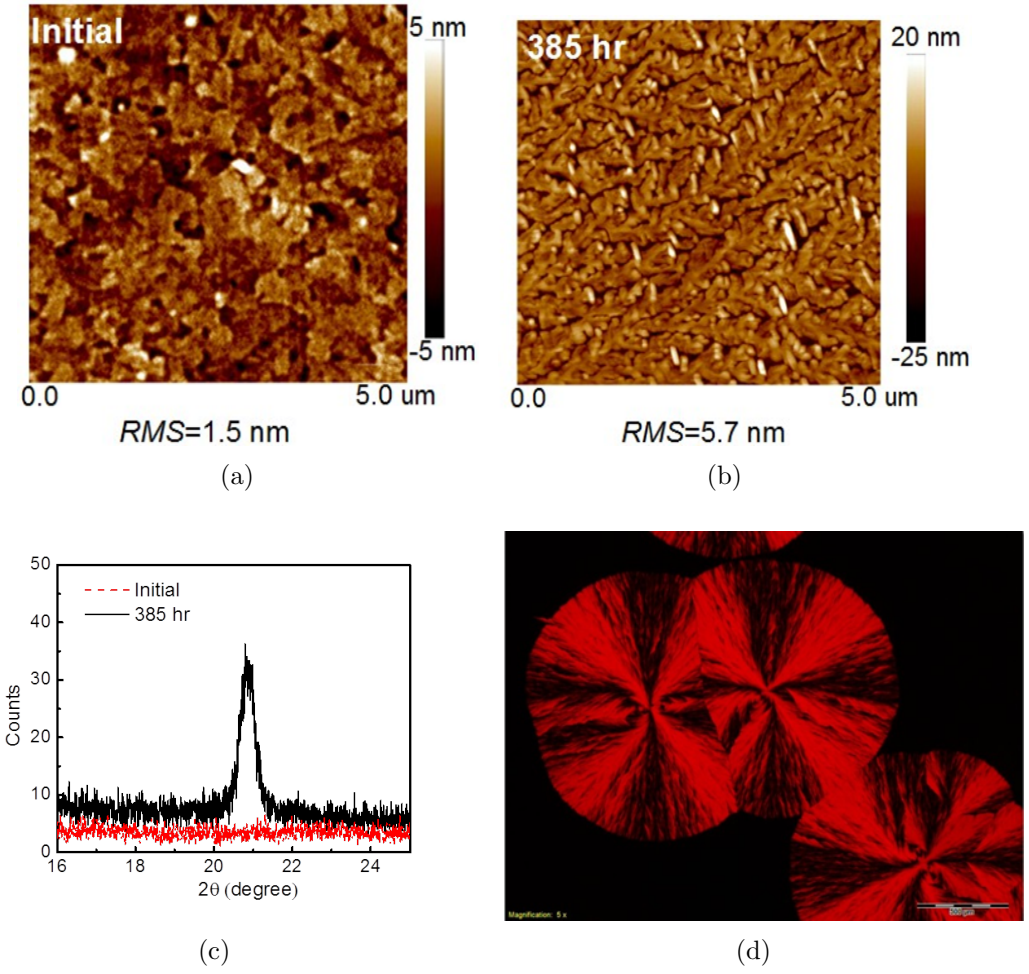

Figure 7.3: AFM images of an 11 nm thick SubPc film on Si packaged in N_2 (a) before, and (b) after storage in the dark for 385 hr, (c) X-ray diffraction of the SubPc film before and after aging, and (d) Optical microscope image of crystallinity in the packaged planar SubPc/C_{60} film aged at 80℃and under 1 sun, AM1.5G illumination for 530 hr.

shunt paths across the film. [175]

Based on the microscopy and photostability data, we conclude there is no crystallization in the mixed layers aged either in the dark or under light. On the other hand, neat SubPc undergoes substantial changes, indicating that in the absence of oxygen, C_{60} inhibits crystalline growth of SubPc.

To further investigate the stability of C_{60}, the time evolution of the absorption of packaged C_{60} (50 nm thick), SubPc:C_{60} (1:4, 55 nm thick), SubPc:C_{60} (1:1, 55 nm thick), and BPhen:C_{60} (1:4, 55 nm thick) films under 1 sun, AM1.5G illumination are shown in Fig. 7.4. The absorption spectrum between $\lambda = 400$ nm and 550 nm of a neat C_{60} film (Fig.7.4(a)) shows increased absorption centered at $\lambda = 450$ nm due to the increase in density of an intermolecular CT state, [176] accompanied by an increase of absorbance at $\lambda = 316$ nm due to a monomolecular excted state. In contrast, SubPc absorption in mixed layers remains unchanged, as shown in Fig.7.4(b) and Fig.7.4(c).

To determine the effects of SubPc on C_{60}, we measured the time evolution of the absorption of packaged SubPc:C_{60} (1:1) and BPhen:C_{60} (1:4) film, with data from the latter shown in Fig. 7.4(d). There is no significant difference in the changes for a neat C_{60} film (Fig. 7.4(a)) and Bphen:C_{60} samples, although the SubPc:C_{60} (1:1) exhibits better stability than the more dilute SubPc:C_{60} (1:4) film. The differences in the time evolutions of these various pure and mixed films is summarized in Fig. 7.5, which shows the absorption at $\lambda = 316$ nm for packaged C_{60}, SubPc:C_{60} (1:4), SubPc:C_{60} (1:1), and Bphen:C_{60} (1:4) under 1 sun illumination, normalized to the initial film optical density. We observe a rapid increase of absorbance of C_{60} during the first 7 hr, followed by a slower linear increase over the long term. On the other hand, SubPc:C_{60} (1:4) exhibits a 16% increase, and SubPc:C_{60} (1:1) showed <5% increase, while Bphen:C_{60} (1:4) has almost the same rate of increase as neat C_{60}.

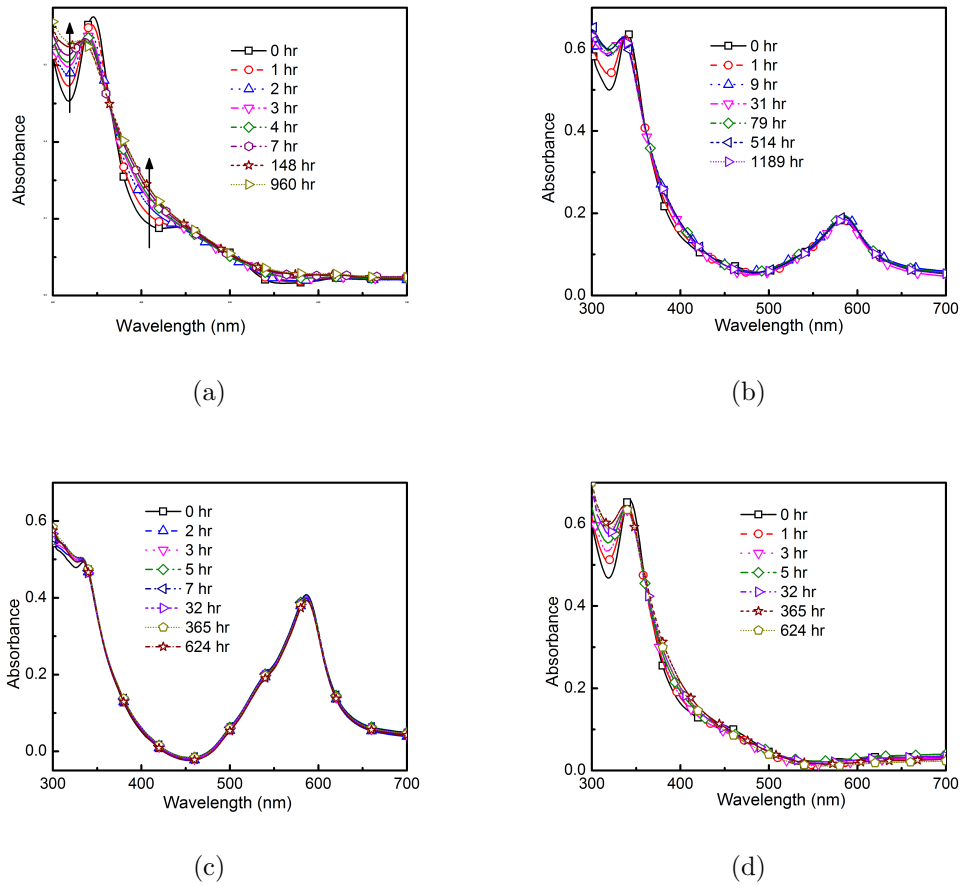

Figure 7.4: Time evolution of absorbance spectra for packaged films under 1 sun, AM1.5G illumination. (a) C_{60} (arrows indicate the increase of C_{60} absorbance), (b) SubPc:C_{60} (1:4), (c) SubPc:C_{60} (1:1), and (d) BPhen:C_{60} (1:4). There are a fast burn-in period and a slow linear degradation period for the changes in (a)

.

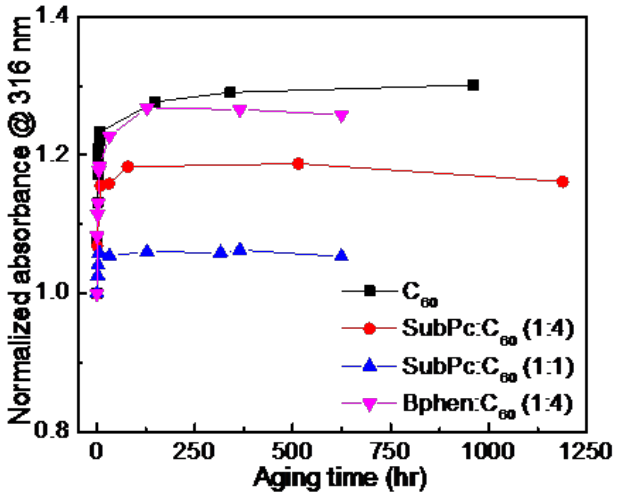

Figure 7.5: Absorption at a wavelength of λ=316 nm for packaged C_{60} (squares), SubPc:C_{60} (1:4, circles), SubPc:C_{60} (1:1, up triangles), and Bphen:C_{60} (1:4, down triangles) films under 1 sun illumination, normalized to individual film initial optical densities.

Finally, we measured the time evolution of packaged C_{70} (30 nm thick) and SubPc:C_{70} (1:4, 35 nm thick) film absorption with results given in Fig.7.6. The C_{70} film absorption is noticeably more stable than C_{60}, and indeed we observe no changes in the absorption spectra upon illumination of either film.

7.3 Degradation mechanisms

The photooxidation of SubPc requires both O_2 and excited states, as shown in Fig.7.1 and Fig.7.2. When the films are packaged in ultra-high-purity N_2, the stablility of SubPc is considerably improved due to the absence of O_2. The degradation is related to the crystallization of SubPc film, where film dichroism can affect the complex refractive index along different crystal axes, as observed in other phthalocyanine films. [177] The reorientation and change in molecular stacking lead to red shifted spectra, as observed in Fig.7.2(a).

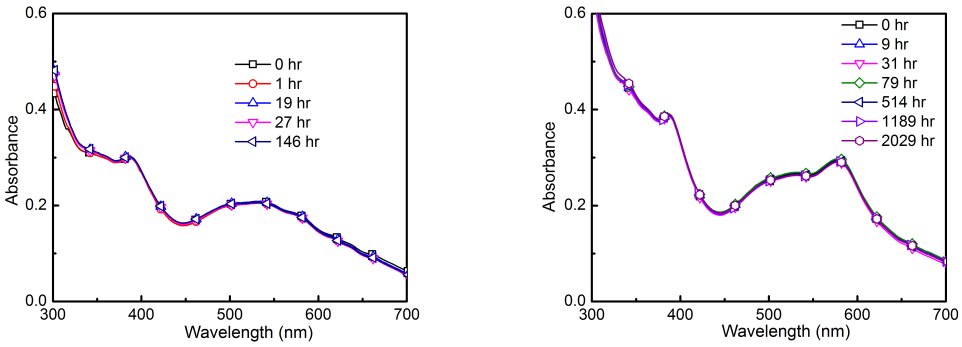

(a) (b)

Figure 7.6: Time evolution of absorbance spectra for packaged samples under 1 sun, AM1.5G illumination (a) C_{70}, (b) SubPc:C_{70} (1:4).

The degradation observed in Fig.7.4 is likely due to the photo-polymerization of C_{60}, where double bonds from two adjacent C_{60} molecules separated by less than ∼4.2 Åcan break and form a four-sided ring.[168] The dimerization reaction is endothermic, requiring the presence of light (Fig. 7.4(a)). The FTIR spectra for C_{60} films aged under different conditions is shown in Fig.7.7. Samples that were aged in the dark showed no spectral change, regardless of aging environment (air or N_2). When the film was aged under illumination and in N_2, where the photodegradation is the most pronounced as shown in Fig.7.4(a), the FTIR spectrum deteriorates, indicating chemical change in the film. On the other hand, when the C_{60} film is aged under illumination without encapsulation, there is no change in C_{60} absorption spectrum. Yet a broad absorption peak between 1730 and 1800 cm^{-1} occurs, which corresponds to C-O vibrational stretching peaks at 1798 cm^{-1} and 1752cm^{-1} in oxidized fullerence.[178] From this we conclude that photo-polymerization proceeds via the C_{60} triplet state, which is quenched by oxygen. [179]

Similar to previous discussion in Chapter VI, the reduced exciton lifetime in donor/acceptor blends removes the molecular excited state before an energy-induced defect (in this case a C_{60} dimer) can form. Therefore photo-polymerization of C_{60}

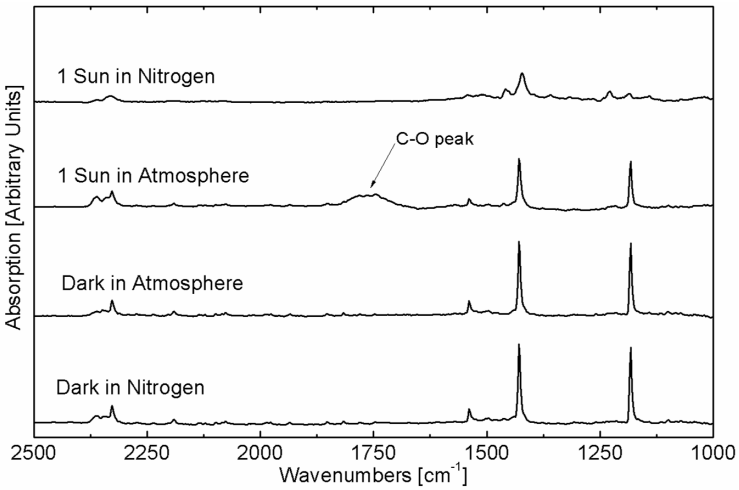

Figure 7.7: Fourier transform infrared spectra of C_{60} films on CaF_2 substrates obtained after 1 week of aging under conditions indicated. The C-O peak observed for the sample aged in air under illumination is indicated.

is significantly slower in a 1:4 blend than in neat C_{60} films, and is further mitigated when the ratio of the donor to acceptor is increased to 1:1. When C_{60} is mixed with BPhen, the excited state is localized on C_{60}, and its lifetime (and hence its ability to form traps) is unaffected by the presence of BPhen.

It has been reported that C_{70} has a considerably reduced ability to photo-polymerize than C_{70}. [168] Indeed, the stability of C_{70} after 2000hr of aging (Fig.7.6(a)) strongly supports this hypothesis. The reduced tendency to polymerization may be due to the reduced symmetry of C_{70} relative to C_{60}. There are only 10 carbon double bonds in C_{70} while there are 30 such bonds in a C_{60} molecule, leading to the reduction of the [2+2] photo-cycloaddition in C_{70}.

In summary, we present effects of aging in the presence or absence of 1 sun, AM1.5G illumination or oxygen on the aborbance and morphology changes in SubPc and fullerene films. We show that the degradation of SubPc requires oxygen and light, and can be mitigated by encapsulation or blending with acceptor materials. On the other hand, the degradation in C_{60} films shown in this chapter, as well as degradation in device performance shown in Chapter VI, are likely due to the photo-

polymerization of C_{60}. Devices and films based on C_{70} exhibit complete stability during the aging period investigated, owing to the reduced tendency of this acceptor molecule to polymerize.

CHAPTER VIII

Long-term reliability of small-molecule organic solar cells

Chapter VI discussed the mechanism leading to the initial burn-in degradation in the absence of water and oxygen. It has been found that the degradation is due to exciton-induced defect states, and the deterioration of device performance occurs on the time scale of hours. Devices exhibit improved stability post burn-in, and degradation occurs on the time scale of weeks under continuous 1 sun, AM1.5G illumination. Therefore accelerated testing is necessary to understand device degradation within a reasonable time frame. Thermal activation of device degradation is the most commonly used method, while humidity and light intensity can also serve as stress factors.[122, 137] Given that solar panels under outdoor operating conditions are at elevated temperature (40-50 ℃), it is crucial to understand device reliability at higher temperatures. By analyzing the temperature dependence of degradation rate according to the Arrhenius relationship, the activation energy of the process is calculated, providing insights into associated degradation processes. Previous studies have focused on activation energy of polymer solar cell degradation.[133, 129] In this chapter, we discuss the thermally activated degradation of small-molecule OPVs.

8.1 Experimental procedure

Thin-film OPV devices were fabricated with the following structure: glass/ITO/ MoO_3 10 nm/active layer/BPhen 8 nm/Al 100 nm. The active layer comprises either

a planar (SubPc 11 nm/C_{60} 50 nm, Device P-60) or mixed (SubPc:C_{60} 55 nm, Device M-60) SubPc-C_{60} thin film. The mixed active layers have a 1:4 SubPc to C_{60} ratio by volume. Prior to thin-film deposition, glass substrates with patterned 1 cm wide ITO stripes were solvent cleaned followed by CO_2 snow cleaning using procedures described previously.[167] Following UV-ozone treatment, substrates were loaded into a high-vacuum (base pressure $< 4 \times 10^{-7}$ Torr) thermal evaporation chamber, where MoO_3, organic materials, and the Al cathode were deposited at a rate of 1 Å/s. The Al cathode was deposited through a shadow mask defining 1 cm wide strips. The active device area of 1 cm^2 was defined by the overlap between the ITO and cathode. All deposition rates and thicknesses were measured using a quartz crystal thickness monitor and calibrated using variable-angle spectroscopic ellipsometry. After fabrication, the devices were encapsulated in a glass-on-glass configuration. Prior to encapsulation, a 0.6 cm^2, 50 nm thick Ca film was deposited onto the cover glass as a visual indicator of packaging quality.[141] Moreover, a thin-film desiccant was applied on the cover glass as a getter of residual moisture. The cover glass and substrate were then sealed using UV-cured epoxy. All transfer and encapsulation processes were done in an ultra-pure N_2 environment (< 1 ppm H_2O and O_2).

Samples of Device M60 for selected area electron diffraction (SAED) images and the TOF-SIMS measurements were prepared identically to the devices described above. For SAED images, the samples were placed in water where MoO_3 layer was dissolved and the organic film was captured by a Cu transmission electron microscope (TEM) grid with a porous carbon film. The SAED patterns were taken at 200 kV using a JEOL 2010F analytical electron microscope, with a selective aperture diameter of 100 μm. Samples for TOF-SIMS measurements were kept under N_2 for all transfer procedures. TOF-SIMS mass spectra and depth profiles of the samples were carried out using a PHI TRIFT III TOF-SIMS with a 22 keV Au^+ analytical ion beam and a 2 keV Cs^+ sputtering gun. Charging compensation was used during

the surface analyses.

To study aging as a function of temperature, 6-8 devices (2 substrates) from two growths were tested for each temperature and device structure. Device performance under continuous simulated AM1.5G illumination as a function of time and temperature was measured in the test setup described in Chapter V.

8.2 Accelerated degradation of planar SubPc/C_{60} organic photovoltaic cells

In Chapter VI, planar SubPc/C_{60} devices were stable post the burn-in period. Yet understanding the thermally-activated degradation is difficult due to the crystallization of SubPc described in Chapter VII. As-grown Device P-60 with initial performance of $R = 0.034 \pm 0.002$ A/W, $FF = 0.65 \pm 0.05$, $V_{OC} = 1.05 \pm 0.01$ V, and $PCE = 2.4 \pm 0.3\%$ were tested under simulated AM1.5G at 40, 60 and 80 ℃. Figure 8.1 shows the normalized performance of Device P-60 as a function of time. Here, half of the devices were passively set at MPP with an electrical load, while the other half were set at open-circuit condition. Once the trap formation saturates, the degradation in responsivity reaches equilibrium, and the long-term degradation is led by the decrease in FF. At high aging temperature, Device P-60 undergoes crystallization, leading to a drastic drop in FF or shorting of the devices. It results in a reduced sample size and large variation in lifetime and no Arrhenius relationship is observed in Fig. 8.2. At 40 ℃ aging temperature, T80 = 360 ± 60 days is obtained, assuming an average of 5h of AM1.5G per day. The longest device lifetime T80 = 560 ± 90 days is obtained for devices aged under 60 ℃.

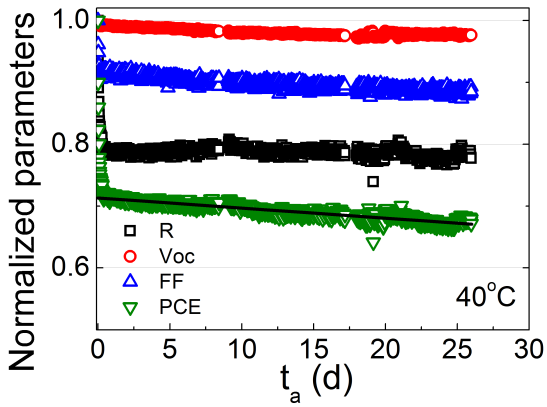

(a)

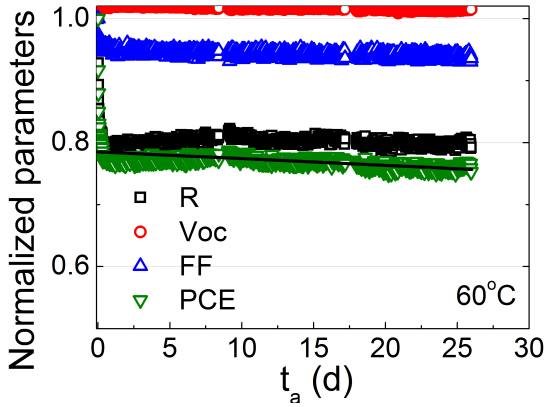

(b)

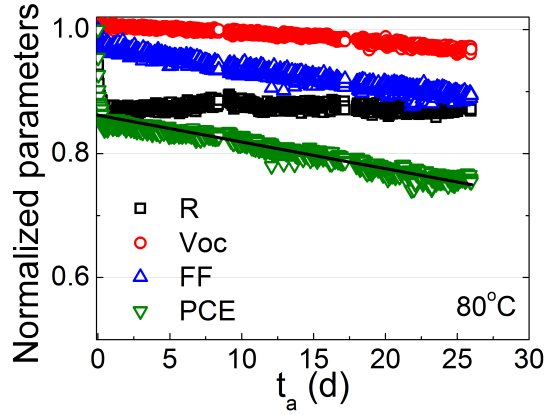

(c)

Figure 8.1: Normalized responsivity (R, squares), fill factor (FF, up triangles), open-circuit voltage (V_{OC}, circles), and power conversion efficiency (PCE, down triangles) of Device P-60 as a function of time when age dunder 1 sun, AM1.5G illumination and at 40 (a), 60 (b), and 80 (c) $\pm$ 3 ℃. Fit of PCE degradation rate according to theory described in text is shown (line).

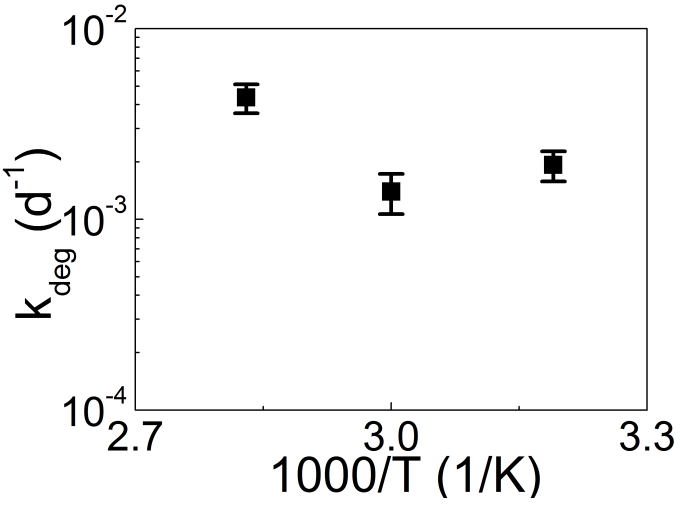

Figure 8.2: Degradation rate of PCE (k_{deg}, squares) as a function of aging temperature.

8.3 Thermally-activated degradation of mixed SubPc:C_{60} organic photovoltaic cells

The as-grown samples of Device M-60 exhibit $R = 0.068 \pm 0.002$ A/W, $FF = 0.43 \pm 0.02$, and $V_{OC} = 1.02 \pm 0.05$ V, resulting in $PCE = 3.0 \pm 0.3\%$. The error range includes measurement error and variation between devices, substrates and different growths. The responsivity of Device M-60 is stable for long periods of time, due to fast exciton dissociation inhibiting trap formation discussed in Chapter VI. As shown in Figure 8.3, when the aging temperature is between 40-80 ℃, the loss in responsivity is less than 7 % of 70 days of aging. Similarly, the FF is relatively stable for aging at 90 ℃, with less than 10 % decrease (Fig. 8.3(b)). The degradation in PCE is dominated by the decrease in V_{OC}, as shown in Fig. 8.3(c) and 8.3(d). At aging temperature >90 ℃, noticeable loss in R occurs and FF decreases more rapidly, indicating new degradation mechanism.

The post-burn-in degradation in PCE is approximated by a linear decay, viz: $PCE(t) = k_{deg}t + PCE_0$, where k_{deg} is the degradation rate, and PCE_0 is the in-

tercept corresponding to the post-burn-in PCE value. The device lifetime (T80) is taken as the time at which PCE drops to 80% of its post-burn-in value, i.e., (T80 = $0.2PCE_0/k_{deg}$). For devices aged at 40 ℃, a lifetime of T80 = 1500 ± 500 days is obtained, assuming an average of 5 hours of 1 sun, AM1.5G illumination per day. Figure 8.4 shows the degradation rate of PCE, k_{deg}, as a function of aging temperature between 40-80 ℃, where the degradation behavior is similar. The dependence of k_{deg} on aging temperature follows the Arrhenius relationship, $k_{deg} = k_{deg}(0) \exp(-E_A/k_BT)$, where E_A is the activation energy, k_B is the Boltzmann constant, T is temperature and $k_{deg}(0)$ is the pre-factor. Fitting of the data gives an activation energy $E_A = 430 \pm 60$ meV, indicating the degradation is associated with sub-bandgap processes.

To understand the degradation mechanism, the dark current density (J_{Dark}) of a series of Device M-60 before and after aging is monitored during aging, as shown in Fig. 8.5. The dark current increases when the device is heated, and continues rising as devices ages. As mentioned in Chapter 1, the OPV current-voltage is described by the ideal diode equation $J = J_{sD}[\exp(qV_a/n_Dk_BT) - k_{PPd}/k_{PPd,eq}] + J_{sA}[\exp(qV_a/n_Ak_BT) - k_{PPd}/k_{PPd,eq}] - q\eta_{PPd}J_X$. Under forward bias, k_{PPd} is similar to $k_{PPd,eq}$, therefore the ideal diode equation reduces to $J = J_{sD}[\exp(qV_a/n_Dk_BT) - 1] + J_{sA}[\exp(qV_a/n_Ak_BT) - 1] - q\eta_{PPd}J_X$, where $V_a = V - JR_{sa}$. In the aged devices, the dark current increases and the inflection point disappears. Hence only one of the two diode expressions in Giebink's double diode model has a meaningful fit. Therefore in the following analyses we only include one of the diodes. It is likely that the other diode go through similar aging processes, however due to the lack of accurate fit we do not know the exact change in the the diode parameters.

Fitting the dark current according to the ideal diode equation gives the reverse saturation current density, J_S, series resistance, R_{SA}, and ideality factor, n. For as-

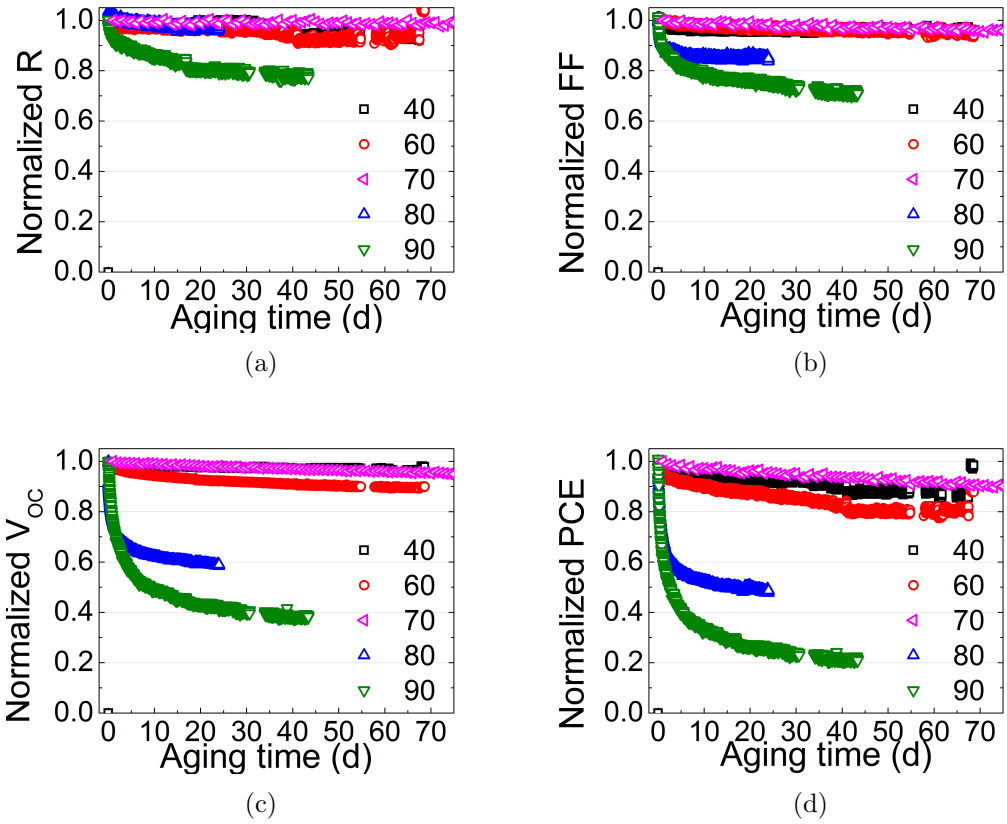

Figure 8.3: Normalized performance for Device M-60 aged under 40 ℃(squares), 60 ℃(circles), 70 ℃(left triangles), 80 ℃(up triangles) and 90 ℃(down triangles) and ac1am15g. (a) R, (b) FF, (c) V_{OC}, (d) PCE.

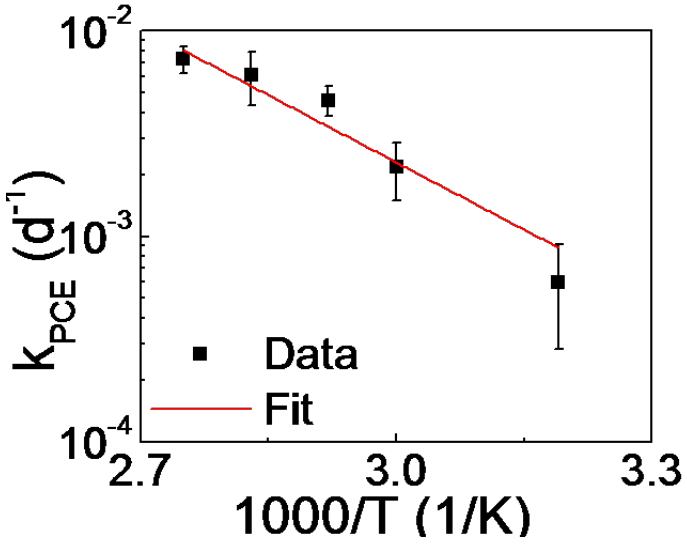

Figure 8.4: The degradation rate of PCE (k_{deg}, symbols) for Device M-60 as a function of aging temperature (T) and the fit according to the Arrhenius relationship described in text (line).

grown devices, we obtain $J_S = (3.0 \pm 0.3) \times 10^{-9}$ A/cm^2, $J_S = 3.6 \pm 0.2$, and $R_{SA} = 24 \pm 5 \Omega \cdot$cm^2. After aging under 40 ℃ for 70 days, J_S increases to $(1.1 \pm 0.2) \times 10^{-8}$ A/cm^2 and n increases to 6.6 ± 0.1 (Fig. 8.6). For device aged under 80 ℃, J_S increases to $((2.0 \pm 0.1) \times 10^{-5}$A/cm^2) and n increases to 6.6 ± 0.1. The high J_S and n indicates increased recombination in the active layer, leading to the loss in V_{OC}. Meanwhile, R_{SA} remains approximately the same for all aging temperature, suggesting no significant change has occured in contact or interface resistance.

In order to investigate the chemical nature of degradation, SAED and TOF-SIMS measurements are conducted on as-grown M-60 devices and the devices aged at 80 ℃ for 24 days, when PCE drops to 50 % of its initial value. All samples stay amorphous, as indicated by the broad diffraction rings in the SAED images shown in Fig. 8.7(a) and 8.7(b). Meanwhile, TOF-SIMS measurements suggest oxygen diffusion from the cathode into the active layer, possibly through the pinholes in the cathode layer (Fig. 8.7(c) and 8.7(d)). It is likely that oxygen has introduced sub-bandgap

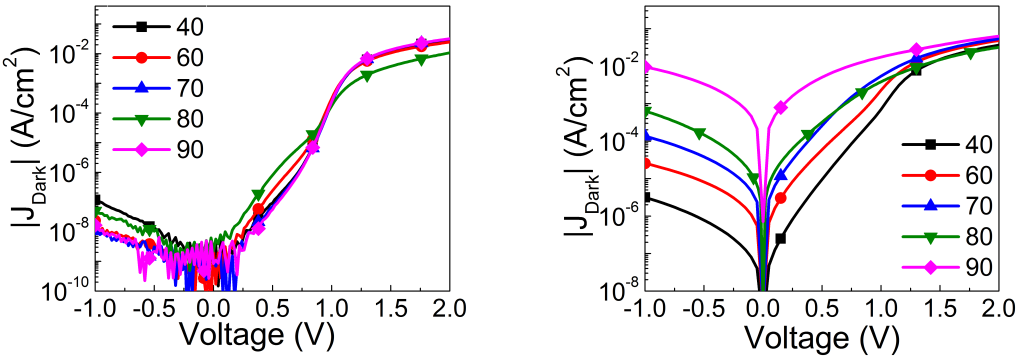

(a) (b)

Figure 8.5: Dark current density vs. voltage characteristics for Device M-60 before (a) and after (b) aging under 40 ℃ (squares), 60 ℃ (circles), 70 ℃ (up triangles), 80 ℃ (down triangles) and 90 ℃ (diamonds). The J_{Dark}-V characteristics were measured under room temperature.

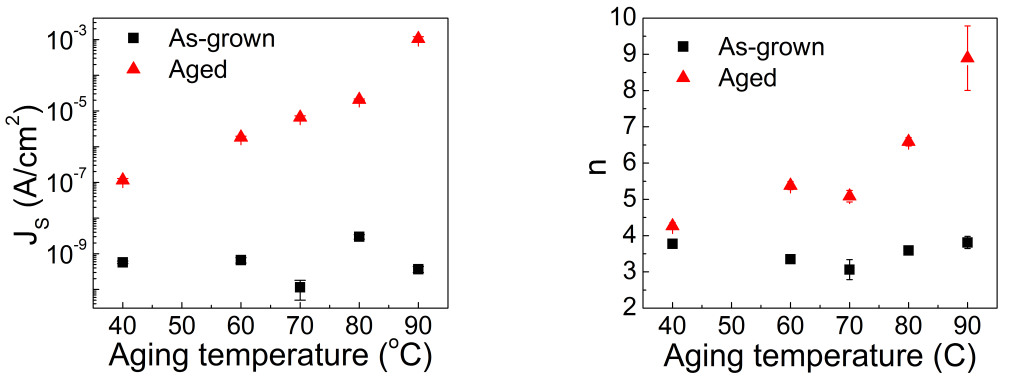

(a) (b)

Figure 8.6: (a) Reverse saturation current J_S and (b) ideality factor (n) of as grown (squares) and aged (triangles) Device M-60 from fits to the Shockley equation.

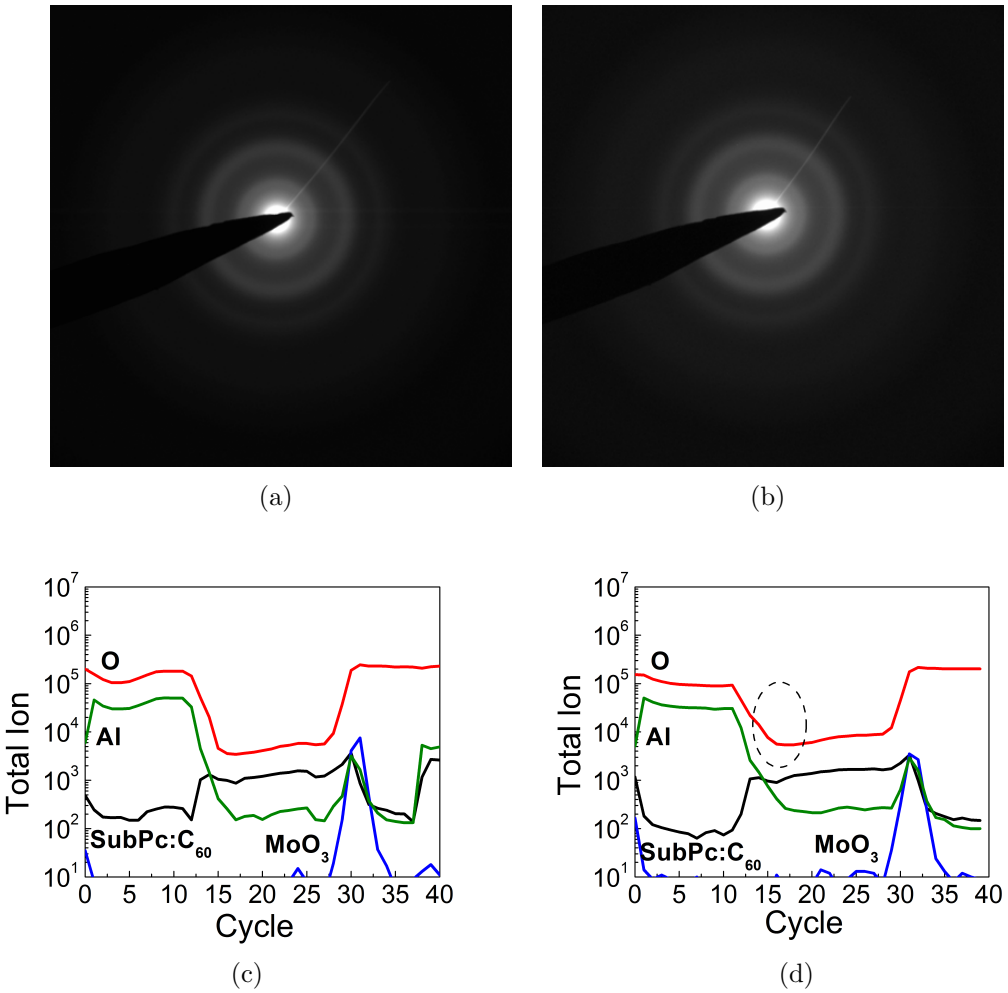

Figure 8.7: Selected area electron diffraction of Device M-60 after growth (a) and after aging at 80 ℃for 24 days (b). Secondary ion mass spectroscopy results of Device M-60 after growth (c) and after aging at 80 ℃for 24 days (d).

defect states that serve as recombination centers.

In conclusion, we investigated thermally-activated degradation in large area SubPc:C_{60} devices. The loss in efficiency is dominated by the decreased V_{OC}, due to the increase in recombination current. The recombination centers are resulted from oxygen diffusion from the cathode into the active layer. The degradation corresponds to an activation energy of 430 ± 60 meV, indicating sub-bandgap processes.

CHAPTER IX

Future outlook

Device reliability is arguably the most important research area in organic photovoltaic cells at present. In this chapter, we propose future directions in organic photovoltaic cells reliability research. We focus on areas that will advance understanding of the dynamics of excitons and polarons and the implications on device reliability and device/material design.

In Part II: Reliability of Organic Photovoltaic Cells, we have demonstrated that excited states are detrimental to OPV stability on many levels - morphology, molecular structure, absorption, and exciton generation and diffusion. In a planar structure, the exciton-induced degradation products shortens the lifetime of excited states, resulting in a significant reduction in photocurrent during the burn-in period. The degradation products could be trap states that quenches subsequently generated excitons, or polymerized products with shorter excited state lifetime. It will be interesting to accurately measure the post-burn-in film composition or exciton lifetime, in order to confirm the chemical degradation process. The degradation mechanism is suppressed by using a mixed donor/acceptor structure where the excitons are quickly dissociated. We have also shown that the exciton-induced photodegradation can be best mitigated by balancing the donor-to-acceptor ratio to 1:1. However, recent high-efficiency single cells have extremely imbalanced donor-to-acceptor ratio.[180] It is necessary to investigate how a donor-rich or acceptor-rich OPV degrades, particu-

larly the morphology degradation.

Another important next step to achieve stable high-efficiency OPVs is to understand the effect of charge carriers on device stability. We have shown in Chapter VI that for low-current OPVs ($J < 5$ mA/cm^2), charge does not introduce additional degradation mechanisms. However, as current density increases in more efficient OPVs, it is likely that polaron-polaron and polaron-exciton recombination will decrease device lifetime through similar pathways that have been observed in the OLED case.[163] Comparing device lifetime for a high-efficiency single cell vs. a tandem cell, where the current density can be drastically different, will bring interesting results on carrier-induced degradation. So far the research on tandem OPV reliability has been rare, yet promising.[181, 182]

In addition to photoactive layers, the stability of OPV buffer layers is crucial. Studies have shown that by eliminating corrosive PEDOT:PSS in polymer OLEDs, the device lifetime is substantially improved.[183] It was also found that BPhen is stablized by mixing Aluminum(III)bis(2-methyl-8-quinolinato)4-phenylphenolate (BAlq) due to its higher glass transition temperature.[184] Finding the most stable buffer layer will likely extend device lifetime, and allows for more focused research in degradation processes in the active layer.

In Chapter VII we have demonstrated that compared to C_{70}, C_{60} is inherently unstable due to its tendency to form polymerized C_{60}. Currently there is no broad understanding on how the molecular structure will affect OPV device lifetime. With deeper understanding of how exciton- and polaron-induced effects cause morphology and molecular changes, designing long-lifetime organic materials and device architecture will be achievable in the future.

APPENDICES

APPENDIX A

An integrated organic passive pixel sensor utilizing an inverted photodetector

Among organic optoelectronic devices, OPDs have attracted particular interest for use in optical imagers owing to their light weight, broad spectral detectivity and compatibility with flexible or conformal substrates. For example, a passive-matrix OPD imaging array has been demonstrated on a hemispherical substrate.[185, 186] However, such an OPD array is limited because the dark current is a function of the array size, scaling linearly with the number of rows or columns. Consequently, transistors must be used as switching elements to reduce the total leakage current. An organic passive pixel sensor was recently reported consisting of a bottom-contact (BC) pentacene OTFT and a bottom-illuminated SubPc/C_{60} OPD.[187] This integrated pixel achieved an 8-bit dynamic range, limited mainly by the low ON-drain current and hole mobility ($\mu = 0.0025$ cm^2/V·s) of the BC-OTFT. On the other hand, it has been shown that top-contact (TC) OTFTs have superior performance compared with BC-OTFTs owing to the improved carrier injection and reduced contact resistance.[188, 189, 190] However, the integration of bottom-illuminated OPDs and TC-OTFTs often involves complicated processing, such as photolithography, inkjet printing,[191] laser drilling or lamination.[192] Therefore, it is of interest to modify the pixel to include TC-OTFTs while retaining the simple fabrication process of bottom-contact devices.

In this chapter, we demonstrate a small-molecule organic passive pixel sensor

consisting of an inverted SubPc/C_{60} OPD described in Chapter III and a bottom-gate, top-contact pentacene OTFT. By using a transparent, sputter-deposited ITO anode, the top-illuminated OPD can be integrated with a TC-OTFT via thermal evaporation and shadow-mask patterning. The OTFT achieves a drain current ON/OFF ratio of 10^5 at a drain-source voltage, V_{DS} = -4 V, and carrier mobility (μ_m) = 0.09 ± 0.02 $cm^2/V{\cdot}s$, resulting in a 12-bit dynamic range for the circuit.

A.1 Experimental procedure

The integrated pixels in Fig. A.1 were fabricated on high thermal conductivity sapphire substrates to prevent heating during ITO sputtering. Prior to thermal deposition in a vacuum chamber with a base pressure $<4\times10^{-7}$ Torr, the substrates were cleaned by ultrasonication in acetone followed by immersion in boiling isopropanol. The OTFT gate and OPD cathode consisting of 50 nm-thick Al were simultaneously thermally evaporated. Next the OPD structure (C_{60} 50 nm/SubPc 9 nm/MoO_3 30 nm) was thermally evaporated at a rate of 1 Å/s. A 50 nm-thick ITO anode was sputtered at a power of 20 W (rate = 0.1 Å/s) using an argon plasma at a pressure of 2 mTorr. After depositing the OPD layers, the samples were loaded into a parylene deposition system where 0.7 g of parylene C (relative dielectric constant, $\epsilon_r = 3.15$) was coated onto the OTFT gate contact, forming a 270 nm-thick insulator. Finally, the 50 nm-thick pentacene channel and the 40 nm-thick Au source and drain contacts were sequentially evaporated at the rates of 0.5 Å/s and 0.3 Å/s, respectively, to complete the OTFT. All features were defined using shadow masks attached in an ultra-high-purity N_2 (<1 ppm O_2 and H_2O), with the exception of a brief exposure to air before and after parylene deposition. The OPD dimensions (100 μm ×800 μm) and OTFT channel width-to-length ratio (W/L = 500 μm/30 μm) were set by shadow-masking during ITO and Au deposition, respectively.

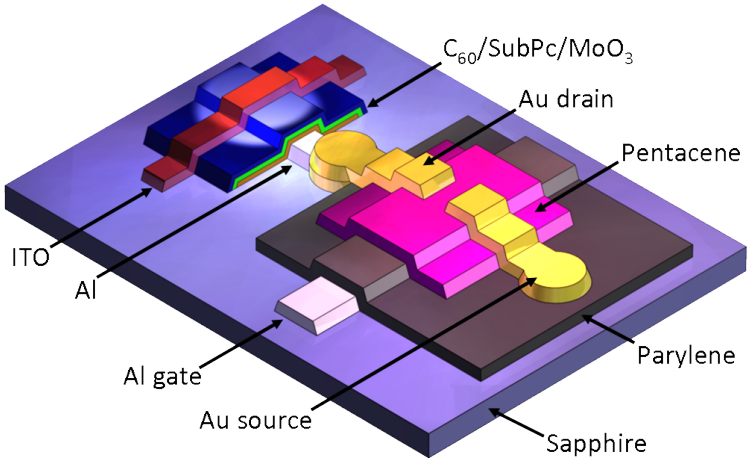

Figure A.1: Schematic diagram of the integrated passive pixel sensor consisting of a top-illuminated organic photodetector with an indium-tin-oxide (ITO) top contact in series with a pentacene organic thin film transistor. Layer compositions are indicated.

Device performance was measured in air using a semiconductor parameter analyzer. Incident light for measuring the circuit dynamic range (DR) was provided by a mercury lamp with a spectral bandpass filter at a center wavelength of $\lambda = 580 \pm 2$ nm, matching a Hg emission peak as well as the absorption maximum of SubPc. The illumination intensity was varied using neutral density filters and measured using a calibrated Si photodetector. EQE was measured using a lock-in amplifier and monochromated light from a tungsten-halogen lamp chopped at $\sim$ 200Hz. Voltage was applied to the detector with a current amplifier at the input to the lock-in for biased EQE measurement. The circuit transient response was measured using an oscilloscope and a pulse generator with rise and fall times of 2 ns controlling the transistor gate.

A.2 Performance of individual sensor and transistor components

The characteristics of the discrete pixel components were individually measured with results shown in Fig. A.2 and Fig. A.3. The OTFT output characteristic is shown in Fig. A.2(a). The drain current (I_{DS}) when the transistor is in the OFF state is $I_{DS} = 27 \pm 3$ pA at V_{DS} = -4 V, and the ON/OFF ratio is 10^5 (Fig. A.2(b)). The OFF current is comparable to that of a BC-OTFT at a small V_{DS}.[187], while the ON current is improved by more than two orders of magnitude. The field-effect hole mobility, $\mu_m = 0.09 \pm 0.02$ cm^2/V·s, was obtained using $I_{DS} = \frac{\mu_m WC}{2L}(V_{GS} - V_{th})^2$ in the saturation region, where C is the gate-insulator capacitance, V_{GS} is the gate voltage, and V_{th} is the threshold voltage. The OTFT ON current is comparable to previously reported bottom-gate pentacene transistors employing a polymer gate dielectric, while the low OFF current was achieved with a much smaller dielectric thickness (270 nm) than a previously reported thickness of >500 nm.[193] This is attributed to reduced gate leakage due to small gate-source overlap (<350μm ×500μm).

The current-voltage (I_{OPD}-V) response of the OPD is shown in Fig. A.3(a). Under a reverse bias of -1.5 V, the OPD dark current is $I_{Dark} = 20$ pA. Also $EQE = 18.2$ % at $\lambda = 580$ nm, and increases to 19.9 % at -2 V due to increased polaron-pair dissociation at high voltages (Fig. A.3(b)).[74] The EQE of an analogous inverted discrete OPD is also shown in Fig. A.3(b). The EQE of both devices is within device-to-device variations. Over the range of incident optical powers used here (from 2.6 μW/cm^2 to 151 mW/cm^2), the OPD photocurrent is linear, resulting in a high detection DR. The photodetector specific detectivity (D^*) at -1.5 V is shown in Fig. A.3(b). Now, D^* is calculated using $D^* = \sqrt{A\Delta f}/\text{NEP}$, where A is the detector area, Δf is the bandwidth, and NEP is the noise equivalent power.[186] Under reverse bias, shot noise

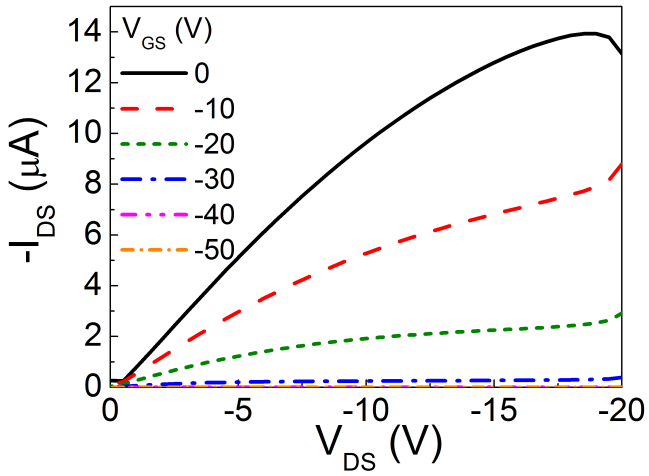

(a)

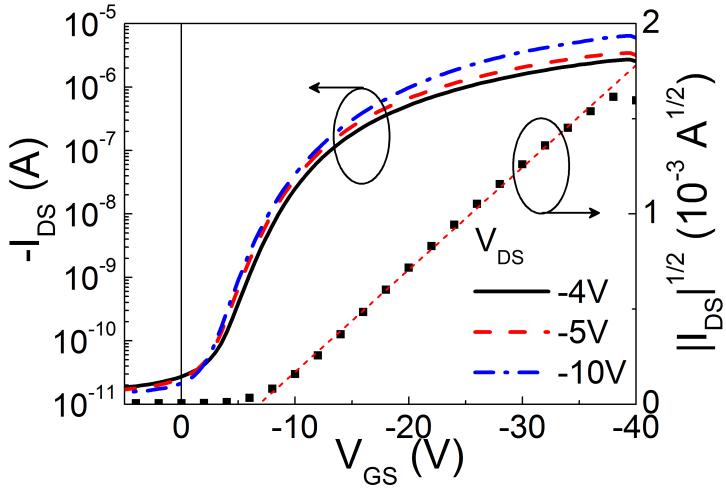

(b)

Figure A.2: Characteristics of a discrete pentacene thin-film transistor. (a) Output characteristics for V_{GS} = 0, -10, -20, -30, -40 and -50 V. (b) Transfer characteristics of I_{DS} vs. V_{GS} of the OTFT at a drain-source voltage of V_{DS} = -4 V (solid line), -5 V (dashed line) and -10 V (dash-dotted line). The square-root of the drain-source current (squares) and the fit (short-dashed line) are shown on the right-hand axis.

dominates the NEP, giving $D^* = \sqrt{A\Delta f} \cdot R/\sqrt{2qI_{Dark}}$, where R is the responsivity, and q is the elementary charge. At $\lambda = 580$ nm, $D^* = 9.4 \times 10^{11}$ cm·Hz$^{1/2}$·W^{-1}.

A.3 An integrated organic pixel sensor

The integrated pixel performance was characterized by measuring the current between the anode of the OPD and the source of the OTFT (I_{AS}) under various light intensities and V_{GS} (Fig. A.4). The pixel has a dark OFF current of $I_{AS} = 31 \pm 5$ pA and dark ON current of 950 ± 130 pA. The dark OFF current is consistent with the OFF current of the discrete OTFT within measurement error. The slight difference is due to the change in V_{DS} across the sample from testing the discrete OTFT (V_{DS} = -4 V) vs. testing the integrated pixel (V_{AS} = -4 V). The dark ON current of the pixel at V_{AS} = -4 V is noticeably higher than that of the OPD at -1.5 V in Fig. A.3(a). Nevertheless, this pixel performance is sufficient for application to a 30×30 sensor array.

The lowest detectable light intensity is 17 μW/cm^2, as shown in Fig. A.5, establishing a lower limit to the DR. Since the OPD photocurrent does not saturate within the testing range used, the upper limit is determined by the ON current (4.6±0.05 μA) of the OTFT at light intensities >130 mW/cm^2. Furthermore, ΔI_{AS} is the difference between the ON current undre illumination and in the dark at a gate bias, V_{GS} = -39.5 V. Fitting the pixel photocurrent ΔI_{AS} vs. incident illumination power gives R = 0.083 ± 0.003 A/W, consistent with the EQE result. The pixel showed a 12-bit dynamic range (corresponding to $DR = \Delta I_{AS}(\max)/\Delta I_{AS}(\min) = 4.1 \times 10^3$). The improved performance is due to the enhance ON current of TC-OTFTs compared with previously reported BC transistors.[187]

The pixel response time is determined by measuring the voltage across a resistor

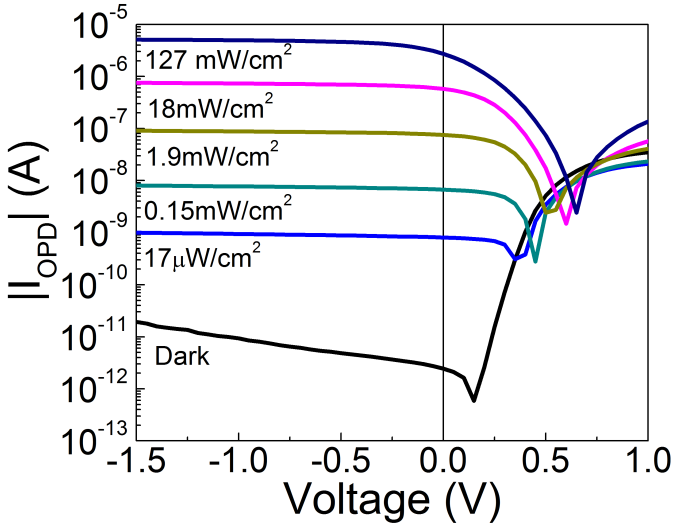

(a)

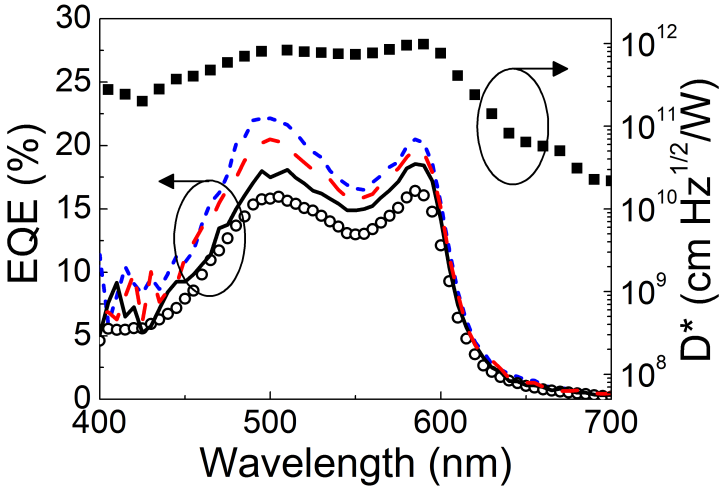

(b)

Figure A.3: (a) current-voltage characteristics of the organic photodetector (I +$_{OPD}$ -V) in the dark and under illumination at different intensities. The incident wavelength is $\lambda = 580 \pm 2$ nm. (b) EQE of the integrated SubPc/C_{60} OPD under 0 V bias (solid line), -1 V (dashed line) and -2 V reverse bias (short-dashed line), compared to that of a control inverted OPD (open circles). The specific detectivity (D^*) at -1.5 V is shown on the right-hand axis (squares).

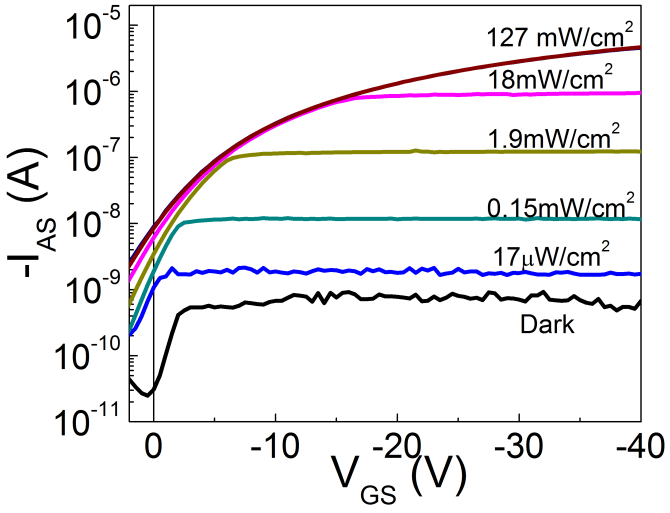

Figure A.4: Transfer characteristics of the integrated pixel. Anode-source current (I_{AS}) vs. V_{GS} at an anode-source voltage of -4 V for various illumination intensities at $\lambda = 580 \pm 2$ nm.

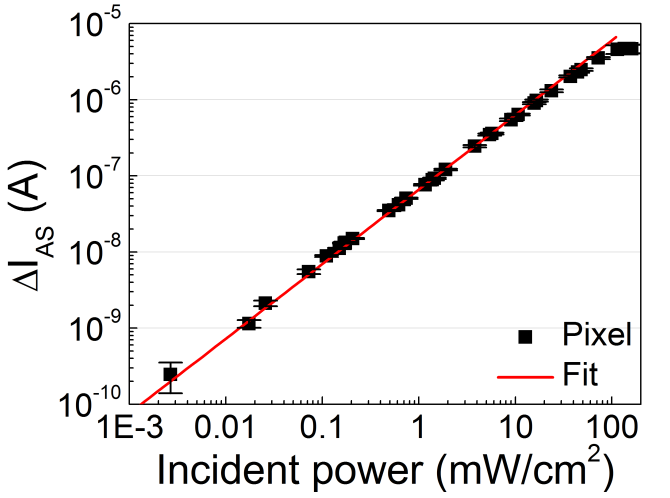

Figure A.5: Pixel photoresponse, ΔI_{AS}, as a function of incident illumination power intensity extracted from the transfer characteristics at V_{GS} = -39.5 V, where ΔI_{AS} is the difference between I_{AS} under illumination and in the dark. The line is a linear fit to the data. The extent of the linear range of the data gives the circuit dynamic range, equal to 12 bits.

between the source of the OTFT and ground. A pulsed V_{GS} from +2 V (OFF state) to -40 V (ON state) is applied while the device was kept under a constant anode-source voltage (V_{AS}) = -4 V and an illumination intensity of 49 mW/cm^2. The resulting data were modeled by a bi-exponential decay following Eq. A.1.

$$-I_{AS} = I_0 + A_1 \exp\left[-\left(t - t_0\right)/\tau_P\right] + A_2 \exp\left[-\left(t - t_0\right)/t_{RO}\right] \qquad \text{(A.1)}$$

,

Here I_0 is the steady state pixel current when the gate is ON, and t_0 is the time when the pulse is applied (Fig. A.6). The RC charging time constant is τ = 29$\pm$8 μs when using a 37.7 kΩ load, corresponding to the fast decay initially observed. Previously, it has been found that the optical response of analogous SubPc/C_{60} OPDs is on the order of nanoseconds,[187, 194] indicating that the circuit response time t_{RO} is limited by the discarging time through the OTFT channel. Note that τ_{RO} is larger than the charge travel time in the channel derived from mobility (25 μs), indicating charge trapping in the channel. This response can be further improved by using a transistor with a higher mobility employing, for example, self-assembled monolayers at the insulator-channel interface that result in enhanced crystal orientation.[195, 193, 196]

In conclusion, an organic integrated pixel based on a bottom-gate, top-contact pentacene transistor and an inverted SubPc/C_{60} photodetector has been demonstrated. It has a 12-bit dynamic range, an OFF current of 31 $\pm$ 5 pA, and a read-out time of 0.4 $\pm$ 0.05 ms. The circuit performance is adequate for use in video-rate, high-sensitivity focal plane arrays of dimensions of at least 30 $\times$ 30 pixels.

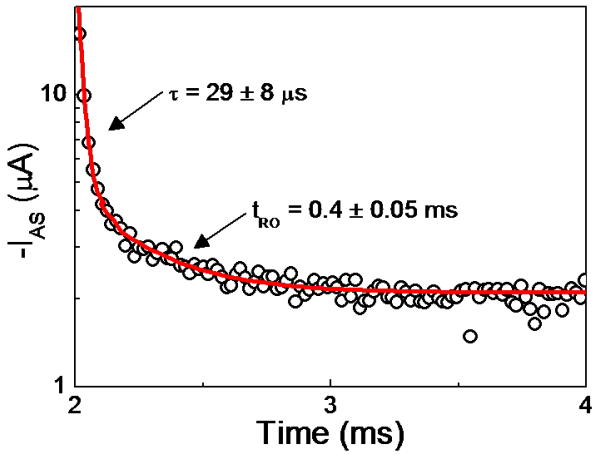

Figure A.6: Transient response of the pixel to a square voltage pulse applied at the transistor gate electrode measured using a 37.7 kΩ load. Also shown (line) is a bi-exponential decay fit to the data. The time constants extracted from the fit are the read-out time of $\tau_{RO} = 0.4 \pm 0.05$ ms, and the RC time constant of $\tau = 29 \pm 8\mu$s.

APPENDIX B

Modeling of current generation in solar cells

A transfer matrix formalism allows for efficient modeling of the local optical field amplitude in planar layered structures.[15] The current generation in an OPV device can be estimated by optical modeling combined with calculation of exciton diffusion. Here, we summarize the well-established simulation methods and provides means to high-performance implementation.

B.1 Optical modeling of multilayer dielectrics

We consider uniform plane waves incident normally on the interfaces of a multilayer structure. The materials are assumed to be homogeneous and isotropic with optically flat interfaces. The optical fields across different layers are related by a 2×2 matrix - a transfer matrix. All variables in this section are a function of the incident wavelength, λ, thus the dependence (λ) is omitted.

Consider an optical field propagating along the x direction in the multilayer structure shown in Fig. B.1. Each layers has a thickness of d_j, where j is the index of the layer. The 0^{th} and m$+1^{th}$ layers are the semi-infinite ambient environment. The optical properties of each layer is described by the complex index of refraction:

$$\overline{n_j} = n_j + i \cdot k_j \tag{B.1}$$

where n_j and k_j are the refractive index and extinction coefficient of the layer, re-

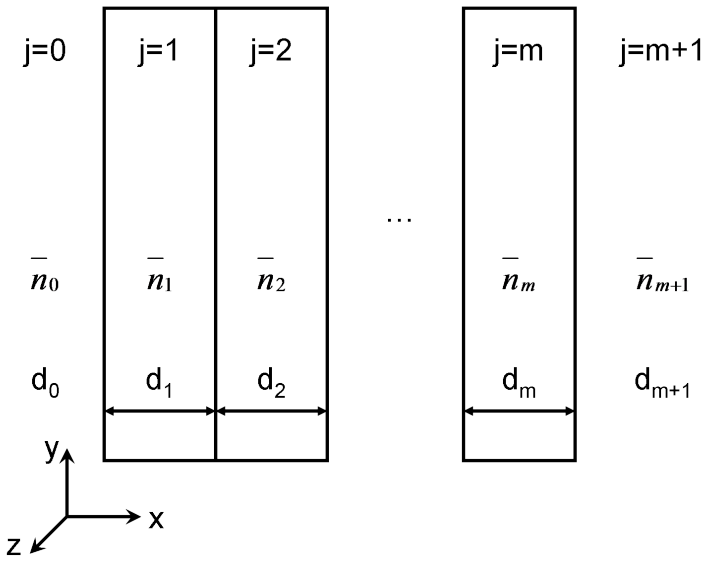

Figure B.1: A multilayer thin-film device.

spectively.

The schematic of the fields across an interface between layer j and layer $j+1$ is shown in Fig. B.2. Here, the notations $+$ and $-$ indicate the propagation direction of the electric field. Prime ($'$) indicates different materials. Symbols r and t are the Fresnel reflection and transmision coefficient, respectively.

The boundary conditions require that the total electric and magnetic fields be continuous across the interface:

$$E = E^+ + E^- = E' = E^{+\prime} + E^{-\prime} \tag{B.2a}$$

$$H = \frac{1}{\eta}\left(E^+ - E^-\right) = H' = \frac{1}{\eta'}\left(E^{+\prime} - E^{-\prime}\right) \tag{B.2b}$$

Here, $\eta = \sqrt{\mu/\epsilon}$ is the characteristic impedance of the dielectric, where μ and ϵ are the permeability and permittivity of the material, respectively.

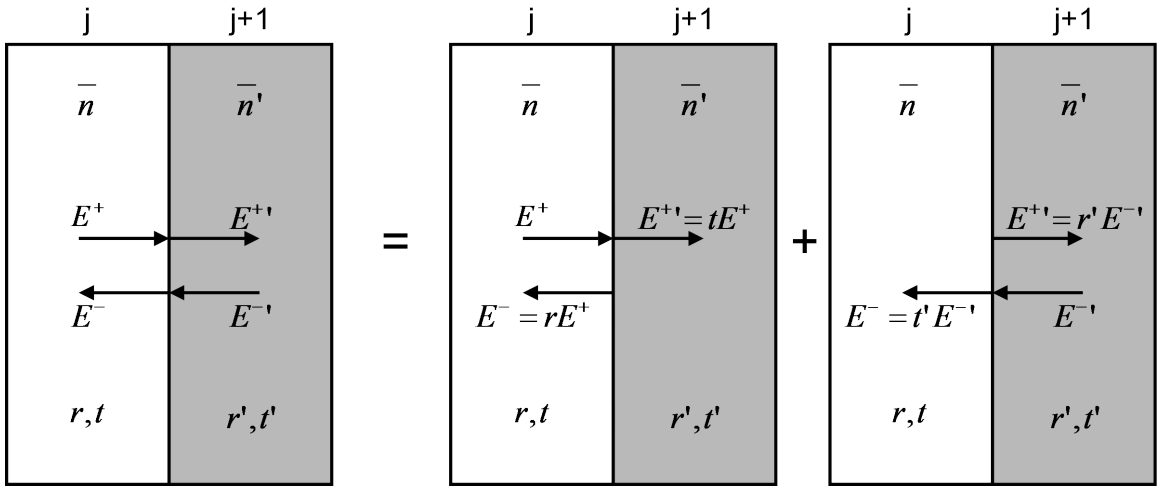

Figure B.2: Fields across an interface between two dielectric thin films. The notations + and − indicate the propagation direction of the field. Prime ($'$) indicates different materials. Symbols r and t are the Fresnel reflection and transmision coefficient, respectively.

The Fresnel reflection and transmission coefficient are:

$$r = r_{j(j+1)} = \frac{\overline{n_j} - \overline{n_{j+1}}}{\overline{n_j} + \overline{n_{j+1}}}; \tag{B.3a}$$

$$t = t_{j(j+1)} = \frac{2\overline{n_j}}{\overline{n_j} + \overline{n_{j+1}}}; \tag{B.3b}$$

Eq. B.2a and B.2b can be written in a matrix form:

$$\begin{bmatrix} E^+ \\ E^- \end{bmatrix} = \frac{1}{t_{j(j+1)}} \begin{bmatrix} 1 & r_{j(j+1)} \\ r_{j(j+1)} & 1 \end{bmatrix} \begin{bmatrix} E^{+\prime} \\ E^{-\prime} \end{bmatrix} \tag{B.4}$$

The interface matrix is therefore defined as:

$$I_{j(j+1)} = \frac{1}{t_{j(j+1)}} \begin{bmatrix} 1 & r_{j(j+1)} \\ r_{j(j+1)} & 1 \end{bmatrix}, \tag{B.5}$$

As shown in Fig. B.3, the field propagating through a layer of dielectric thin film is related in a matrix form as:

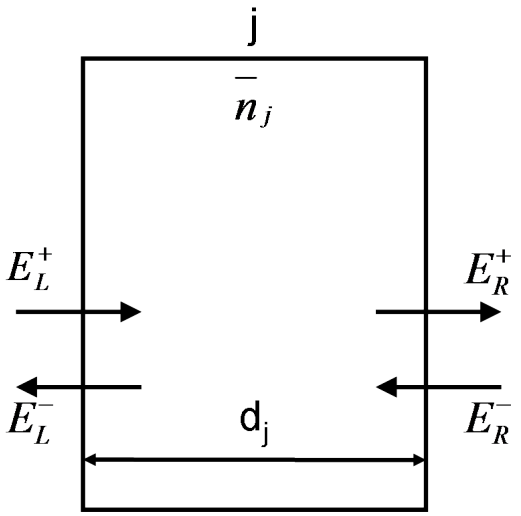

Figure B.3: Field propagated through a dielectric layer.

$$\begin{bmatrix} E_L^+ \\ E_L^- \end{bmatrix} = \begin{bmatrix} e^{-id_j\xi_j} & 0 \\ 0 & e^{id_j\xi_j} \end{bmatrix} \cdot \begin{bmatrix} E_R^+ \\ E_R^- \end{bmatrix} \tag{B.6}$$

where $\xi_j = 2\pi\overline{n_j}/\lambda$. The layer propagation matrix is:

$$L_j = \begin{bmatrix} e^{-id_j\xi_j} & 0 \\ 0 & e^{id_j\xi_j} \end{bmatrix} \tag{B.7}$$

The fields incident on the multilayer structure from the left to those from the right is linked by the product of a series of propagation and interface matrices, viz:

$$S = \begin{bmatrix} S_{11} & S_{12} \\ S_{21} & S_{22} \end{bmatrix} = \frac{1}{t_{jk}} \cdot \begin{bmatrix} 1 & r_{jk} \\ r_{jk} & 1 \end{bmatrix} = \left(\prod_{n=1}^{m} I_{(n-1)n} L_n \right) \cdot I_{m(m+1)}, \tag{B.8}$$

$$S = S_j^- L_j S_j^+, \tag{B.9}$$

with (B.10)

$$S_j^- = \left(\prod_{n=1}^{j-1} I_{(n-1)n} L_n \right) \cdot I_{(j-1)j}, \tag{B.11}$$

and (B.12)

$$S_j^+ = \left(\prod_{n=j+1}^{m} I_{(n-1)n} L_n \right) \cdot I_{(m-1)m}. \tag{B.13}$$

The electric field at the left interface of layer j is related to the incident field by:

$$\frac{E_j^+}{E_0^+} = t_j^+ = \frac{\frac{1}{S_{j11}^-}}{1 + \frac{S_{j12}^- S_{j21}^+}{S_{j11}^- S_{j11}^+} e^{i2d_j\xi_j}}; \tag{B.14}$$

$$\frac{E_j^-}{E_0^+} = t_j^- = t_j^+ \frac{S_{j21}^+}{S_{j11}^+} e^{i2d_j\xi_j}. \tag{B.15}$$

The total electric field at position x of layer j is:

$$E_j(x) = E_j^+(x) + E_j^-(x) = \left(t_j^+ e^{ix\xi_j} + t_j^- e^{-ix\xi_j} \right) E_0^+. \tag{B.16}$$

In general, the multilayer structure is supported by a substrate with thickness $d \gg \lambda$. The effect of the substrate is calculated by including the reflection at the air/substrate and substrate/multilayer interfaces instead of including it in the transfer matrix.

$$R' = \frac{R_{Air/Sub} + R_{Sub/Stack}}{1 + R_{Air/Sub} \times R_{Sub/Stack}} \tag{B.17}$$

$$T' = \frac{T_{Air/Sub} \times T_{Sub/Stack}}{1 + T_{Air/Sub} \times T_{Sub/Stack}} \tag{B.18}$$

with

$$R_{Air/Sub} = \left| \frac{1 - \overline{n_{Sub}}}{1 + \overline{n_{Sub}}} \right|^2, \tag{B.19}$$

$$T_{Air/Sub} = \left| \frac{2}{1 + \overline{n_{Sub}}} \right|^2, \tag{B.20}$$

and

$$R_{Sub/Stack} = \left| \frac{S_{21}}{S_{11}} \right|^2 \tag{B.21}$$

$$T_{Sub/Stack} = \left| \frac{S_{21}}{S_{11}} \right|^2 \cdot \frac{\overline{n_{m+1}}}{\overline{n_0}} \tag{B.22}$$

$$\tag{B.23}$$

The aborption efficiency is $\eta_A = 1 - R' - T'$. The optical field at position x is corrected to:

$$E_j(x) = E_j^+(x) + E_j^-(x) = \left(t_j^+ e^{ix\xi_j} + t_j^- e^{-ix\xi_j} \right) E_0^+ (1 - R' - T') \tag{B.24}$$

The overall time-averaged absorbed power at position x in layer j is

$$Q_j(x) = \frac{4\pi c \epsilon_0 k_j n_j}{2\lambda} \left| E_j(x) \right|^2 \tag{B.25}$$

B.2 Modeling of exciton diffusion in planar organic solar cells

The power intensity of the local optical field determines the exciton generation rate. The exciton density at wavelength, λ, and position, x, is calculated by the steady-state exciton diffusion equation:

$$\frac{\partial N_X\left(x,\lambda\right)}{\partial t} = D\frac{\partial^2 N_X\left(x,\lambda\right)}{\partial x^2} - k_0 N_X\left(x,\lambda\right) + G\left(x,\lambda\right) = 0 \tag{B.26}$$

Here, $N_X\left(x,\lambda\right)$ is the exciton density generated by absorption of photons of wavelength, λ, and at position, x. Also, D is the exciton diffusivity, k_0 is the exciton natural decay rate including the natural (τ_0) and nonradiative (τ_{nr}) decay lifetimes (i.e.,$k_0 = 1/\tau_0 + 1/\tau_{nr}$), and $G\left(x,\lambda\right)$ is the photogeneration rate of excitons in the device active layers determined by the local intensity of the optical electric field. Assuming unity photon absorption efficiency, $G\left(x,\lambda\right) = Q(x,\lambda)/(hc/\lambda)$.

Eq. B.26 is solved by using boundary conditions:
(i)Ideal non-quenching interface:

$$\left.\frac{\partial N_X}{\partial x}\right|_{Boundary} = 0; \tag{B.27}$$

and (ii)Ideal exciton dissociation interface:

$$N_X|_{Boundary} = 0. \tag{B.28}$$

The case of partial-quenching interface with finite exciton dissociation rate is not considered here.

The EQE of the device is the exciton flux at the dissociating interface normalized to the incident field:

$$EQE(\lambda) = D\frac{\partial N_X(x,\lambda)}{\partial x}\Big|_{D/A}\Big/\frac{1}{2}\frac{c\epsilon_r\epsilon_0|E|^2}{hc/\lambda} \tag{B.29}$$

Such boundary value problems (BVPs) of ordinary differential equations (ODEs) can be solved using numerical methods. Details on numerical methods and algorithm are in Ref. [197]. There are many effective programs for solving BVPs. In this section we discuss implementation of solving Eq. B.26 using a common BVP solver, MATLAB® bvp4c.[198]

The solver bvp4c implements a collocation method for the solution of BVPs of the form:

$$y' = f(x, y, p), a \leq x \leq b, \text{ subject to: } g\left(y(a), y(b), p\right) = 0. \tag{B.30}$$

Here p is a vector of unknown parameters in the general nonlinear, two-point boundary conditions.

The solver bvp4c requires the ODEs to be written as a system of first order ODEs - one for each variable in the original problem and one for each of its derivatives up to one less than the highest derivative appearing. To solve Eq. B.26, set $y_1(x) = N_X\left(x, \lambda\right)$ and $y_2(x) = \partial N_X\left(x, \lambda\right)/\partial x$. The required inputs are:

$$dydx = \begin{bmatrix} y_1' \\ y_2' \end{bmatrix} = \begin{bmatrix} y_2 \\ \frac{1}{D}\left(k_0 y_1 - G(x, \lambda)\right) \end{bmatrix} \tag{B.31}$$

Assuming the simple case of a photoactive layer in a planar OPV cell that the left interface is non-quenching and the right one is exciton dissociating. The boundary conditions are:

$$y_2(a) = 0 \text{ and } y_1(b) = 0. \tag{B.32}$$

Once the exciton density is solved, the EQE of the device is calculated as the dissociated exciton flux at the D/A interface divided by the incoming photon density.

Certainly the run time of the program depends on the hardware and its configuration. Yet the performance of the BVP solver can be significantly improved by

proper coding. There are a number of references discussing ways to efficiently implement numerical methods in great details.[199, 200, 201, 202] Here we summarize a few methods to shorten the elapse time of the program:

(a) Including the partial derivatives of the ODE and boundary conditions.

BVPs are generally solved much faster with improved robustness when the analytical partical derivatives are given. One can inform the solver of functions for evaluating the partial derivatives for ODEs as well as for the boundary conditions. Some BVPs do not have convenient analytical form of partial derivatives, thus it is often not required to provide it in BVP solvers. However, including them when possible, at least the Jacobian of the ODEs, can substantially reduce the run time.

The exciton diffusion equation have straightforward expressions for the partial derivatives.

$$J = \frac{\partial dydx}{\partial y} = \begin{bmatrix} \frac{\partial dydx_1}{\partial y_1} & \frac{\partial dydx_1}{\partial y_2} \\ \frac{\partial dydx_2}{\partial y_1} & \frac{\partial dydx_2}{\partial y_2} \end{bmatrix} = \begin{bmatrix} 0 & 1 \\ \frac{1}{D} & 0 \end{bmatrix} \tag{B.33}$$

The function for evaluating the partial derivatives of the boundary condition $g\left(y(a), y(b), p\right) = 0$ involves two vectors: $\partial g/\partial ya$ and $\partial g/\partial yb$. The Jacobian of the boundary conditions should be provided according to the types of boundary condition. For the example shown in Eq. B.32, the Jacobians are:

$$\mathrm{dBCd}ya = \begin{bmatrix} 0 & 1 \\ 0 & 0 \end{bmatrix}, \text{ and} \tag{B.34a}$$

$$\mathrm{dBCd}yb = \begin{bmatrix} 0 & 0 \\ 1 & 0 \end{bmatrix} \tag{B.34b}$$

(b) Vectorizing the input.

Many MATLAB® BVP solvers forms Jacobians using finite differences by default. Vectorizing the evaluation of the ODE function can significantly shorten the run time. To utilize vectorization, code the ODE such that $F([x1, x2, ...], [y1, y2, ...])$ returns $[(x1, y1), (x2, y2)...]$. This way, the ODE function passes to the solver a whole array of vectors at once, reducing the number of function evaluations and therefore the run time. The options of vectorization and supplying analytical Jacobians are independent. One may be more effective at reducing run time than the other depending on the types of BVPs. Note that for stiff ODE solvers, vectorization is ignored when analytical Jacobians are provided. bvp4c benefits from vectorization even when analytical Jacobians are used, thus one should include both whenever possible to speed up computation to its maximum.

(c) Utilizing parallel computing.

The Parallel Computing Toolbox™ in MATLAB® uses multicore processors, graphics processing units (GPUs) and computer clusters to solve computationally intense problems. In order to use the Parallel Computing Toolbox™ , every iteration must be independent. That is, the variables used in one iteration do not reference results from other iterations. When solving the exciton diffusion equation across the incident spectrum, each solution at different wavelengths can be handled by the Parallel Computing Toolbox™ since they are all independent from each other. This speeds up the computation when using multicore processor and is very easy to implement without reprogramming.

Modeling provides a powerful way to predict device performance and optimize material selection and device structure. As computation becomes more complicated, such as designing tandem devices, it is essential to fully take advantage of the existing resources, thus significantly expands the computation capability, allowing for efficient OPV modeling and design.

APPENDIX C

List of Publications

C.1 Journal publications

[1] Xiaoran Tong, Nana Wang, Michael Slootsky, Junsheng Yu, and Stephen R. Forrest. Intrinsic burn-in efficiency loss of small-molecule organic photovoltaic cells due to exciton-induced trap formation. *Solar Energy Materials and Solar Cells*, 118:116–123, November 2013.

[2] Xiaoran Tong and Stephen R. Forrest. An integrated organic passive pixel sensor. *Organic Electronics*, 12(11):1822–1825, November 2011.

[3] Xiaoran Tong, Brian E. Lassiter, and Stephen R. Forrest. Inverted organic photovoltaic cells with high open-circuit voltage. *Organic Electronics*, 11(4):705–709, April 2010.

[4] Xiaoran Tong, Rhonda F. Bailey-Salzman, Guo dan Wei, and Stephen R. Forrest. Inverted small molecule organic photovoltaic cells on reflective substrates. *Applied Physics Letters*, 93(17):173304–3, October 2008.

[5] Nana Wang, Xiaoran Tong, Quinn Burlingame, Junsheng Yu, and Stephen R. Forrest. Photodegradation of small-molecule organic photovoltaics. *Solar Energy Materials and Solar Cells*, 125:170–175, June 2014.

[6] Nana Wang, Jeramy D. Zimmerman, Xiaoran Tong, Xin Xiao, Junsheng Yu, and Stephen R. Forrest. Snow cleaning of substrates increases yield of large-area organic photovoltaics. *Applied Physics Letters*, 101(13):133901–4, September 2012.

C.2 Conference contributions

[1] Xiaoran Tong, Nana Wang, Michael Slootsky, and Stephen Forrest. Exciton-induced degradation of photocurrent in small-molecule organic solar cells. In *Bul-*

letin of the American Physical Society, volume 58, Number 1. American Physical Society, March 2013.

[2] Xiaoran Tong and Stephen R. Forrest. Integrated organic thin-film transistor with an inverted organic photodetector. In *ICEL 2010 - 8th International Conference on Electroluminescence & Organic Optoelectronics*, October 2010.

[3] Xiaoran Tong and Stephen R. Forrest. The open-circuit voltage of inverted small molecule organic photovoltaic cells. In *Symposium S: Organic Materials and Devices for Sustainable Energy Systems - 2009 MRS Fall Meeting*, November 2009.

[4] Xiaoran Tong, Stephen R. Forrest, and Rhonda Bailey-Salzman. Inverted small molecule organic photovoltaic cells. In *Symposium H: Physics and Technology of Organic Semiconductor Devices - 2008 MRS Fall Meeting*, December 2008.

[5] Jung-Yong Lee, Steve T. Connor, Xiaoran Tong, Yi Cui, Stephen R. Forrest, and Peter Peumans. Enhanced outcoupling of organic light emitting devices via metal nanowire mesh transparent electrodes. In *Symposium B: Transparent Conductors and Semiconductors for Optoelectronics - 2008 MRS Fall Meeting*, December 2008.

C.3 Patents

[1] Stephen R. Forrest, Xiaoran Tong, Jun Yeob Lee, and Yong Joo Cho. Methods of preparing the surface of metal substrates for organic photosensitive devices, May 2013. US20130105779 A1.

BIBLIOGRAPHY

BIBLIOGRAPHY

[1] Martin Pope and Charles E. Swenberg. *Electronic processes in organic crystals and polymers*. Oxford University Press, 1999.

[2] Frederik C. Krebs, Jan Fyenbo, and Mikkel Jrgensen. Product integration of compact roll-to-roll processed polymer solar cell modules: methods and manufacture using flexographic printing, slot-die coating and rotary screen printing. *Journal of Materials Chemistry*, 20(41):8994–9001, October 2010.

[3] Roar R. Sndergaard, Markus Hsel, and Frederik C. Krebs. Roll-to-roll fabrication of large area functional organic materials. *Journal of Polymer Science Part B: Polymer Physics*, 51(1):1634, 2013.

[4] N. S. Sariciftci, D. Braun, C. Zhang, V. I. Srdanov, A. J. Heeger, G. Stucky, and F. Wudl. Semiconducting polymerbuckminsterfullerene heterojunctions: Diodes, photodiodes, and photovoltaic cells. *Applied Physics Letters*, 62(6):585–587, February 1993.

[5] R.H. Friend, G.J. Denton, J.J.M. Halls, N.T. Harrison, A.B. Holmes, A. Khler, A. Lux, S.C. Moratti, K. Pichler, N. Tessler, K. Towns, and H.F. Wittmann. Electronic excitations in luminescent conjugated polymers. *Solid State Communications*, 102(23):249–258, April 1997.

[6] J. Cornil, D. Beljonne, J.-P. Calbert, and J.-L. Brdas. Interchain interactions in organic -conjugated materials: Impact on electronic structure, optical response, and charge transport. *Advanced Materials*, 13(14):1053–1067, 2001.

[7] S. F. Nelson, Y.-Y. Lin, D. J. Gundlach, and T. N. Jackson. Temperature-independent transport in high-mobility pentacene transistors. *Applied Physics Letters*, 72(15):1854–1856, April 1998.

[8] Qian Miao, Thuc-Quyen Nguyen, Takao Someya, Graciela B. Blanchet, and Colin Nuckolls. Synthesis, assembly, and thin film transistors of dihydrodiazapentacene: an isostructural motif for pentacene. *Journal of the American Chemical Society*, 125(34):10284–10287, August 2003.

[9] Richard R. Lunt, Noel C. Giebink, Anna A. Belak, Jay B. Benziger, and Stephen R. Forrest. Exciton diffusion lengths of organic semiconductor thin films measured by spectrally resolved photoluminescence quenching. *Journal of Applied Physics*, 105(5):053711–7, March 2009.

[10] Jeramy D. Zimmerman, Xin Xiao, Christopher Kyle Renshaw, Siyi Wang, Vyacheslav V. Diev, Mark E. Thompson, and Stephen R. Forrest. Independent control of bulk and interfacial morphologies of small molecular weight organic heterojunction solar cells. *Nano Letters*, 12(8):4366–4371, August 2012.

[11] S. C. Ganguly and N. K. Chaudhuri. Directional properties of single crystal of anthracene regarding fluorescence phenomena. *The Journal of Chemical Physics*, 19(5):617–618, May 1951.

[12] S. Kna-Cohen and S. R. Forrest. Room-temperature polariton lasing in an organic single-crystal microcavity. *Nature Photonics*, 4(6):371–375, June 2010.

[13] M. A. Baldo, S. Lamansky, P. E. Burrows, M. E. Thompson, and S. R. Forrest. Very high-efficiency green organic light-emitting devices based on electrophosphorescence. *Applied Physics Letters*, 75(1):4–6, July 1999.

[14] Wade A. Luhman and Russell J. Holmes. Investigation of energy transfer in organic photovoltaic cells and impact on exciton diffusion length measurements. *Advanced Functional Materials*, 21(4):764771, 2011.

[15] Peter Peumans, Aharon Yakimov, and Stephen R. Forrest. Small molecular weight organic thin-film photodetectors and solar cells. *Journal of Applied Physics*, 93(7):3693–3723, April 2003.

[16] J. Frenkel. On the transformation of light into heat in solids. i. *Physical Review*, 37(1):17–44, January 1931.

[17] Gregory H. Wannier. The structure of electronic excitation levels in insulating crystals. *Physical Review*, 52(3):191–197, August 1937.

[18] S. Kazaoui, N. Minami, Y. Tanabe, H. J. Byrne, A. Eilmes, and P. Petelenz. Comprehensive analysis of intermolecular charge-transfer excited states in c-60 and c-70 films. *Physical Review B*, 58(12):7689–7700, September 1998.

[19] Theodor Frster. *Delocalized Excitation and Excitation Transfer*. Florida State University, 1965.

[20] D. L. Dexter. A theory of sensitized luminescence in solids. *The Journal of Chemical Physics*, 21(5):836–850, May 1953.

[21] P. Avakian and R. E. Merrifield. Experimental determination of the diffusion length of triplet excitons in anthracene crystals. *Physical Review Letters*, 13(18):541–543, November 1964.

[22] D. F. Williams and J. Adolph. Diffusion length of triplet excitons in anthracene crystals. *The Journal of Chemical Physics*, 46(11):4252–4254, June 1967.

[23] V. M. Agranovich and Yu. V. Konobeev. Diffusion of free excitons in molecular crystals. *physica status solidi (b)*, 27(1):435–442, 1968.

[24] Vladimir Moiseevich Agranovich and M. D. Galanin. *Electronic Excitation Energy Transfer in Condensed Matter*. North-Holland Publishing Company, 1982.

[25] Subrahmanyan Chandrasekhar. Stochastic problems in physics and astronomy. *Reviews of Modern Physics*, 15(1):1–89, January 1943.

[26] Bernhard Dick and Bernhard Nickel. Accessibility of the lowest quintet state of organic molecules through triplet-triplet annihilation; an indo ci study. *Chemical Physics*, 78(1):1–16, July 1983.

[27] Jean-Luc Brdas, Joseph E. Norton, Jrme Cornil, and Veaceslav Coropceanu. Molecular understanding of organic solar cells: The challenges. *Accounts of Chemical Research*, 42(11):1691–1699, November 2009.

[28] Askat E. Jailaubekov, Adam P. Willard, John R. Tritsch, Wai-Lun Chan, Na Sai, Raluca Gearba, Loren G. Kaake, Kenrick J. Williams, Kevin Leung, Peter J. Rossky, and X.-Y. Zhu. Hot charge-transfer excitons set the time limit for charge separation at donor/acceptor interfaces in organic photovoltaics. *Nature Materials*, 12(1):66–73, 2013.

[29] I. Zhivkov, S. Neprek, and F. Schauer. Influence of oxygen on the parameters of a thin film copper phthalocyanine field effect transistor. *Advanced Materials for Optics and Electronics*, 9(5):175–180, 1999.

[30] Thomas D. Anthopoulos and Torfeh S. Shafai. Oxygen induced p-doping of α-nickel phthalocyanine vacuum sublimed films: Implication for its use in organic photovoltaics. *Applied Physics Letters*, 82(10):1628–1630, March 2003.

[31] Kihyon Hong, Kisoo Kim, and Jong-Lam Lee. Enhancement of electrical property by oxygen doping to copper phthalocyanine in inverted top emitting organic light emitting diodes. *Applied Physics Letters*, 95(21):213307–3, November 2009.

[32] G. Parthasarathy, C. Shen, A. Kahn, and S. R. Forrest. Lithium doping of semiconducting organic charge transport materials. *Journal of Applied Physics*, 89(9):4986–4992, May 2001.

[33] Jun Endo, Toshio Matsumoto, and Junji Kido. Organic electroluminescent devices with a vacuum-deposited lewis-acid-doped hole-injecting layer. *Japanese Journal of Applied Physics*, 41(Part 2, No. 3B):L358–L360, 2002.

[34] B. Lssem, M. Riede, and K. Leo. Doping of organic semiconductors. *physica status solidi (a)*, 210(1):943, 2013.

[35] Selina Olthof, Shafigh Mehraeen, Swagat K. Mohapatra, Stephen Barlow, Veaceslav Coropceanu, Jean-Luc Bredas, Seth R. Marder, and Antoine Kahn.

Ultralow doping in organic semiconductors: Evidence of trap filling. *Physical Review Letters*, 109(17):176601, October 2012.

[36] Richa Pandey and Russell J. Holmes. Graded donor-acceptor heterojunctions for efficient organic photovoltaic cells. *Advanced Materials*, 22(46):5301–5305, 2010.

[37] Fabio Silvestri, Michael D. Irwin, Luca Beverina, Antonio Facchetti, Giorgio A. Pagani, and Tobin J. Marks. Efficient squaraine-based solution processable bulk-heterojunction solar cells. *Journal of the American Chemical Society*, 130(52):17640–17641, December 2008.

[38] Guodan Wei, Siyi Wang, Kyle Renshaw, Mark E. Thompson, and Stephen R. Forrest. Solution-processed squaraine bulk heterojunction photovoltaic cells. *ACS Nano*, 4(4):1927–1934, April 2010.

[39] Aung Ko Ko Kyaw, Dong Hwan Wang, Vinay Gupta, Wei Lin Leong, Lin Ke, Guillermo C. Bazan, and Alan J. Heeger. Intensity dependence of currentvoltage characteristics and recombination in high-efficiency solution-processed small-molecule solar cells. *ACS Nano*, 7(5):4569–4577, May 2013.

[40] Alfred G. Emslie, Francis T. Bonner, and Leslie G. Peck. Flow of a viscous liquid on a rotating disk. *Journal of Applied Physics*, 29(5):858–862, May 1958.

[41] P.E. Burrows, S.R. Forrest, L.S. Sapochak, J. Schwartz, P. Fenter, T. Buma, V.S. Ban, and J.L. Forrest. Organic vapor phase deposition: a new method for the growth of organic thin films with large optical non-linearities. *Journal of Crystal Growth*, 156(12):91–98, November 1995.

[42] Cedric Rolin, Garen Vartanian, and Stephen R. Forrest. Laser induced fluorescence monitoring of the transport of small organic molecules in an organic vapor phase deposition system. *Journal of Applied Physics*, 112(11):113502–7, December 2012.

[43] Richard R. Lunt, Brian E. Lassiter, Jay B. Benziger, and Stephen R. Forrest. Organic vapor phase deposition for the growth of large area organic electronic devices. *Applied Physics Letters*, 95(23):233305–3, December 2009.

[44] Max Shtein, Peter Peumans, Jay B. Benziger, and Stephen R. Forrest. Micropatterning of small molecular weight organic semiconductor thin films using organic vapor phase deposition. *Journal of Applied Physics*, 93(7):4005–4016, April 2003.

[45] Gregory J. McGraw and Stephen R. Forrest. Vapor-phase microprinting of multicolor phosphorescent organic light emitting device arrays. *Advanced Materials*, 25(11):1583–1588, 2013.

[46] L. S. Hung, C. W. Tang, and M. G. Mason. Enhanced electron injection in organic electroluminescence devices using an al/LiF electrode. *Applied Physics Letters*, 70(2):152–154, January 1997.

[47] M. Stssel, J. Staudigel, F. Steuber, J. Simmerer, and A. Winnacker. Impact of the cathode metal work function on the performance of vacuum-deposited organic light emitting-devices. *Applied Physics A*, 68(4):387–390, April 1999.

[48] Junji Kido, Kenichi Hongawa, Masafumi Kohda, Katsutoshi Nagai, and Katsuro Okuyama. Molecularly doped polymers as a hole transport layer in organic electroluminescent devices. *Japanese Journal of Applied Physics*, 31(Part 2, No. 7B):L960–L962, 1992.

[49] G. Parthasarathy, P. E. Burrows, V. Khalfin, V. G. Kozlov, and S. R. Forrest. A metal-free cathode for organic semiconductor devices. *Applied Physics Letters*, 72(17):2138–2140, April 1998.

[50] Asuka Yamamori, Sachiko Hayashi, Toshiki Koyama, and Yoshio Taniguchi. Transparent organic light-emitting diodes using metal acethylacetonate complexes as an electron injective buffer layer. *Applied Physics Letters*, 78(21):3343–3345, May 2001.

[51] Y. Jin, A. Yadav, K. Sun, H. Sun, K. P. Pipe, and M. Shtein. Thermal boundary resistance of copper phthalocyanine-metal interface. *Applied Physics Letters*, 98(9):093305–3, March 2011.

[52] Brendan OConnor, Kwang H. An, Kevin P. Pipe, Yiying Zhao, and Max Shtein. Enhanced optical field intensity distribution in organic photovoltaic devices using external coatings. *Applied Physics Letters*, 89(23):233502–3, December 2006.

[53] M. Glatthaar, M. Niggemann, B. Zimmermann, P. Lewer, M. Riede, A. Hinsch, and J. Luther. Organic solar cells using inverted layer sequence. *Thin Solid Films*, 491(1-2):298–300, November 2005.

[54] Whitney Gaynor, Jung-Yong Lee, and Peter Peumans. Fully solution-processed inverted polymer solar cells with laminated nanowire electrodes. *ACS Nano*, 4(1):30–34, January 2010.

[55] Zhuangchun Wu, Zhihong Chen, Xu Du, Jonathan M. Logan, Jennifer Sippel, Maria Nikolou, Katalin Kamaras, John R. Reynolds, David B. Tanner, Arthur F. Hebard, and Andrew G. Rinzler. Transparent, conductive carbon nanotube films. *Science*, 305(5688):1273–1276, August 2004.

[56] Jun-Seok Yeo, Jin-Mun Yun, Dong-Yu Kim, Seok-Soon Kim, and Seok-In Na. Successive solvent-treated PEDOT:PSS electrodes for flexible ITO-free organic photovoltaics. *Solar Energy Materials and Solar Cells*, 114:104–109, July 2013.

[57] Dechan Angmo and Frederik C. Krebs. Flexible ITO-free polymer solar cells. *Journal of Applied Polymer Science*, 129(1):114, 2013.

[58] Cui Yuanri, Xu Xinghao, Jin Zhaoting, Peng Chuancai, and Xie Shuyun. Deposition of transparent conducting indium tin oxide thin films by reactive ion plating. *Thin Solid Films*, 115(3):195–201, May 1984.

[59] J. Kane, H.P. Schweizer, and W. Kern. Chemical vapor deposition of transparent electrically conducting layers of indium oxide doped with tin. *Thin Solid Films*, 29(1):155–163, September 1975.

[60] S. Naseem and T.J. Coutts. The influence of deposition parameters on the optical and electrical properties of r.f.-sputter- deposited indium tin oxide films. *Thin Solid Films*, 138(1):65–70, April 1986.

[61] Jiangeng Xue and Stephen R. Forrest. Carrier transport in multilayer organic photodetectors: II. effects of anode preparation. *Journal of Applied Physics*, 95(4):1869–1877, February 2004.

[62] M. W. Choi, K. Cho, C. Sung, J. Yang, Y. Yi, M. Noh, J. C. Choi, and K. Jeong. Enhanced hole injection in organic electroluminescent device with an additional oxygen-rich indiumtinoxide sublayer. *Journal of Vacuum Science & Technology B: Microelectronics and Nanometer Structures*, 22(2):758–761, 2004.

[63] Kiyoshi Sugiyama, Hisao Ishii, Yukio Ouchi, and Kazuhiko Seki. Dependence of indium-tin-oxide work function on surface cleaning method as studied by ultraviolet and x-ray photoemission spectroscopies. *Journal of Applied Physics*, 87(1):295–298, January 2000.

[64] A.E. Becquerel. Recherches sur les effets de la radiation chimique de la lumiere solaire au moyen des courants electriques. *Comptes Rendus de LAcademie des Sciences*, 9:145–149, 1839.

[65] Yanming Sun, Gregory C. Welch, Wei Lin Leong, Christopher J. Takacs, Guillermo C. Bazan, and Alan J. Heeger. Solution-processed small-molecule solar cells with 6.7% efficiency. *Nat Mater*, advance online publication, November 2011.

[66] Yutaka Matsuo, Ayako Ozu, Naoki Obata, Naoya Fukuda, Hideyuki Tanaka, and Eiichi Nakamura. Deterioration of bulk heterojunction organic photovoltaic devices by a minute amount of oxidized fullerene. *Chemical Communications*, 48(32):3878–3880, March 2012.

[67] Brett M. Savoie, Bijan Movaghar, Tobin J. Marks, and Mark A. Ratner. Simple analytic description of collection efficiency in organic photovoltaics. *The Journal of Physical Chemistry Letters*, 4(5):704–709, March 2013.

[68] E44 Committee. Test method for electrical performance of photovoltaic cells using reference cells under simulated sunlight. Technical report, ASTM International, 2009.

[69] G03 Committee. Tables for reference solar spectral irradiances: Direct normal and hemispherical on 37 tilted surface. Technical report, ASTM International, 2012.

[70] IEC: International Electrotechnical Commission. IEC 60904-3 photovoltaic devices part 3: Measurement principles for terrestrial photovoltaic (PV) solar devices with reference spectral irradiance data. Technical report, April 2008.

[71] IEC: International Electrotechnical Commission. IEC 60904-7 photovoltaic devices part 7: Computation of the spectral mismatch correction for measurements of photovoltaic devices. Technical report, November 2008.

[72] C.R. Osterwald. Translation of device performance measurements to reference conditions. *Solar Cells*, 18(34):269–279, September 1986.

[73] W. Shockley. The theory of p-n junctions in semiconductors and p-n junction transistors. *The Bell System technical journal*, 28(3):435–489, 1949.

[74] N. C. Giebink, G. P. Wiederrecht, M. R. Wasielewski, and S. R. Forrest. Ideal diode equation for organic heterojunctions. i. derivation and application. *Physical Review B*, 82(15):155305, October 2010.

[75] James C. Blakesley and Dieter Neher. Relationship between energetic disorder and open-circuit voltage in bulk heterojunction organic solar cells. *Physical Review B*, 84(7):075210, August 2011.

[76] C. W. Tang. Two-layer organic photovoltaic cell. *Applied Physics Letters*, 48(2):183–185, January 1986.

[77] Fan Yang, Max Shtein, and Stephen R. Forrest. Controlled growth of a molecular bulk heterojunction photovoltaic cell. *Nat Mater*, 4(1):37–41, January 2005.

[78] P. Sullivan, S. Heutz, S. M. Schultes, and T. S. Jones. Influence of codeposition on the performance of CuPc-c60 heterojunction photovoltaic devices. *Applied Physics Letters*, 84(7):1210–1212, February 2004.

[79] Soichi Uchida, Jiangeng Xue, Barry P. Rand, and Stephen R. Forrest. Organic small molecule solar cells with a homogeneously mixed copper phthalocyanine: C60 active layer. *Applied Physics Letters*, 84(21):4218–4220, May 2004.

[80] Hagen Klauk. Organic thin-film transistors. *Chemical Society Reviews*, 39(7):2643–2666, June 2010.

[81] N. Koch, J. Ghijsen, R. L. Johnson, J. Schwartz, J.-J. Pireaux, and A. Kahn. Physisorption-like interaction at the interfaces formed by pentacene and samarium. *The Journal of Physical Chemistry B*, 106(16):4192–4196, April 2002.

[82] P. G. Schroeder, C. B. France, J. B. Park, and B. A. Parkinson. Orbital alignment and morphology of pentacene deposited on au(111) and SnS2 studied using photoemission spectroscopy. *The Journal of Physical Chemistry B*, 107(10):2253–2261, March 2003.

[83] Joo H. Kang and X.-Y. Zhu. Pi-stacked pentacene thin films grown on au(111). *Applied Physics Letters*, 82(19):3248–3250, May 2003.

[84] Yoshinori Ishikawa, Yasuo Wada, and Toru Toyabe. Origin of characteristics differences between top and bottom contact organic thin film transistors. *Journal of Applied Physics*, 107(5):053709–7, March 2010.

[85] Christopher Siol, Christian Melzer, and Heinz von Seggern. Electron trapping in pentacene based p- and n-type organic field-effect transistors. *Applied Physics Letters*, 93(13):133303–3, September 2008.

[86] Qing Meng and Wenping Hu. Recent progress of n-type organic semiconducting small molecules for organic field-effect transistors. *Physical Chemistry Chemical Physics*, 14(41):14152–14164, October 2012.

[87] Y-Y Lin, D. J. Gundlach, S.F. Nelson, and T.N. Jackson. Stacked pentacene layer organic thin-film transistors with improved characteristics. *IEEE Electron Device Letters*, 18(12):606–608, 1997.

[88] M. D. McGehee and A. J. Heeger. Semiconducting (conjugated) polymers as materials for solid-state lasers. *Advanced Materials*, 12(22):1655–1668, 2000.

[89] I. D. W. Samuel and G. A. Turnbull. Organic semiconductor lasers. *Chemical Reviews*, 107(4):1272–1295, April 2007.

[90] D. G. Lidzey, D. D. C. Bradley, T. Virgili, A. Armitage, M. S. Skolnick, and S. Walker. Room temperature polariton emission from strongly coupled organic semiconductor microcavities. *Physical Review Letters*, 82(16):3316–3319, April 1999.

[91] Malte C. Gather, Anne Khnen, and Klaus Meerholz. White organic light-emitting diodes. *Advanced Materials*, 23(2):233–248, 2011.

[92] Neal R. Armstrong, Weining Wang, Dana M. Alloway, Diogenes Placencia, Erin Ratcliff, and Michael Brumbach. Organic/organic heterojunctions: Organic light emitting diodes and organic photovoltaic devices. *Macromolecular Rapid Communications*, 30(9-10):717–731, 2009.

[93] Samsung GALAXY s4 - life companion.

[94] OLED TV: Discover LG's OLED TV | LG USA.

[95] Lumiblade OLEDs - philips.

[96] Q. L. Song, M. L. Wang, E. G. Obbard, X. Y. Sun, X. M. Ding, X. Y. Hou, and C. M. Li. Degradation of small-molecule organic solar cells. *Applied Physics Letters*, 89(25):251118–3, December 2006.

[97] Ycel Sahin, Salima Alem, Rmi de Bettignies, and Jean-Michel Nunzi. Development of air stable polymer solar cells using an inverted gold on top anode structure. *Thin Solid Films*, 476(2):340–343, April 2005.

[98] C. Waldauf, M. Morana, P. Denk, P. Schilinsky, K. Coakley, S. A. Choulis, and C. J. Brabec. Highly efficient inverted organic photovoltaics using solution based titanium oxide as electron selective contact. *Applied Physics Letters*, 89(23):233517–3, December 2006.

[99] M. S. White, D. C. Olson, S. E. Shaheen, N. Kopidakis, and D. S. Ginley. Inverted bulk-heterojunction organic photovoltaic device using a solution-derived ZnO underlayer. *Applied Physics Letters*, 89(14):143517–3, October 2006.

[100] Rhonda F. Bailey-Salzman, Jiangeng Xue, Barry P. Rand, Alex Alexander, Mark E. Thompson, and Stephen R. Forrest. The effects of copper phthalocyanine purity on organic solar cell performance. *Organic Electronics*, 6(56):242–246, December 2005.

[101] Seungkeun Choi, William J. Potscavage, and Bernard Kippelen. Area-scaling of organic solar cells. *Journal of Applied Physics*, 106(5):054507–10, September 2009.

[102] Barry P. Rand, Diana P. Burk, and Stephen R. Forrest. Offset energies at organic semiconductor heterojunctions and their influence on the open-circuit voltage of thin-film solar cells. *Physical Review B*, 75(11):115327, March 2007.

[103] Jiangeng Xue, Soichi Uchida, Barry P. Rand, and Stephen R. Forrest. 4.2% efficient organic photovoltaic cells with low series resistances. *Applied Physics Letters*, 84(16):3013–3015, April 2004.

[104] P. Peumans, V. Bulovic, and S. R. Forrest. Efficient photon harvesting at high optical intensities in ultrathin organic double-heterostructure photovoltaic diodes. *Applied Physics Letters*, 76(19):2650–2652, May 2000.

[105] K. Yamamoto, S. Egusa, M. Sugiuchi, and A. Miura. Photogeneration mechanism of charged carriers in copper-phthalocyanine thin films. *Solid State Communications*, 85(1):5–10, January 1993.

[106] Ning Li, Brian E. Lassiter, Richard R. Lunt, Guodan Wei, and Stephen R. Forrest. Open circuit voltage enhancement due to reduced dark current in small molecule photovoltaic cells. *Applied Physics Letters*, 94(2):023307–3, January 2009.

[107] C. C. Wu, C. I. Wu, J. C. Sturm, and A. Kahn. Surface modification of indium tin oxide by plasma treatment: An effective method to improve the efficiency, brightness, and reliability of organic light emitting devices. *Applied Physics Letters*, 70(11):1348–1350, March 1997.

[108] V. Shrotriya, G. Li, Y. Yao, T. Moriarty, K. Emery, and Y. Yang. Accurate measurement and characterization of organic solar cells. *Advanced Functional Materials*, 16(15):2016–2023, 2006.

[109] V. D. Mihailetchi, P. W. M. Blom, J. C. Hummelen, and M. T. Rispens. Cathode dependence of the open-circuit voltage of polymer:fullerene bulk heterojunction solar cells. *Journal of Applied Physics*, 94(10):6849–6854, November 2003.

[110] Yoshiki Kinoshita, Rie Takenaka, and Hideyuki Murata. Independent control of open-circuit voltage of organic solar cells by changing film thickness of MoO3 buffer layer. *Applied Physics Letters*, 92(24):243309–243309–3, June 2008.

[111] M. A. Baldo and S. R. Forrest. Interface-limited injection in amorphous organic semiconductors. *Physical Review B*, 64(8):085201, August 2001.

[112] Aung Ko Ko Kyaw, Dong Hwan Wang, David Wynands, Jie Zhang, Thuc-Quyen Nguyen, Guillermo C. Bazan, and Alan J. Heeger. Improved light harvesting and improved efficiency by insertion of an optical spacer (ZnO) in solution-processed small-molecule solar cells. *Nano Letters*, June 2013.

[113] Zhicai He, Chengmei Zhong, Shijian Su, Miao Xu, Hongbin Wu, and Yong Cao. Enhanced power-conversion efficiency in polymer solar cells using an inverted device structure. *Nature Photonics*, 6(9):591–595, 2012.

[114] Martin A. Green, Keith Emery, Yoshihiro Hishikawa, Wilhelm Warta, and Ewan D. Dunlop. Solar cell efficiency tables (version 41). *Progress in Photovoltaics: Research and Applications*, 21(1):111, 2013.

[115] Jingbi You, Letian Dou, Ken Yoshimura, Takehito Kato, Kenichiro Ohya, Tom Moriarty, Keith Emery, Chun-Chao Chen, Jing Gao, Gang Li, and Yang Yang. A polymer tandem solar cell with 10.6% power conversion efficiency. *Nature Communications*, 4:1446, February 2013.

[116] Mikkel Jrgensen, Kion Norrman, and Frederik C. Krebs. Stability/degradation of polymer solar cells. *Solar Energy Materials and Solar Cells*, 92(7):686–714, July 2008.

[117] Frederik C. Krebs. *Stability and Degradation of Organic and Polymer Solar Cells*. John Wiley & Sons, April 2012.

[118] Mikkel Jrgensen, Kion Norrman, Suren A. Gevorgyan, Thomas Tromholt, Birgitta Andreasen, and Frederik C. Krebs. Stability of polymer solar cells. *Advanced Materials*, 24(5):580612, 2012.

[119] Frederik C. Krebs, Jon E. Carl, Nicolaj Cruys-Bagger, Morten Andersen, Mathilde R. Lilliedal, Mark A. Hammond, and Sren Hvidt. Lifetimes of organic photovoltaics: photochemistry, atmosphere effects and barrier layers in ITO-MEHPPV:PCBM-aluminium devices. *Solar Energy Materials and Solar Cells*, 86(4):499–516, April 2005.

[120] Craig H. Peters, I. T. Sachs-Quintana, William R. Mateker, Thomas Heumueller, Jonathan Rivnay, Rodigo Noriega, Zach M. Beiley, Eric T. Hoke, Alberto Salleo, and Michael D. McGehee. The mechanism of burn-in loss in a high efficiency polymer solar cell. *Advanced Materials*, 24(5):663–668, 2012.

[121] Xiaoran Tong, Nana Wang, Michael Slootsky, Junsheng Yu, and R. Stephen Forrest. Intrinsic burn-in efficiency loss of small-molecule organic photovoltaic cells due to exciton-induced trap formation. *Solar Energy Materials and Solar Cells*, Accepted, 2013.

[122] Eszter Voroshazi, Bregt Verreet, Tom Aernouts, and Paul Heremans. Long-term operational lifetime and degradation analysis of p3ht:PCBM photovoltaic cells. *Solar Energy Materials and Solar Cells*, 95(5):1303–1307, May 2011.

[123] Panagiotis E. Keivanidis, Frdric Laquai, Ian A. Howard, and Richard H. Friend. Room-temperature phase demixing in bulk heterojunction layers of solution-processed organic photodetectors: the effect of active layer ageing on the device electro-optical properties. *Advanced Functional Materials*, 21(8):1355–1363, 2011.

[124] R. Lessmann, Z. Hong, S. Scholz, B. Maennig, M.K. Riede, and K. Leo. Aging of flat heterojunction zinc phthalocyanine/fullerene c60 organic solar cells. *Organic Electronics*, 11(4):539–543, April 2010.

[125] D. L. King, M. A. Quintana, J. A. Kratochvil, D. E. Ellibee, and B. R. Hansen. Photovoltaic module performance and durability following long-term field exposure. *Progress in Photovoltaics: Research and Applications*, 8(2):241–256, 2000.

[126] K. Morita, T. Inoue, H. Kato, I. Tsuda, and Y. Kishikawa. Degradation factor analysis of crystalline-si PV modules through long-term field exposure test. In *Proceedings of 3rd World conference on photovoltaic energy conversion, vols A-C*, volume A-C, pages 1948–1951, Osaka, JAPAN, May 2003.

[127] D. L. Staebler and C. R. Wronski. Reversible conductivity changes in discharge-produced amorphous si. *Applied Physics Letters*, 31(4):292–294, August 1977.

[128] Matthew O. Reese, Suren A. Gevorgyan, Mikkel Jrgensen, Eva Bundgaard, Sarah R. Kurtz, David S. Ginley, Dana C. Olson, Matthew T. Lloyd, Pasquale

Morvillo, Eugene A. Katz, Andreas Elschner, Olivier Haillant, Travis R. Currier, Vishal Shrotriya, Martin Hermenau, Moritz Riede, Kiril R. Kirov, Gregor Trimmel, Thomas Rath, Olle Ingans, Fengling Zhang, Mattias Andersson, Kristofer Tvingstedt, Monica Lira-Cantu, Darin Laird, Christine McGuiness, Srinivas (Jimmy) Gowrisanker, Michael Pannone, Min Xiao, Jens Hauch, Roland Steim, Dean M. DeLongchamp, Roland Rsch, Harald Hoppe, Nieves Espinosa, Antonio Urbina, Glsah Yaman-Uzunoglu, Jrg-Bernd Bonekamp, Albert J.J.M. van Breemen, Claudio Girotto, Eszter Voroshazi, and Frederik C. Krebs. Consensus stability testing protocols for organic photovoltaic materials and devices. *Solar Energy Materials and Solar Cells*, 95(5):1253–1267, May 2011.

[129] Suren A. Gevorgyan, Mikkel Jrgensen, and Frederik C. Krebs. A setup for studying stability and degradation of polymer solar cells. *Solar Energy Materials and Solar Cells*, 92(7):736–745, July 2008.

[130] Suren A. Gevorgyan, Mikkel Jrgensen, Frederik C. Krebs, and Kristian O. Sylvester-Hvid. A compact multi-chamber setup for degradation and lifetime studies of organic solar cells. *Solar Energy Materials and Solar Cells*, 95(5):1389–1397, May 2011.

[131] M.O. Reese, A.K. Sigdel, J.J. Berry, D.S. Ginley, and S.E. Shaheen. A simple miniature controlled-atmosphere chamber for optoelectronic characterizations. *Solar Energy Materials and Solar Cells*, 94(7):1254–1258, July 2010.

[132] Frederik C. Krebs and Kion Norrman. Analysis of the failure mechanism for a stable organic photovoltaic during 10 000 h of testing. *Progress in Photovoltaics: Research and Applications*, 15(8):697–712, 2007.

[133] S. Schuller, P. Schilinsky, J. Hauch, and C. J. Brabec. Determination of the degradation constant of bulk heterojunction solar cells by accelerated lifetime measurements. *Applied Physics A*, 79(1):37–40, June 2004.

[134] Rmi De Bettignies, Jocelyne Leroy, Muriel Firon, and Carole Sentein. Accelerated lifetime measurements of p3ht:PCBM solar cells. *Synthetic Metals*, 156(78):510–513, April 2006.

[135] Bert Conings, Sabine Bertho, Koen Vandewal, Alessia Senes, Jan DHaen, Jean Manca, and Ren A. J. Janssen. Modeling the temperature induced degradation kinetics of the short circuit current in organic bulk heterojunction solar cells. *Applied Physics Letters*, 96(16):163301–3, April 2010.

[136] Eszter Voroshazi, Bregt Verreet, Andrea Buri, Robert Mller, Daniele Di Nuzzo, and Paul Heremans. Influence of cathode oxidation via the hole extraction layer in polymer:fullerene solar cells. *Organic Electronics*, 12(5):736–744, May 2011.

[137] M. Hermenau, Sebastian Scholz, Karl Leo, and Moritz Riede. Total charge amount as indicator for the degradation of small molecule organic solar cells. *Solar Energy Materials and Solar Cells*, 95(5):1278–1283, May 2011.

[138] Stefan Schfer, Andreas Petersen, Thomas A. Wagner, Rolf Kniprath, Dominic Lingenfelser, Achmad Zen, Thomas Kirchartz, Birger Zimmermann, Uli Wrfel, Xianjin Feng, and Thomas Mayer. Influence of the indium tin oxide/organic interface on open-circuit voltage, recombination, and cell degradation in organic small-molecule solar cells. *Physical Review B*, 83(16):165311, April 2011.

[139] P.E Burrows, G.L Graff, M.E Gross, P.M Martin, M.K Shi, M Hall, E Mast, C Bonham, W Bennett, and M.B Sullivan. Ultra barrier flexible substrates for flat panel displays. *Displays*, 22(2):65–69, May 2001.

[140] S. Cros, R. de Bettignies, S. Berson, S. Bailly, P. Maisse, N. Lemaitre, and S. Guillerez. Definition of encapsulation barrier requirements: A method applied to organic solar cells. *Solar Energy Materials and Solar Cells*, 95, Supplement 1:S65–S69, May 2011.

[141] S. Schubert, H. Klumbies, L. Mller-Meskamp, and K. Leo. Electrical calcium test for moisture barrier evaluation for organic devices. *Review of Scientific Instruments*, 82(9):094101–8, September 2011.

[142] Chih-Yu Chang, Chun-Ting Chou, Yun-Jun Lee, Miin-Jang Chen, and Feng-Yu Tsai. Thin-film encapsulation of polymer-based bulk-heterojunction photovoltaic cells by atomic layer deposition. *Organic Electronics*, 10(7):1300–1306, November 2009.

[143] N.Serdar Sariciftci. Role of buckminsterfullerene, c60, in organic photoelectric devices. *Progress in Quantum Electronics*, 19(2):131–159, 1995.

[144] Roger Taylor, Jonathan P. Parsons, Anthony G. Avent, Steven P. Rannard, T. John Dennis, Jonathan P. Hare, Harold W. Kroto, and David R. M. Walton. Degradation of c60 by light. *, Published online: 23 May 1991; | doi:10.1038/351277a0*, 351(6324):277–277, May 1991.

[145] Toshinori Matsushima, Masayuki Yahiro, and Chihaya Adachi. Estimation of electron traps in carbon-60 field-effect transistors by a thermally stimulated current technique. *Applied Physics Letters*, 91(10):103505–3, September 2007.

[146] Martin Hermenau, Moritz Riede, Karl Leo, Suren A. Gevorgyan, Frederik C. Krebs, and Kion Norrman. Water and oxygen induced degradation of small molecule organic solar cells. *Solar Energy Materials and Solar Cells*, 95(5):1268–1277, May 2011.

[147] Andrea Seemann, Tobias Sauermann, Christoph Lungenschmied, Oskar Armbruster, Siegfried Bauer, H.-J. Egelhaaf, and Jens Hauch. Reversible and irreversible degradation of organic solar cell performance by oxygen. *Solar Energy*, 85(6):1238–1249, June 2011.

[148] Kion Norrman, Suren A. Gevorgyan, and Frederik C. Krebs. Water-induced degradation of polymer solar cells studied by h218o labeling. *ACS Applied Materials & Interfaces*, 1(1):102–112, January 2009.

[149] Toshihiro Yamanari, Tetsuya Taima, Jun Sakai, Jun Tsukamoto, and Yuji Yoshida. Effect of buffer layers on stability of polymer-based organic solar cells. *Japanese Journal of Applied Physics*, 49(1):01AC02, 2010.

[150] B. Zimmermann, U. Wrfel, and M. Niggemann. Longterm stability of efficient inverted p3ht:PCBM solar cells. *Solar Energy Materials and Solar Cells*, 93(4):491–496, April 2009.

[151] Kion Norrman, Morten V. Madsen, Suren A. Gevorgyan, and Frederik C. Krebs. Degradation patterns in water and oxygen of an inverted polymer solar cell. *Journal of the American Chemical Society*, 132(47):16883–16892, December 2010.

[152] Eric T. Hoke, I. T. Sachs-Quintana, Matthew T. Lloyd, Isaac Kauvar, William R. Mateker, Alexandre M. Nardes, Craig H. Peters, Nikos Kopidakis, and Michael D. McGehee. The role of electron affinity in determining whether fullerenes catalyze or inhibit photooxidation of polymers for solar cells. *Advanced Energy Materials*, 2(11):13511357, 2012.

[153] Richard R. Lunt, Timothy P. Osedach, Patrick R. Brown, Jill A. Rowehl, and Vladimir Bulovi. Practical roadmap and limits to nanostructured photovoltaics. *Advanced Materials*, 23(48):5712–5727, 2011.

[154] Reg Bauld, Leesa M. Fleury, Marima Van Walsh, and Giovanni Fanchini. Correlation between density of paramagnetic centers and photovoltaic degradation in polythiophene-fullerene bulk heterojunction solar cells. *APL: Organic Electronics and Photonics*, 5(9):204–204, September 2012.

[155] Matthew O. Reese, Alexandre M. Nardes, Benjamin L. Rupert, Ross E. Larsen, Dana C. Olson, Matthew T. Lloyd, Sean E. Shaheen, David S. Ginley, Garry Rumbles, and Nikos Kopidakis. Photoinduced degradation of polymer and polymerfullerene active layers: Experiment and theory. *Advanced Functional Materials*, 20(20):3476–3483, 2010.

[156] Obadiah G. Reid, Glennis E. Rayermann, David C. Coffey, and David S. Ginger. Imaging local trap formation in conjugated polymer solar cells: A comparison of time-resolved electrostatic force microscopy and scanning kelvin probe imaging. *The Journal of Physical Chemistry C*, 114(48):20672–20677, December 2010.

[157] R. A. Street and D. M. Davies. Kinetics of light induced defect creation in organic solar cells. *APL: Organic Electronics and Photonics*, 6(1):16–16, January 2013.

[158] Assaf Manor, Eugene A. Katz, Thomas Tromholt, and Frederik C. Krebs. Electrical and photo-induced degradation of ZnO layers in organic photovoltaics. *Advanced Energy Materials*, 1(5):836–843, 2011.

[159] Kenji Kawano, Roberto Pacios, Dmitry Poplavskyy, Jenny Nelson, Donal D.C. Bradley, and James R. Durrant. Degradation of organic solar cells due to air exposure. *Solar Energy Materials and Solar Cells*, 90(20):3520–3530, December 2006.

[160] Matthew O. Reese, Anthony J. Morfa, Matthew S. White, Nikos Kopidakis, Sean E. Shaheen, Garry Rumbles, and David S. Ginley. Pathways for the degradation of organic photovoltaic p3ht:PCBM based devices. *Solar Energy Materials and Solar Cells*, 92(7):746–752, July 2008.

[161] Yong Hyun Kim, Christoph Sachse, Martin Hermenau, Karsten Fehse, Moritz Riede, Lars Mller-Meskamp, and Karl Leo. Improved efficiency and lifetime in small molecule organic solar cells with optimized conductive polymer electrodes. *Applied Physics Letters*, 99(11):113305–3, September 2011.

[162] Barry P. Rand, Jiangeng Xue, Soichi Uchida, and Stephen R. Forrest. Mixed donor-acceptor molecular heterojunctions for photovoltaic applications. i. material properties. *Journal of Applied Physics*, 98(12):124902–7, December 2005.

[163] N. C. Giebink, B. W. DAndrade, M. S. Weaver, P. B. Mackenzie, J. J. Brown, M. E. Thompson, and S. R. Forrest. Intrinsic luminance loss in phosphorescent small-molecule organic light emitting devices due to bimolecular annihilation reactions. *Journal of Applied Physics*, 103(4):044509–9, February 2008.

[164] Klaus Kuhnke, Ren Becker, Maximilian Epple, and Klaus Kern. C_{60} exciton quenching near metal surfaces. *Physical Review Letters*, 79(17):3246–3249, October 1997.

[165] Paul A. Heiney, John E. Fischer, Andrew R. McGhie, William J. Romanow, Arnold M. Denenstein, John P. McCauley Jr., Amos B. Smith, and David E. Cox. Orientational ordering transition in solid c_{60}. *Physical Review Letters*, 66(22):2911–2914, June 1991.

[166] S. Berner, M. de Wild, L. Ramoino, S. Ivan, A. Baratoff, H.-J. Gntherodt, H. Suzuki, D. Schlettwein, and T. A. Jung. Adsorption and two-dimensional phases of a large polar molecule:sub-phthalocyanine on ag(111). *Physical Review B*, 68(11):115410, September 2003.

[167] Nana Wang, Jeramy D. Zimmerman, Xiaoran Tong, Xin Xiao, Junsheng Yu, and Stephen R. Forrest. Snow cleaning of substrates increases yield of large-area organic photovoltaics. *Applied Physics Letters*, 101(13):133901–4, September 2012.

[168] P.C. Eklund, A.M. Rao, Ping Zhou, Ying Wang, and J.M. Holden. Photochemical transformation of c60 and c70 films. *Thin Solid Films*, 257(2):185–203, March 1995.

[169] M. Karas, D. Bachmann, U. Bahr, and F. Hillenkamp. Matrix-assisted ultraviolet laser desorption of non-volatile compounds. *International Journal of Mass Spectrometry and Ion Processes*, 78:53–68, September 1987.

[170] Brian E. Lassiter, Jeramy D. Zimmerman, Anurag Panda, Xin Xiao, and Stephen R. Forrest. Tandem organic photovoltaics using both solution and vacuum deposited small molecules. *Applied Physics Letters*, 101(6):063303–4, August 2012.

[171] Nana Wang, Xiaoran Tong, Quinn Burlingame, Junsheng Yu, and Stephen R. Forrest. Photodegradation of small-molecule organic photovoltaics. *Solar Energy Materials and Solar Cells*, 125:170–175, June 2014.

[172] Mamoru Fujitsuka, Koichi Fujiwara, Yasujiro Murata, Shinobu Uemura, Masashi Kunitake, Osamu Ito, and Koichi Komatsu. Properties of photoexcited states of c₁₈₀, a triangle trimer of c₆₀. *Chemistry Letters*, 30(5):384–385, 2001.

[173] Mamoru Fujitsuka, Chuping Luo, Osamu Ito, Yasujiro Murata, and Koichi Komatsu. Triplet properties and photoinduced electron-transfer reactions of c120, the [2+2] dimer of fullerene c60. *The Journal of Physical Chemistry A*, 103(36):7155–7160, September 1999.

[174] Chi-Ta Chou, Wei-Li Tang, Yian Tai, Chien-Hung Lin, Chin-Hsin J. Liu, Li-Chyong Chen, and Kuei-Hsien Chen. Effect of substrate temperature on orientation of subphthalocyanine molecule in organic photovoltaic cells. *Thin Solid Films*, 520(1):2289–2292, January 2012.

[175] Jeramy D. Zimmerman, Brian E. Lassiter, Xin Xiao, Kai Sun, Andrei Dolocan, Raluca Gearba, David A. Vanden Bout, Keith J. Stevenson, Piyumie Wickramasinghe, Mark E. Thompson, and Stephen R. Forrest. Control of interface order by inverse quasi-epitaxial growth of squaraine/fullerene thin film photovoltaics. *ACS Nano*, 7(10):9268–9275, October 2013.

[176] Andrew N. Bartynski, Cong Trinh, Anurag Panda, Kevin Bergemann, Brian E. Lassiter, Jeramy D. Zimmerman, Stephen R. Forrest, and Mark E. Thompson. A fullerene-based organic exciton blocking layer with high electron conductivity. *Nano Letters*, 13(7):3315–3320, July 2013.

[177] Santanu Karan and Biswanath Mallik. Effects of annealing on the morphology and optical property of copper(II) phthalocyanine nanostructured thin films. *Solid State Communications*, 143(67):289–294, August 2007.

[178] C. Taliani, G. Ruani, R. Zamboni, R. Danieli, S. Rossini, V. N. Denisov, V. M. Burlakov, F. Negri, G. Orlandi, and F. Zerbetto. Light-induced oxygen incision of c60. *Journal of the Chemical Society, Chemical Communications*, (3):220–222, January 1993.

[179] Rebecca R. Hung and Joseph J. Grabowski. A precise determination of the triplet energy of carbon (c60) by photoacoustic calorimetry. *The Journal of Physical Chemistry*, 95(16):6073–6075, August 1991.

[180] Xin Xiao, Jeramy D. Zimmerman, Brian E. Lassiter, Kevin J. Bergemann, and Stephen R. Forrest. A hybrid planar-mixed tetraphenyldibenzoperiflanthene/c70 photovoltaic cell. *Applied Physics Letters*, 102(7):073302–073302–4, February 2013.

[181] R. Franke, B. Maennig, A. Petrich, and M. Pfeiffer. Long-term stability of tandem solar cells containing small organic molecules. *Solar Energy Materials and Solar Cells*, 92(7):732–735, July 2008.

[182] Christian Uhrich, G. Schwartz, Bert Maennig, Wolf-Michael Gnehr, Stefan Sontag, Oliver Erfurth, Eginhard Wollrab, Karsten Walzer, Jan Foerster, Andre Weiss, Olga Tsaryova, Karl Leo, Moritz K. Riede, and Martin Pfeiffer. Efficient and long-term stable organic vacuum deposited tandem solar cells. *Proc. SPIE 7722, Organic Photonics IV, 77220G*, May 2010.

[183] M. P. de Jong, L. J. van IJzendoorn, and M. J. A. de Voigt. Stability of the interface between indium-tin-oxide and poly(3,4-ethylenedioxythiophene)/poly(styrenesulfonate) in polymer light-emitting diodes. *Applied Physics Letters*, 77(14):2255–2257, October 2000.

[184] Brian W. DAndrade, Stephen R. Forrest, and Anna B. Chwang. Operational stability of electrophosphorescent devices containing p and n doped transport layers. *Applied Physics Letters*, 83(19):3858–3860, November 2003.

[185] Xin Xu, Marcelo Davanco, Xiangfei Qi, and Stephen R. Forrest. Direct transfer patterning on three dimensionally deformed surfaces at micrometer resolutions and its application to hemispherical focal plane detector arrays. *Organic Electronics*, 9(6):1122–1127, December 2008.

[186] Xin Xu, Momchil Mihnev, Andre Taylor, and Stephen R. Forrest. Organic photodetector arrays with indium tin oxide electrodes patterned using directly transferred metal masks. *Applied Physics Letters*, 94(4):043313, 2009.

[187] C. Kyle Renshaw, Xin Xu, and Stephen R. Forrest. A monolithically integrated organic photodetector and thin film transistor. *Organic Electronics*, 11(1):175–178, January 2010.

[188] Keum-Dong Jung, Yoo Chul Kim, Hyungcheol Shin, Byung-Gook Park, Jong Duk Lee, Eou Sik Cho, and Sang Jik Kwon. A study on the carrier injection mechanism of the bottom-contact pentacene thin film transistor. *Applied Physics Letters*, 96(10):103305, 2010.

[189] Dipti Gupta, M. Katiyar, and Deepak Gupta. An analysis of the difference in behavior of top and bottom contact organic thin film transistors using device simulation. *Organic Electronics*, 10(5):775–784, August 2009.

[190] Masakazu Nakamura, Hirokazu Ohguri, Naoyuki Goto, Hiroshi Tomii, Mingsheng Xu, Takashi Miyamoto, Ryousuke Matsubara, Noboru Ohashi, Masaaki Sakai, and Kazuhiro Kudo. Extrinsic limiting factors of carrier transport in organic field-effect transistors. *Applied Physics A*, 95(1):73–80, December 2008.

[191] I. Nausieda, Ryu Kyungbum, I. Kymissis, A.I. Akinwande, V. Bulovic, and C.G. Sodini. An organic active-matrix imager. *Electron Devices, IEEE Transactions on*, 55(2):527–532, 2008.

[192] T. Someya, Y. Kato, Shingo Iba, Y. Noguchi, T. Sekitani, H. Kawaguchi, and T. Sakurai. Integration of organic FETs with organic photodiodes for a large area, flexible, and lightweight sheet image scanners. *Electron Devices, IEEE Transactions on*, 52(11):2502–2511, 2005.

[193] Tsuyoshi Sekitani, Ute Zschieschang, Hagen Klauk, and Takao Someya. Flexible organic transistors and circuits with extreme bending stability. *Nature Materials*, 9(12):1015–1022, December 2010.

[194] Michael S. Arnold, Jeramy D. Zimmerman, Christopher K. Renshaw, Xin Xu, Richard R. Lunt, Christine M. Austin, and Stephen R. Forrest. Broad spectral response using carbon nanotube/organic semiconductor/c60 photodetectors. *Nano Letters*, 9(9):3354–3358, 2009.

[195] Tsuyoshi Sekitani, Shingo Iba, Yusaku Kato, Yoshiaki Noguchi, Takayasu Sakurai, and Takao Someya. Submillimeter radius bendable organic field-effect transistors. *Journal of Non-Crystalline Solids*, 352(9-20):1769–1773, June 2006.

[196] D. K. Hwang, Kimoon Lee, Jae Hoon Kim, Seongil Im, Chang Su Kim, Hong Koo Baik, Ji Hoon Park, and Eugene Kim. Low-voltage high-mobility pentacene thin-film transistors with polymer/high-k oxide double gate dielectrics. *Applied Physics Letters*, 88(24):243513, 2006.

[197] J. Douglas Faires and Richard L. Burden. *Numerical Methods*. Cengage Learning, April 2012.

[198] MATLAB. MATLAB bvp4c document, 2013.

[199] L. F. Shampine, I. Gladwell, and S. Thompson. *Solving ODEs with MATLAB*. Cambridge University Press, April 2003.

[200] Won Y. Yang, Wenwu Cao, Tae-Sang Chung, and John Morris. *Applied Numerical Methods Using MATLAB*. John Wiley & Sons, June 2005.

[201] Robert E. White. *Computational Mathematics: Models, Methods, and Analysis with MATLAB and MPI*. CRC Press, September 2003.

[202] Mark S. Gockenbach. *Understanding and Implementing the Finite Element Method*. SIAM, 2006.